UNIVERSITÀ DEGLI STUDI DI PADOVA

Department of Geosciences

MASTER DEGREE

'Geophysics for Natural Risks and Resources'

Thesis

COMBINING PASSIVE SEISMIC METHODS FOR THE DYNAMIC CHARACTERIZATION OF TALL BUILDINGS

Letizia Nardi

Supervised by:

Dr.ssa Ilaria Barone

Dr.ssa Gwenola Michaud (external)

Dr. Alessandro Brovelli (external)

A.Y. 2023/2024

27th September 2024

ABSTRACT

The identification of the dynamic properties of a structure is an excellent tool to predict its behaviour under different seismic excitations and to assess its state of health.

By recording seismic noise, two different structures were analysed: a medieval bell tower in Angera (VA), on the eastern shore of Lago Maggiore, and the chimney of a former industrial site in Porto Tolle (RO).

The two buildings differ in numerous structural aspects, such as the height, the shape and the construction technique, in the different environmental context in which they are located, which influences the characteristics of seismic noise, and in the different design of the seismic monitoring system.

The data collected from several triaxial velocimeters and accelerometers were processed using different analysis methods, such as spectral analysis, frequency power density analysis -PSD, SVD-, spectral H/V ratio, motion analysis -hodograms- and modal analysis.

The results led to the identification of the main oscillation frequencies, modes, directions and amplitude of the two structures. The comparison of analysis methods showed that the combination of modal analysis, PSD, and HVSR provided the most reliable results, offering a comprehensive understanding of the dynamic behavior of the two structures. While the combination of spectrograms with PSDs allow for the characterization of the input signal in terms of energy and frequency content and the addition of RMS analysis enables the quantification of signal intensity, thus identifying the istances when the structure is most excited.

Table of contents

1. INTRODUCTION

1.1 SEISMIC WAVES

According to data provided by the INGV - National Institute of Geophysics and Volcanology -, over the 365 days preceding 28 August 2024, there have been 2,718 seismic events of magnitude greater than 2 globally. This is equivalent to approximately eight seismic events per day worldwide. This highlights the continuous geological activity and evolution of our planet, as well as the significant impact of seismology, which studies seismic phenomena, on our daily lives.

The release of energy by seismic events, even those of low magnitude, is considerable. The advent of increasingly sophisticated measuring instruments has enabled the measure of these phenomena worldwide. The high energy of naturally released elastic waves during an earthquake allows for the study of the deep structure of the Earth. On the other hand, the propagation of seismic waves released either artificially or naturally from lower energy sources provides insights into the smaller-scale and more shallow structure of the Earth.

Seismic waves are elastic waves that propagate in the interior or on the surface of the Earth with varying directions and speeds. Given these diverse characteristics of the waves, they have been classified under different names. The initial significant classification is between body and surface waves. Body waves are transmitted through an elastic medium, whereas surface waves propagate at the interface between distinct media. Subsequently, body waves are classified into P-waves and S-waves. Similarly, surface waves divide into Rayleigh waves and Love waves.

As illustrated in *Fig.1*, P-waves or primary waves, which derive their name from being the first waves to manifest in the seismogram, are longitudinal waves, i.e.they propagate with a particle motion in compression and expansion along

the direction of propagation. In contrast, S-waves, which are secondary waves, are transverse waves, i.e. they propagate with a shearing particle motion in the plane perpendicular to the direction of propagation. As for surface waves, Rayleigh waves have an elliptical polarisation within the plane defined by the normal to the surface and the direction of propagation (Rayleigh 1892). They propagate in the vicinity of the surface of a homogeneous half-space, with a particle motion of a retrograde vertical ellipse, anticlockwise for a wave travelling to the right (Novotny, 1999). Finally, Love waves propagate in media with a low-velocity layer overlying a homogeneous half-space. The particle motion of Love waves is transverse and parallel to the surface.

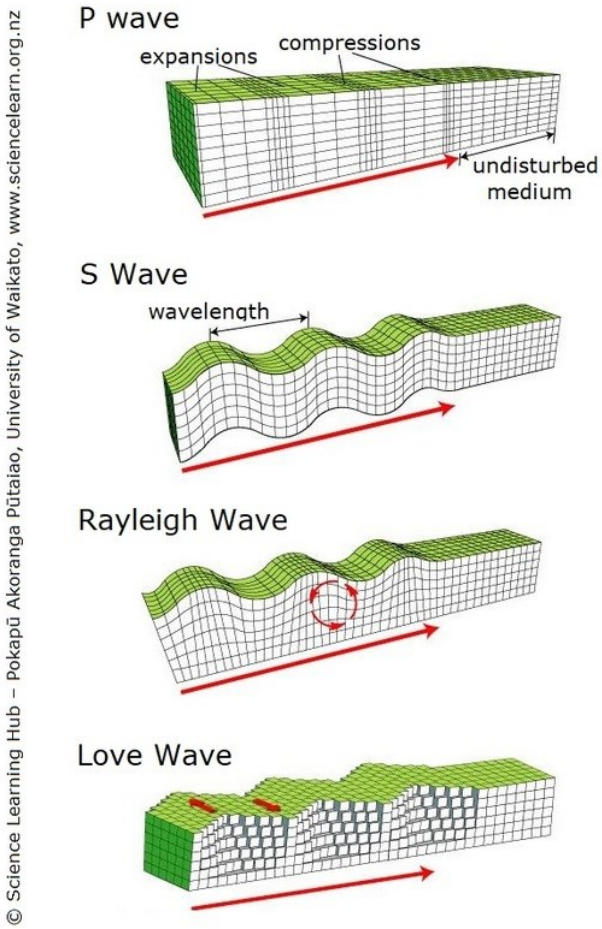

Figure 1: Illustration of the different type of waves and their propagation modes [The University of Waikato, 2007]

As previously stated, the study of seismic waves offers insights into a range of crustal and deep Earth geological structures, including both larger macro-structures and smaller surface features. This method is built upon the premise that seismic waves pass through different types of rocks and geological formations at varying speeds, with their velocity being influenced by the physical properties of the medium through which they propagate.

Two types of seismic data acquisition exist. The first involves the generation of seismic waves with artificial means such as impact hammer, accelerated mass and vibroseis, which are then recorded by a network of strategically placed sensors. In this case we talk about active seismic acquisitions. The second option involves the passive detection of seismic waves, also called "ambient seismic noise". Seismic noise is defined as the ambient vibration of the earth's surface, generated by the combination of low frequency natural microseisms (≤1 Hz) and higher frequency anthropogenic microtremors (≥1Hz; *Bonnefoy-Claudet et al. 2006; Landès et al. 2010)*. This background noise is a mixture of various seismic wave phases, which contains information on the sources and transmission paths of the waves, and subsurface structure *(Okada and Suto 2003)*. Most anthropogenic seismic noise sources and some natural sources – i.e. wind and ocean waves - are located close to the surface of the earth, which leads to energy mostly released as surface waves *(Molnar et al. 2022)*.

As mentioned earlier, surface waves are generated at the interface between two media and in the case of elastic waves at the interface between soil and air. However, they should not be regarded as a fundamentally new type of wave, but rather as an interference phenomenon of body waves *(Novotny 1999)*. In comparison to body waves, they exhibit a higher amplitude and are responsible for the majority of damage following an earthquake. Surface waves are relatively straightforward to generate, which is advantageous when designing an active surface wave study. However, this can be a disadvantage

when the study is not focused on them, as their high amplitude can mask other types of signals.

It is also noteworthy that surface waves display a dispersive behaviour when crossing a non-homogeneous medium, which means that their velocity is dependent on frequency. This property of surface waves, in addition with the observation that the Rayleigh wave velocity is similar to the shear wave velocity - $V_R \approx 0{,}9V_S$ -, offers significant insights into the estimation of a soil model and the determination of the seismic soil type.

The acquisition of surface wave data and the estimation of a soil model are of great significance in the prevention of seismic damage and the comprehension of the effects of an earthquake in a particular area, which can be defined as seismic local response. In fact, local geological conditions have the capacity to modify the seismic ground motion, leading to amplification. Such conditions may be determined by the topography of the area in question, as well as the specific type of soil in which the structures are constructed.

The influence of soil deposits on a given area can also be observed in the dynamic behaviour of structures. This is due to the fact that soil response influences structural response, and vice versa. This is known as the SSI - soil structure interaction -. In the worst case, if the period of the ground motion corresponds to the period of oscillation of the structure, the oscillation is amplified. This phenomenon is known as resonance, which results in enhanced damage and an elevated probability of collapse of the structure.

Thus, it is crucial to determine both the soil response and the structural dynamics. In the two case studies presented in this thesis, the objective is to obtain information on the dynamic behavior of the structures under examination through the analysis of ambient noise, and on the relationship between the structure behaviour and the environmental forcings.

1.2 DYNAMIC IDENTIFICATION OF STRUCTURES

Structures are subjected to dynamic loads and different stresses over time. Additionally, they can be subjected to various transient external excitations, which can be either natural, such as earthquakes or wind, or artificial.

Structural dynamics aims to define the internal forces and deformations to which structures are subjected when subject to a rapidly changing external excitation. To describe the fundamental aspects of the dynamics of a structure it is necessary to know its natural frequencies, which identify the modal shapes of the structure, and the damping coefficients, which together with stiffness and mass are the properties of the system. The dynamic identification is based on obtaining this information as a result of an external excitation of the structure.

The different nature of this excitation gives rise to two distinct forms of modal analysis: Operational Modal Analysis -OMA- and Experimental Modal Analysis -EMA-. In OMA, the input is not controlled and is instead represented by random ambient noise -white noise- with a high frequency range. In contrast, EMA employs an artificial and controlled input, which can be generated by shakers, impact hammers, or drop weight systems.

One advantage of this analysis, both Operational and Experimental, is that it provides an integrated view of the global system's dynamic response. This is precisely why dynamic identification is also employed for the calibration of numerical models. Without real data, such models would be unable to fully represent the totality of the structure in its complexity.

A further significant application of this approach is structural health monitoring -SHM-, which enables the detection and characterisation of damage in engineered structures, thereby ensuring their structural integrity and safety. This is achieved with a monitoring network that measures changes in the intrinsic dynamic properties of the structure.

In the case of OMA, which is the analysis of interest for this study, since the ambient noise is employed as the source of excitation, the structure is susceptible to its own free vibration. This vibration can be complicated to analyse, but here modal analysis comes to the rescue, which separates the complicated vibration pattern into a set of vibration modes characterised by natural frequency, damping ratio and modal form. These modes are actually the fingerprint of a structure *(Fig. 2)*.

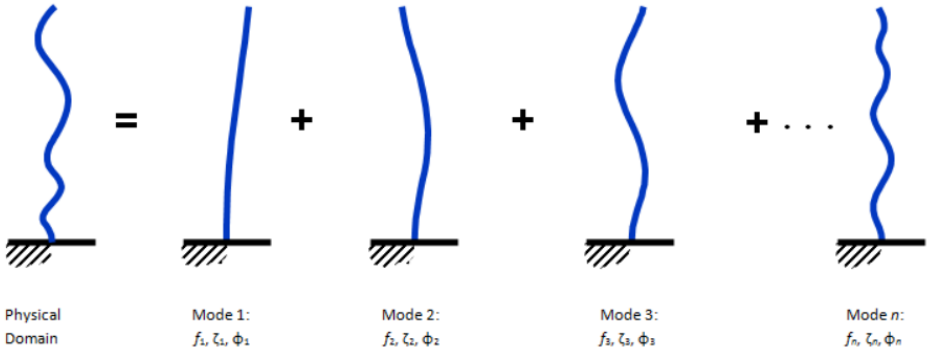

Figure 2: A visual representation of the decomposition of the vibration pattern in the vibration modes in which f_i =Natural frequency, ξ_i = Damping Ratio and Φ_i =Mode shape [svibs.com].

Further details regarding the technical aspects of modal analysis will be provided in section 2.2.7.

As mentioned in the previous paragraph, an understanding of the dynamic response of structures is also crucial for evaluating their interaction with the soil and preventing potential resonance phenomena resulting from ground motion.

2. MATERIALS AND METHODS

2.1 THE SENSORS

A seismic sensor is an instrument that measures the ground motion. In order to fully characterize the motion of a deformable body at a given point in the context of infinitesimal deformation, one needs three components of translation, six components of strain, and three components of rotation *(Cochard et al. 2006)*. Technically, such measurement is not easy to do and depends on the sensor type and its sensitivity.

Standard seismometers do not normally take rotational ground motion into account, simplifying the issue, although more and more research suggest that it is not negligible and may contribute to co-seismic structural damages *(Pham, PhD thesis, 2009)*. For this reason, the development and implementation of rotational seismometers is now gaining momentum.

As in this case, standard digital sensors were used to measure the velocity of the ground motion – velocimeters and seismometers - and its acceleration – accelerometer - only along the 3 translational directions x, y and z.

The instruments used are called Triton seismograph and Triton accelerographs and are produced by the Italian manufacturer Lunitek *(Fig.3)*.

Figure 3: Photo of the sensors taken during the surveys: left from Porto Tolle, right from Angera.

The Triton seismograph and Triton accelerograph are an integrated data acquisition and sensor system designed for applications requiring a combined and space-saving solution. They present a low seismic noise level as an excellent performance, are easy to use, equipped with an internal battery which can guarantee an autonomy of about 33 hours. Finally, they are robust and shockproof as well as vibration and weather resistant *(www.lunitek.it)*.

Technically speaking, the seismograph is a tri-component short-period velocimeter while the accelerograph is a tri-component accelerometer equipped with a MEMS - Micro Electro-Mechanical Systems - sensor.

The two types of sensors - velocimeter and accelerometer - differ in sensitivity and dynamic range. The velocimeter is much more sensitive indicatively at frequencies above 0.2 Hz and quickly becomes insensitive below this value. MEMS are sensors that, due to their low cost, low footprint -i.e., very small instruments- and increasingly high performance, can be used as a viable alternative to classical and more expensive accelerometers for identifying small local seismic event - 2<M<3 - *(Cascone et al., 2021)*, from moderate - M>4 - to high ground motion *(Boaga et al., 2019)* and for structural health monitoring *(Crognale et al.,2024)* and dynamic identification of structures *(Andò et al.,2018)*. Dynamic identification of structures focuses on low frequency ranges, and although MEMS accelerometers are cost-effective and energy-efficient, they generally have limitations at low frequencies, especially below 1 Hz. However, recent advancements have improved their performance and some studies suggest that low-noise MEMS accelerometers can now reliably capture structural frequencies as low as 0.1 Hz *(Crognale et al.,2024)*. Nevertheless, accuracy at these low frequencies may depend on sensor quality and noise level.

In *Tab.1* are reported the technical information of the sensors and the acquisition parameters used.

Table 1: Technical information about the type of sensors used.

Type	VELOCIMETER SENSOR	ACCELEROMETER SENSOR
Dynamic range	136 dB	110dB
Self noise	1Hz:< 3nm/s	0.2μg/√Hz
Sensitivity	400 V/m/s (Voltage per meter/second)	±2g
Unit	Velocity in meters per second	Acceleration in meters per second squared
Corner period	1s	/
Frequency range	1Hz-100Hz	0-500Hz
Sampling rate	200 sps (sampling per second)	200 sps (sampling per second)
InPUT RANGE	10 Vpp (Voltage peak to peak)	10 Vpp (Voltage peak to peak)
Format	MiniSEED	MiniSEED

2.2 OVERVIEW OF THE ANALYSES PERFORMED

2.2.1 RAW DATA MANIPULATION

The raw data are presented as three separate traces, one for each direction, with digital count values over time in seconds saved in MiniSEED format. The sampling interval is 5 ms. The MiniSEED format is the subset of the SEED - Standard for the Exchange of Earthquake Data- standard used for time series data. It contains the digital time-series data plus some meta information contained in the header such as station and channel ID, sample rate, and number of data points.

First of all, to be able to interpret the data, we need to convert the digital counts per second into the unit of measurement in which we are interested, i.e. velocity or acceleration.

Secondly, it is evident that the recording instrument possesses intrinsic characteristics that influence the recorded signal. These include its frequency range sensitivity and dynamic range. These conditions collectively define the instrument's intrinsic response. It is thus imperative to deconvolve the instrument's response from the recorded traces, particularly with the objective of attempting to regain the signal amplitude below the lower corner frequency of the instrument. This is of particular importance when analysing the chimney, which, due to its considerable height, may exhibit an oscillation frequency below 1 Hz, which is the lower corner frequency of the seismometer.

Phyton's Obspy package through the *trace.remove_response* function was used to perform this operation. To prevent overamplification while convolving the inverted instrument spectrum I also applied a bandpass pre-filter from 0.1 Hz to 30 Hz for Angera and from 0.005 Hz to 30 Hz for Porto Tolle *(Fig.4)*.

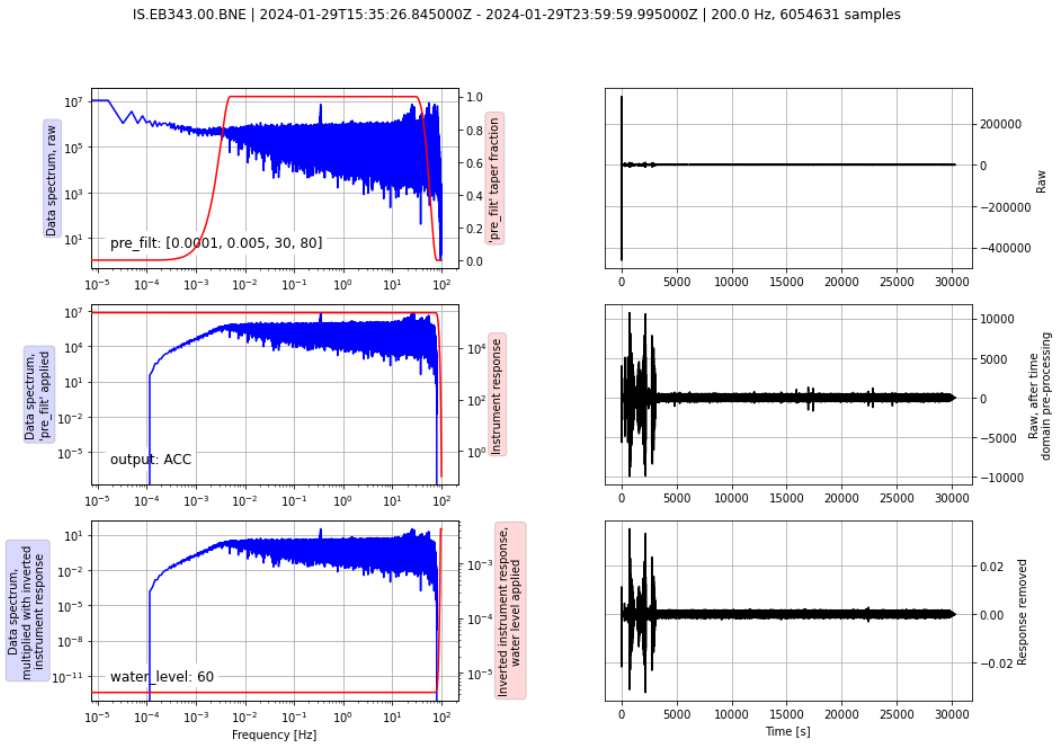

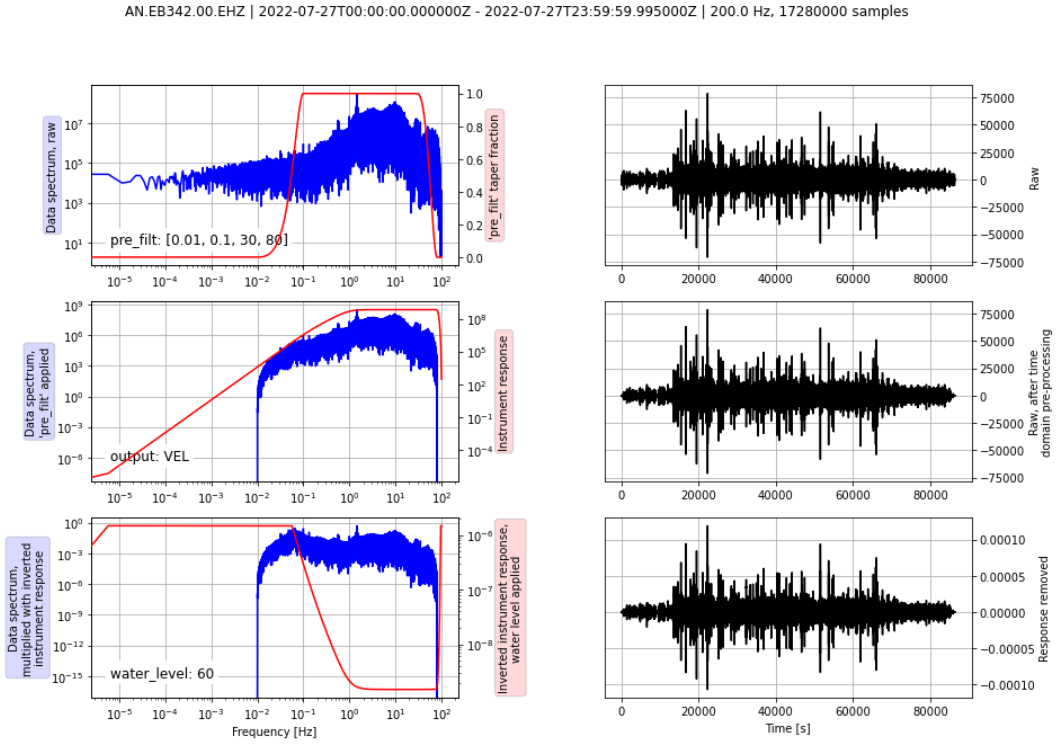

Figure 4: Steps of applying the trace.remove response function for the accelerometer from Porto Tolle (top) and the velocimeter from Angera (bottom). See how the y-values change.

Finally, the data ready to be analysed are presented as streams of traces for the entire recording period in the three directions, shown in acceleration or velocity values, depending on the sensor, as a function of time in seconds.

2.2.2 ROOT MEAN SQUARE (RMS)

The moving window Root Mean Square – RMS - was computed on the velocity and acceleration data registered by the sensors, to check the distribution of the strength of the seismic signal over time. The RMS corresponds to the square root of the mean of the sum of the squares of each data within a chosen time window. By squaring, RMS avoids canceling out positive and negative deviations, ensuring that only the magnitude contributes to the final measure. On the other hand, squaring also emphasizes the difference

between values, so that the final measurement is biased by higher amplitude impulse signals. Since this analysis was carried out in support of other analyses and is not of primary interest, these inaccuracies are not to be considered relevant.

2.2.3 H/V SPECTRAL RATIO (HVSR)

The Horizontal to Vertical Spectral Ratio – HVSR -, also known as the Nakamura method after the Japanese author who first proposed it *(Nakamura. 1989)*, is a simple and fast method for obtaining information on the dynamic characteristics of soil and structures.

The main applications of HVSR are site classification, site effect study, mineral exploration and acquisition of the underground average shear wave velocity structure (Xu and Wang, 2021). In this study, the main objective of using this method was to recover the seismic ground response and the structure response expressed by the natural fundamental frequency.

This simple and cost-effective method requires no special equipment. All that is needed is to measure ambient noise in the three directions from a single recording station.

Its theoretical basis rests on two assumptions: first, the H/V Fourier spectral ratio is 1 at the bedrock, that is, the horizontal and vertical waves travel equally on bedrock and second, after the seismic wave propagates from the bedrock to the surface, the vertical component is unchanged, that is, the vertical transfer function is considered as 1 *(Xu and Wang, 2021)*. Based on these assumptions, it can be posited that the HVSR would be analogous to the horizontal transfer function, defined as the ratio between the horizontal amplitude spectra at the bedrock and at the surface. Consequently, the HVSR can be used to strictly reveal the fundamental frequency of the horizontal component in a given site.

Anyway, the results obtained can be influenced by various factors, especially with regard to the use of ambient noise as a source. Because of the randomness of the noise wave field, the position and kind of source might change, thus affecting the estimation of HVSR. In addition, the installation of the equipment has a considerable impact on the quality and variability of HVSR measurements *(Molnar et al. 2022)*.

From a practical point of view the signal is divided into windows whose length can be chosen and tapered individually using the Konno-Ohmachi smoothing method. For each window, the amplitude spectra of the three components are computed using a Fast Fourier Transform – FFT - algorithm. As a result, the average spectral ratio of horizontal-to-vertical noise components is thus calculated. The H/V plots were processed using the GEOPSY software package (www.geopsy. org).

2.2.4 POWER SPECTRAL DENSITY (PSD)

Power Spectral Density analysis – PSD -, as the name implies, is used to characterise the power of a time series signal as a function of frequency.

Phyton's matplotlib module using Welch's average periodogram method was used to calculate it.

The Welch method is carried out by dividing the time signal into successive overlapping segments, window the data segments, forming the periodogram for each block, i.e., performing the Discrete Fourier Transform calculation, followed by computing the squared magnitude of the result and averaging, which reduces the variance of the individual power measurements *(Jwo et al. 2021)*.

The two most important parameters in this calculation are: the length of the segment on which the Discrete Fourier Transform is calculated - the NFFT -

and the choice of window type to be applied to the data prior to compute the periodogram.

Regarding the NFFT parameter, it will be evaluated in the presentation of the results, while the default Hanning window was used as window type. The Hanning window possesses better suppression capability on spectrum leakage, which is caused by the non-coherent sampling in the practical acquisition system – i.e., the number of periods of the time serie acquired is not an integer and so the endpoints are discontinuous -, while the frequency resolution is relatively good, hence suitable for general frequency estimation of signals with low Signal to Noise Ratio *(Jwo et al. 2021)*.

2.2.5 SPECTROGRAM

Spectrogram analysis also relates to signal frequency and in this case refers to the evaluation of the frequency content of a signal over time. In this representation of the signal one axis represents time, the other represents frequency, and the color or intensity represents the magnitude of the signal at each frequency and time.

Similar to PSD analysis, the time series signal is split into parts that are processed using the Fast Fourier Transform – FFT - and thus the spectrogram appears as a moving sequence of local spectra for the signal.

To analyse this data, the *spectrogram* function of Phyton's Obspy package was used, with 90% overlap of the signal segment and a maximum sliding window size of 4096 points as the default.

2.2.6 HODOGRAM

In the hodogram analysis, the frequency of the signal is no longer directly analysed; however, it remains a significant factor to be considered. In fact, the

analysis is employed to examine the directionality of the signal to which a bandpass filter is previously applied on the frequency bands of interest.

The hodogram represents the particle movement in the three directions North-South, East-West and in the vertical direction, which is not relevant in our case. The analysis is performed over a limited time window on the order of minutes or seconds to gain insight into the main motion of the structure.

The values, corresponding to the numerical data collected by the sensors in that small time interval, can be represented as points in a linear Cartesian graph, which highlights the shapes of the movement. Alternatively, the values can be converted to polar coordinates and depicted by a frequency diagram, known as a rose diagram or a polar coordinate histogram, which, in contrast, highlights the direction of the movement more clearly.

2.2.7 MODAL ANALYSIS

The objective of this analysis is to identify the dynamic response of the structure due to an external excitation, which in this study is ambient noise. To this end, Operational Modal Analysis (OMA) was performed.

As discussed in greater detail in the introduction, this analysis enables the determination of the oscillation eigen-frequencies and vibration modes -i.e. modal forms or shapes- of structures, which in this case are the two tall buildings.

This was achieved through the use of the ARTeMIS Modal Pro software which employs the Singular Value Decomposition -SVD- method for the identification of the vibration modes of structures.

The Singular Value Decomposition is a linear algebra analysis related to the decomposition or factorisation of matrices. The basic ideas behind SVD is to take a high dimensional, highly variable set of data points and reducing it to a

lower dimensional space that exposes the substructure of the original data more clearly and orders it from most variation to the least *(Baker, 2005)*. The SVD theorem states that a rectangular matrix A can be decomposed into the product of three matrices with different properties i.e. $A = UDV^T$ where U is an orthogonal matrix containing the left singular vector, D is a diagonal matrix containing the singular values and V^T is the transpose of an orthogonal matrix containing the right singular vector.

In essence, the software transforms time data into the frequency domain via the FFT, thus obtaining frequency spectra for each sensor. The responses of a pair of sensors at a time are cross-correlated at a specific frequency and the values are reported in the spectral matrix. Subsequently, the spectral matrix is decomposed using the Singular Value Decomposition where the singular values obtained represent the magnitude of the energy present at each frequency in the dominant modal directions. The SVD lines are the graphical representation of the singular values obtained from the SVD as a function of frequency and power. The peaks that can be identified in these lines thus represent the frequencies at which the energy is most concentrated in a specific mode of vibration. These frequencies are to be identified as the modal frequencies of the structure.

A window on the ARTeMIS modal screen *(Fig.5)* displays these SVD lines as a function of frequency and power while another one allows the user to view animations of the vibration modes of the selected frequencies. Another window presents the MAC -Modal Assurance Criterion- values used to identify the main modal shapes and distinguish between similar modes. The MAC is a numerical value between 0 and 1 that quantifies the similarity between two modal forms. A value of 0 indicates that the forms are completely different, whereas a value of 1 indicates that the forms are identical. As illustrated in *Fig.5*, the values are presented in columns, with the varying heights corresponding to distinct MAC values.

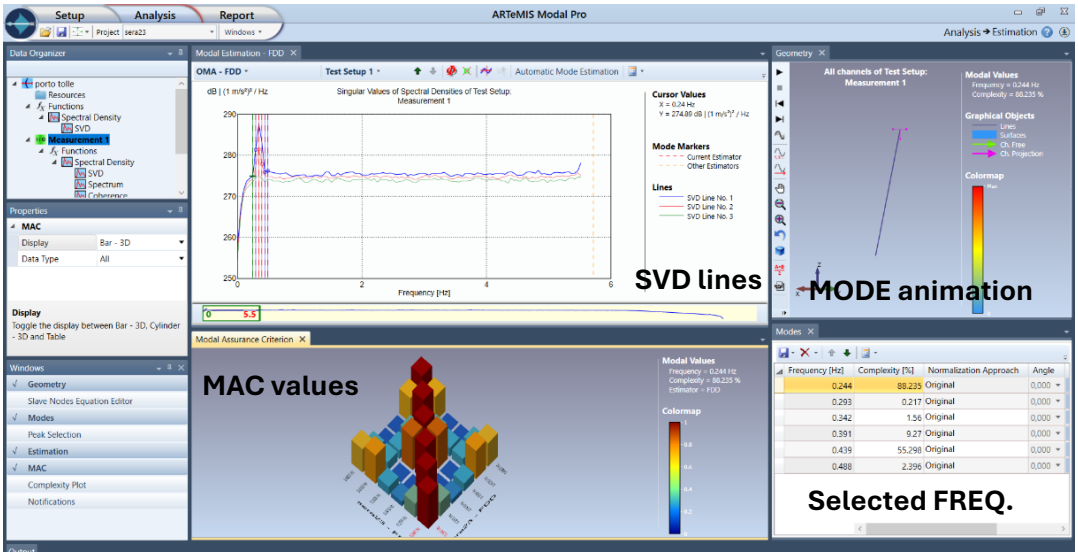

Figure 5: Screenshot of the ARTeMIS modal screen.

3. CASE STUDIES

Two very different structures were analyzed in this study. The buildings differ in numerous aspects that, to varying degrees, influence their dynamic behavior. Their common characteristic is that they are both identifiable as tall buildings with greater vertical than horizontal elevation.

3.1 PORTO TOLLE CHIMNEY

The first tall building to be investigated is the chimney of the former Porto Tolle thermoelectric power plant operated by Enel S.p.A. and currently decommisioned. The chimney is located on the Po River Delta in the island of Polesine Camerini, originated around the year 1759 when a branch of the river, the Po di Tolle, split to form the Po di Pila. The island is located in the province of Rovigo, Veneto *(Fig.6 and Fig.7)*.

Figure 6: Photo of the former power plant in Porto Tolle.

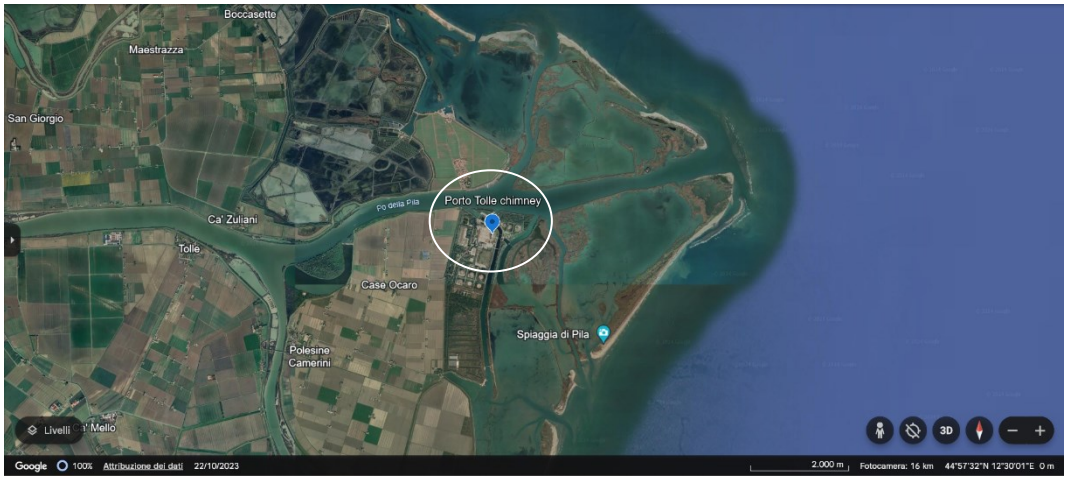

Figure 7: Location of the former Porto Tolle power plant [Google Earth, 2023].

The power plant, which was divided into four groups, was built between 1980 and 1984 and had a total nominal capacity of 2,640 MW, capable of generating around 8% of Italy's electricity needs.

In connection with the operation of the Porto Tolle power plant, in the years between 1998 and 2005, Enel was condemned for failing to comply with pollutant emission limits *(Trib. Rovigo, 31 marzo 2014)*. Despite this, production was only permanently halted in January 2015. A last attempt to convert the previously dense fuel oil-fired power plant facility to coal was made in 2011, but was unsuccessful.

The power plant is currently undergoing a conversion through Enel's Futur-e project *(Enel, 2016)*. This involves the decommissioning and reclamation of the site, with the intention of creating a tourist village in its place.

Regarding the chimney of the industrial site, the subject of these analyses, it is 250 meters high and composed of four ducts, so that pollutant particles are effectively dispersed in the upper atmosphere. The structure is circular in shape and rests on a foundation consisting of 415 poles of 50 cm diameter *(Fig.8; Enel, 1976)*. This building, that is made of reinforced concrete, turns out to be the tallest non-metallic structure in Italy.

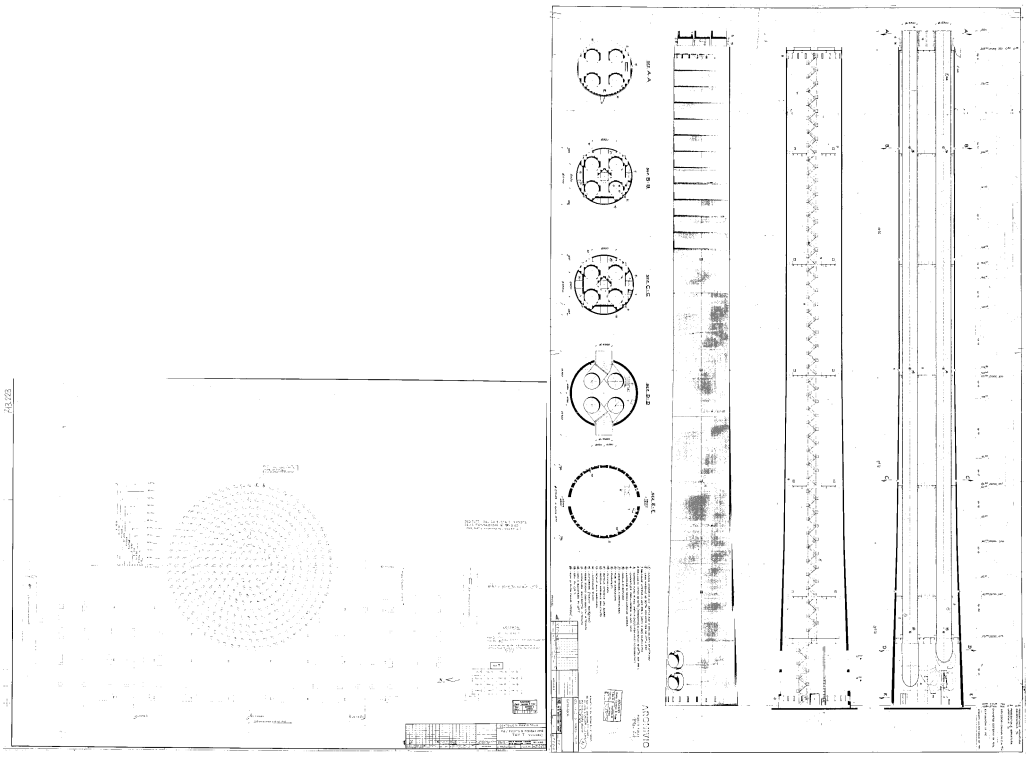

Figure 8: Archive drawings of the Porto Tolle chimney project and its foundations [Enel,1976].

Regarding the soil on which the foundations rest, approximately one month prior to the seismic monitoring of the structure, a geognostic investigation was conducted by *Georicerche S.r.l.* in the former power station. This investigation comprised two continuous core drilling surveys in the north and south sides of the chimney, borehole tests, core sampling and subsequent laboratory analyses.

The results of the core drilling show the lack of strong impedance contrasts in the first 50 m -maximum core depth- where the soil is mainly composed of sands and silty clay *(Georicerche, 2024)*. These results are further corroborated by the MASW - Multichannel Analysis of Surface Waves - and ReMi - Refraction Microtremor - analyses carried out by *Isamgeo S.r.l.* during the same period of the seismic monitoring *(Isamgeo, 2024)*.

As mentioned before, the tower was monitored on the 29th and 30th of January 2024. A triaxial accelerometer and velocimeter were placed on the top of the chimney, while five other velocimeters were placed on the ground surface at increasing distances from the tower *(Tab.2 and Fig.9)*.

Table 2: Table of the characteristics of sensor acquisitions. Start and end times are reported in UTC Time.

SN	Type	Distance from the tower	Start	End	Duration
EB343	Acc	0m - Top	29/1/2024 15:35:26	31/1/2024 06:26:50	1 day/s 14:51:24
EB587	Vel	0m - Top	29/1/2024 15:35:37	30/1/2024 15:12:20	0 day/s 23:36:43
EB696	Vel	0m - Base	29/1/2024 16:09:10	30/1/2024 16:14:36	1 day/s 00:05:26
EB693	Vel	190m	29/1/2024 16:36:40	30/1/2024 16:10:46	0 day/s 23:34:06
EB694	Vel	290m	29/1/2024 16:30:50	30/1/2024 15:36:08	0 day/s 23:05:18
EB206	Vel	445m	29/1/2024 16:50:24	30/1/2024 17:20:21	1 day/s 00:29:57
EB695	Vel	590m	29/1/2024 17:24:12	30/1/2024 17:38:07	1 day/s 00:13:55

Figure 9: Position of the sensor.

The chimney is made of reinforced concrete and although very tall, the structure was built to be robust and durable. The placement of a single sensor on the top should make it possible to obtain dynamic information on the main vibration modes of the structure. The presence of construction-free land around the chimney allowed the easy placement of the sensors on the ground. This also permitted an investigation of the frequencies exhibited by the surrounding terrain, with a view to assessing any influence or correlation between these frequencies and those of the tower.

3.2 ANGERA BELL TOWER

The second structure analysed is the bell tower of the church of Sant'Alessandro, Sisinnio e Martirio located in the town of Angera on the eastern shore of Lago Maggiore in the province of Varese, Lombardia *(Fig.10 and Fig.11)*.

Figure 10: Photo of the church of Sant'Alessandro, Sissinio e Martirio.

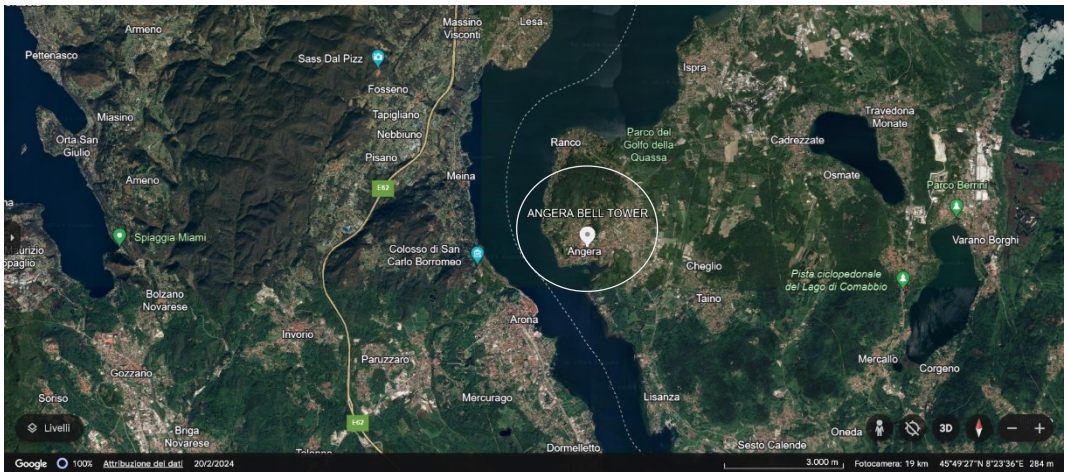

Figure 11: Location of the Angera bell tower [Google Earth, 2024].

The complex as seen today is the result of a reconstruction taken place between 1580 and 1585 of the former church that was the seat of a very large parish church that included the surrounding areas. An exception of this reconstruction is the bell tower, which dates back to the Romanesque period, although the clock and belfry were added during the Baroque period.

The bell tower has a rectangular cross-section with a tile roof topped with a lantern. The building leans against the bottom of the south side of the church and is surrounded by other buildings. Regarding the construction material, a recent archaeological investigation on the perimeter of the south wall and bell tower have confirmed that the current structure was built by reusing masonry from an older period, probably early Christian -5th/7th century- *(Mariotti and Simonotti, 2001-2002)*.

The seismic monitoring of the building took place in the summer of 2022 from the 23th of July to the 6th of September. A total of four triaxial velocimeters were used, positioned at different heights at various floors of the tower: ground floor, second floor, fourth floor and sixth floor. On the highest floor, a triaxial accelerometer was additionally installed next to the velocimeter *(Tab.3, Fig.12 and Fig.13)*.

Table 3: Table of the sensors with their respective name, type and position.

SN	Type	Height of the bell tower
EB343	Acc	6th floor - 20.35m
EB342	Vel	6th floor - 20.35m
EB208	Vel	4th floor - 13.15m
EB462	Vel	2nd floor - 6.65m
EB206	Vel	ground floor - 0m

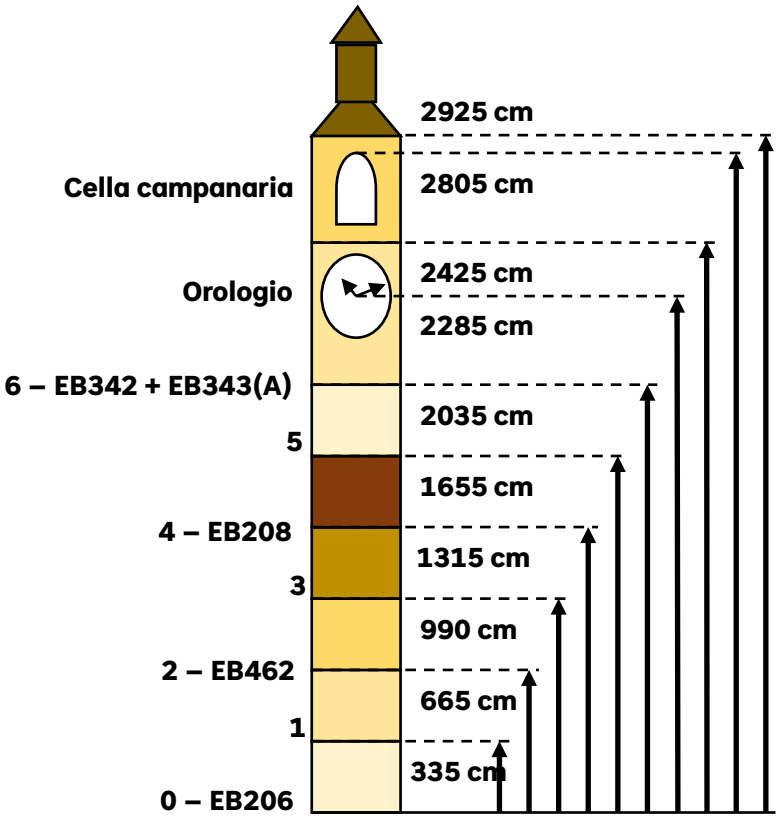

Figure 12: Illustration of the bell tower (not in scale).

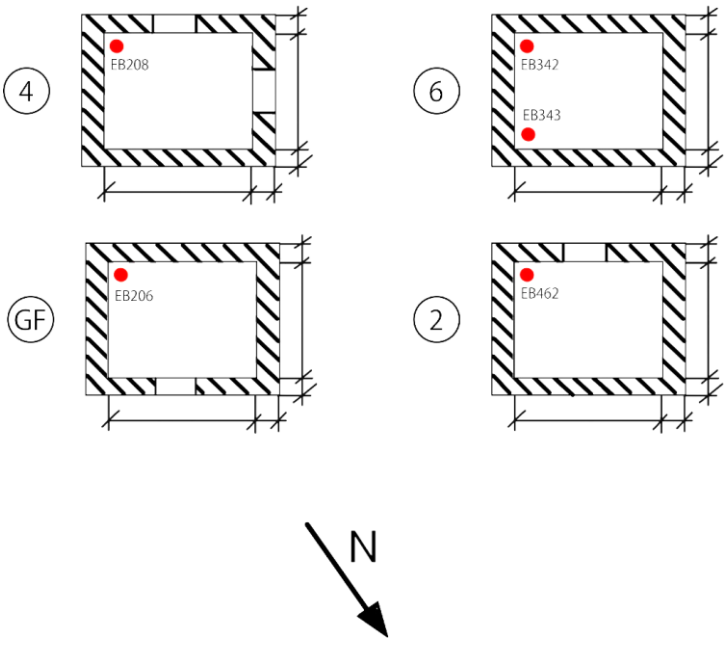

Figure 13: Position and orientation of the sensor inside the bell tower. All sensors are oriented north.

Unfortunately, not all data were available for the entire recording period of the five sensors. Especially the EB208 sensor, located on the 4th floor, experienced some problems after two weeks from the installation and it was removed. Also for the EB206 sensor, on the ground floor, the data were not available for about twelve days *(Tab.4)*.

Table 4: Table of data availability for different days and sensors. Green: data available, red: data not available, yellow: data partially available.

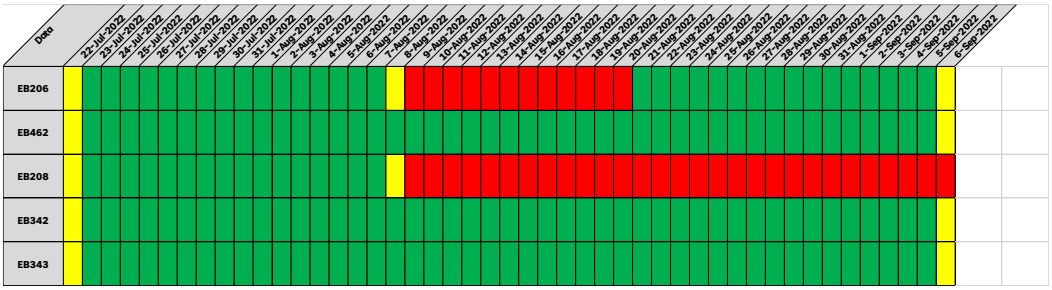

4. RESULTS

This chapter presents the results obtained from the six analyses described in chapter 2 for the two case studies, the chimney of Porto Tolle and the bell tower of Angera, respectively. All graphs are presented in UTC Time -Universal Time Coordinates-. The local time for Porto Tolle, where the records were taken during winter, is equal to CET -Central Europe Time- (UTC+1). The local time for Angera, where the recordings were taken in summer, instead corresponds to CEST - Central Europe Summer Time- (UTC+2).

4.1 PORTO TOLLE CHIMNEY

4.1.1 RMS

The RMS analysis was conducted exclusively of one horizontal component of the velocimeter positioned at the top of the tower -EB587- for the entire recording period -23 hours-. This was done to ascertain the signal strength and, consequently, to identify the periods during which the tower is subjected to the greatest stress and when the signal is least intense.

The analysis was conducted using two distinct temporal windows: a 30-minute interval and a 10-minute interval *(Fig.14)*.

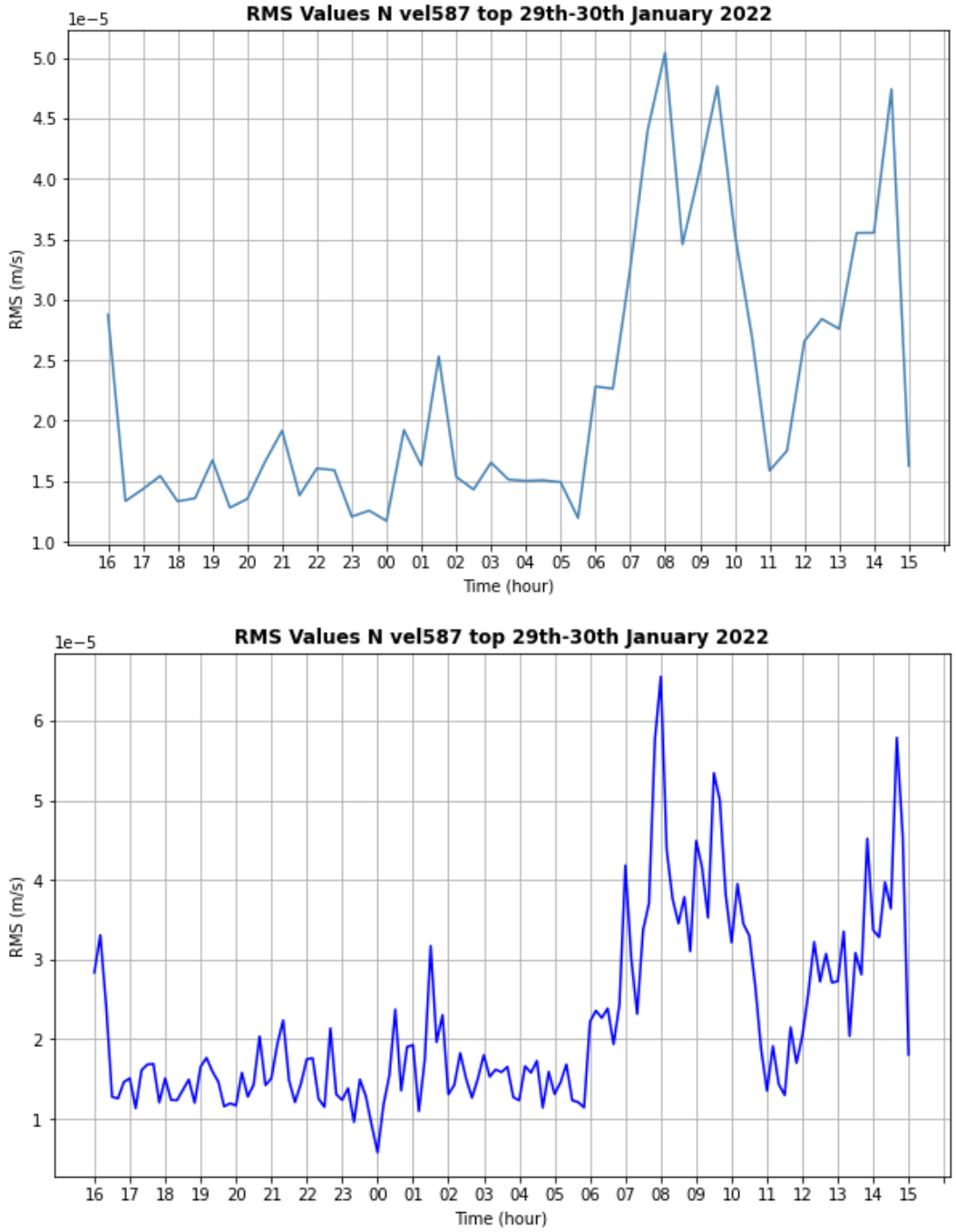

Figure 14: RMS amplitude calculated for the EB587 velocimeter at the top of the tower for the 23 hours of recording obtained over a 30-minute time window (top) and a 10-minute time window (bottom) for one horizontal component.

The use of a 10-minute time window permits the generation of a more detailed graph. Nevertheless, as observed in the two images, the general trend remains unaltered. It can be seen that the largest amplitudes are from the morning at 6 a.m. until approximately 3 p.m., with a decrease between 11 a.m. and 12 a.m. UTC Time. Converted to CET local time -UTC+1- this amplitude trend appears to almost align with standard working hours, likely due to the reclamation and redevelopment work in the area during the seismic monitoring, which also employs heavy machinery.

4.1.2 HVSR

The HVSR was calculated for all sensors, including accelerometer, for the entire recording time. The window length used is 120s. *Fig.15* shows the results obtained from the sensors on top of the tower to the most distant sensor.

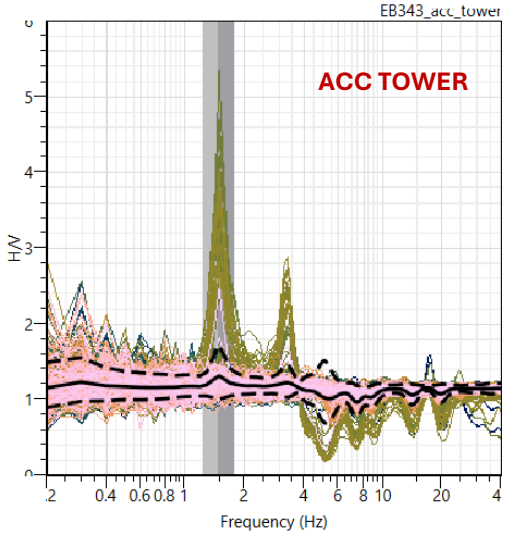
EB343_acc_tower
ACC TOWER
H/V
Frequency (Hz)

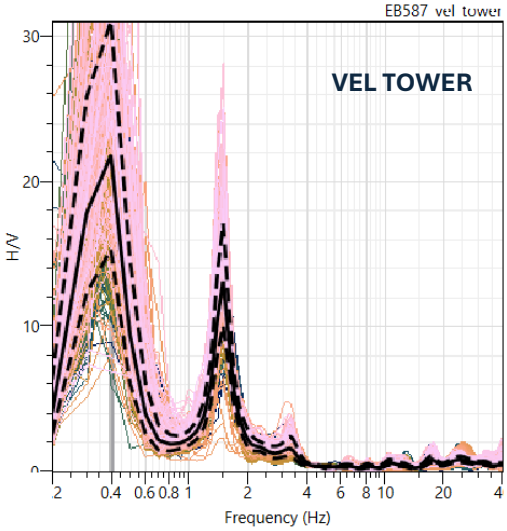
EB587_vel_tower
VEL TOWER
H/V
Frequency (Hz)

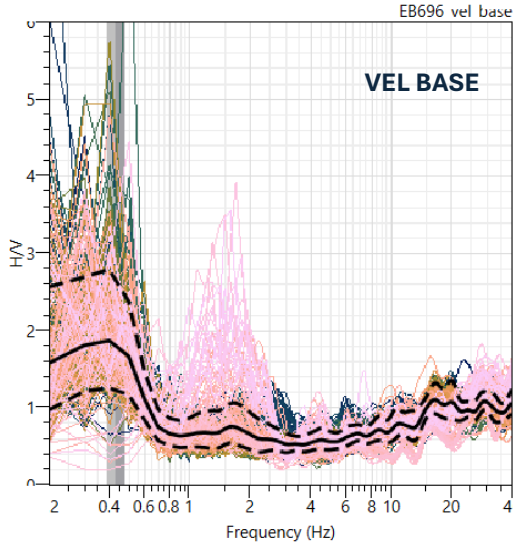
EB696_vel_base
VEL BASE
H/V
Frequency (Hz)

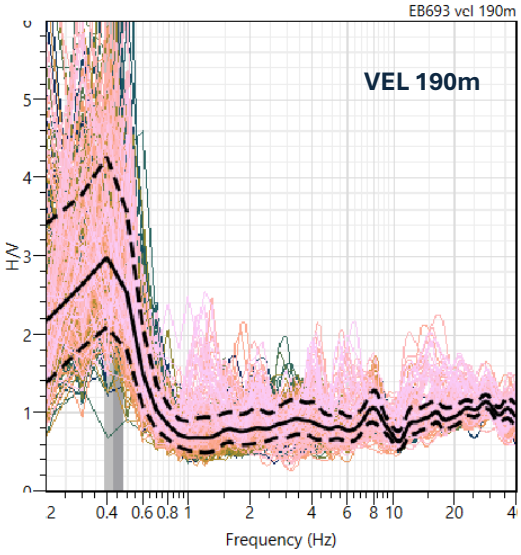
EB693_vel_190m
VEL 190m
H/V
Frequency (Hz)

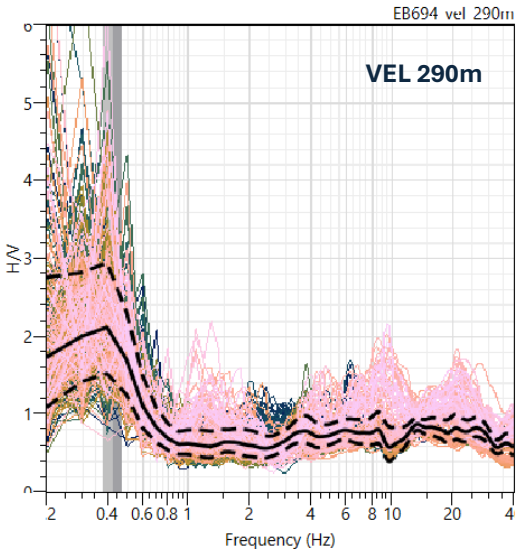
EB694_vel_290m
VEL 290m
H/V
Frequency (Hz)

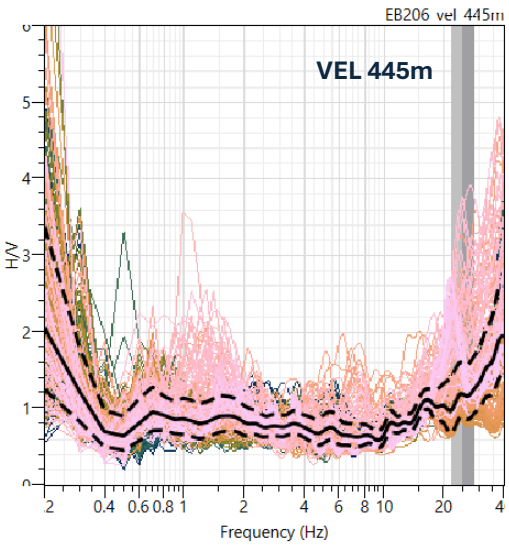
EB206_vel_445m
VEL 445m
H/V
Frequency (Hz)

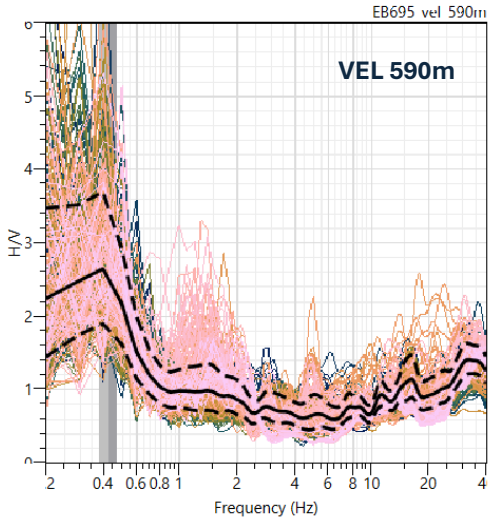

Figure 15: H/V spectral ratio of all the sensors in Porto Tolle for the entire recording tim. The colored lines represent the HVSR obtained for each time window, the continuous black line represent the average and the dotted lines represent the standard deviation.

The velocimeter situated at the top of the tower clearly reveals two peaks with higher amplitudes than those observed in the other velocimeters. The first peak exhibits frequencies of approximately 0.4 Hz, while the second peak is observed at around 1.5 Hz. In the other velocimeters from the base of the tower up to a distance of 590 meters, the two peaks are no longer as clearly identifiable but, an increase in amplitudes below 0.6 Hz is evident.

Regarding the accelerometer situated at the top, the peak occurring at approximately 1.5 Hz is clearly identifiable, as is a secondary peak at approximately 3.5 Hz. This second peak is also visible in the velocimeter on top of the tower although to a lesser degree due to the difference in scale used. In contrast, the 0.4 Hz peak of the velocimeter is not visible in the accelerometer.

Nevertheless, when the HVSR for some sensors is calculated for a shorter time interval, rather than for the entire recording period, it becomes evident that the tower's excitation and the occurrence of peaks vary over time. A

comparison with the RMS analysis reveals that when the signal at night is weaker, the HVSR of these sensors doesn't exhibit any well-defined peaks. Conversely, when the tower is under greater stress, as is the case during the morning and afternoon, spikes at higher frequencies are clearly visible. *Fig.16* and *Fig.17* illustrate this phenomenon for the accelerometer located at the top of the tower and the velocimeter situated at the base, respectively.

As explained in Section 2.2.3 this is due to the randomness of ambient noise that varies over time and affects the estimation of HVSR. In this instance, the observed variability is not entirely unpredictable, but rather correlated with the ongoing operational works in the area. However, this phenomenon is not present in the velocimeter situated on the top, which throughout the recording period clearly exhibits the two peaks.

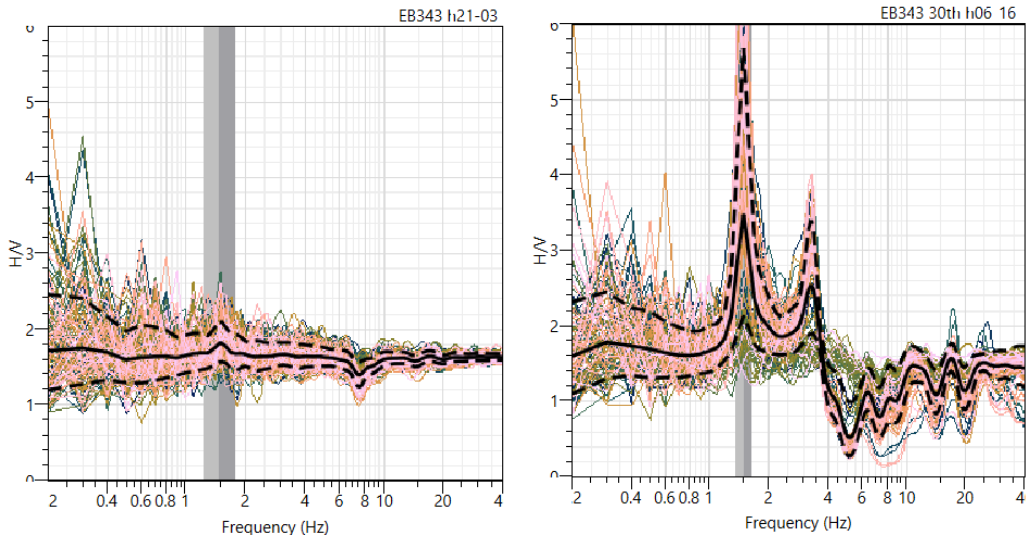

Figure 16: HVSR of the accelerometer on the top of the tower for two different time intervals; from 9 p.m. until 3 a.m.UTC (left) and from 6 a.m. to 4 p.m. UTC (right)

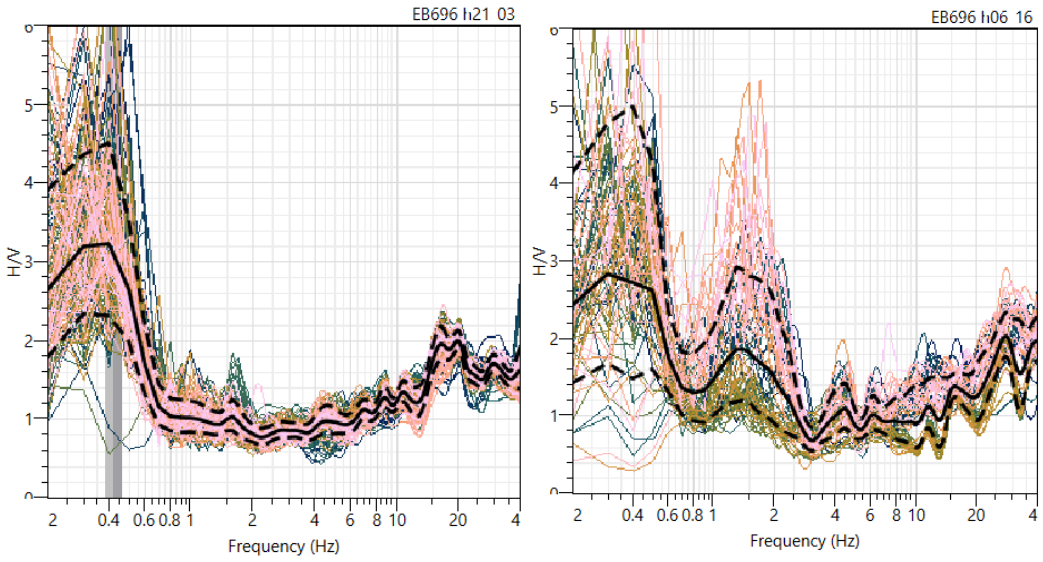

Figure 17: HVSR of the velocimeter at the base of the tower for two different time intervals; from 9 p.m. until 3 a.m.UTC (left) and from 6 a.m. to 4 p.m. UTC (right).

4.1.3 PSD

The PSD analysis was mainly concentrated on the two sensors situated on the top of the tower: the EB343 accelerometer and the EB587 velocimeter. Before performing the analysis for the velocimeter, a bandpass filter between 0.25Hz and 25Hz was applied to the trace given the low sensitivity of the sensor below 0.2Hz. The analysis was conducted on the recording interval showing the least noise, namely the night of January 29th-30th. The results obtained for the two horizontal directions, namely north-south and east-west, for the accelerometer and the velocimeter at the top of the tower, respectively, are presented in *Fig.18* and *Fig.19*.

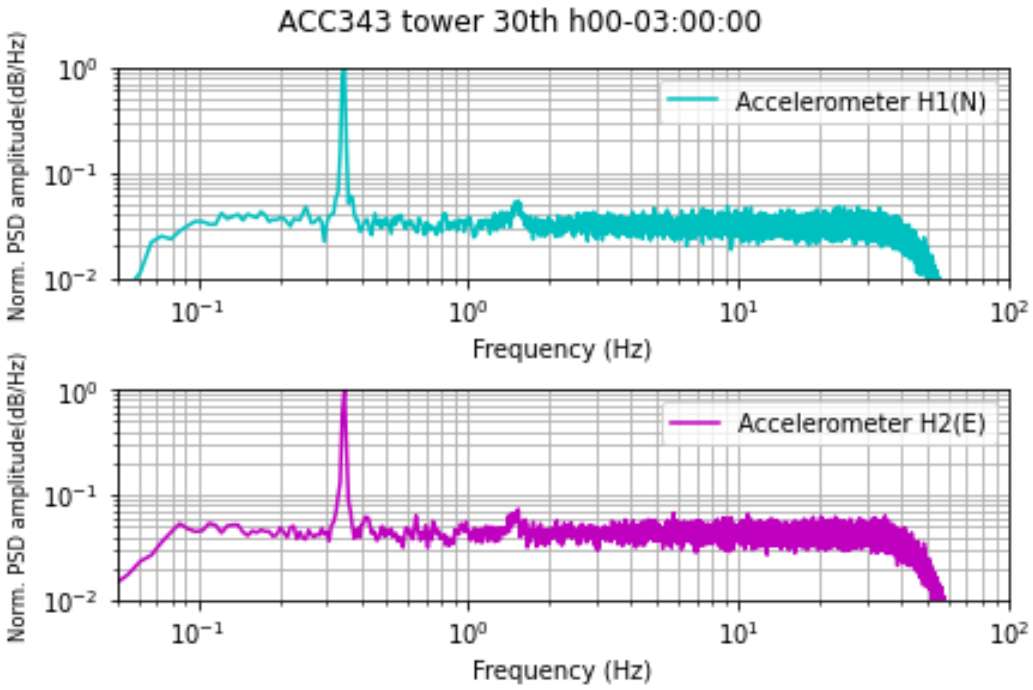

Figure 18: Normalized -by the maximum- PSD for the accelerometer EB343 at the top of the tower for the two horizontal directions, namely north-south and east-west.

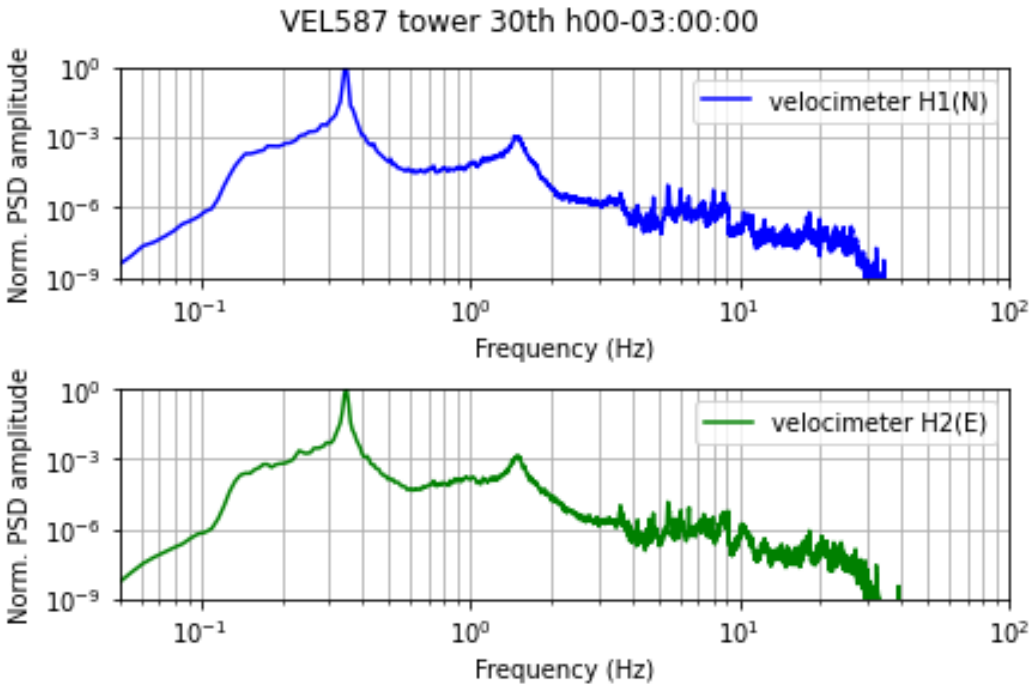

Figure 19: Normalized PSD for the velocimeter EB587 at the top of the tower for the two horizontal directions, namely north-south and east-west.

In both the accelerometer and velocimeter, the peak between 0.3 Hz and 0.4 Hz is clearly discernible. Conversely, the second peak around 1.5 Hz is more visible in the velocimeter and less visible in the accelerometer. However, as evidenced by the HVSRs, if the PSD is calculated for the accelerometer in the time interval where the signal is strongest, the higher frequency peaks emerge *(Fig.20)*.

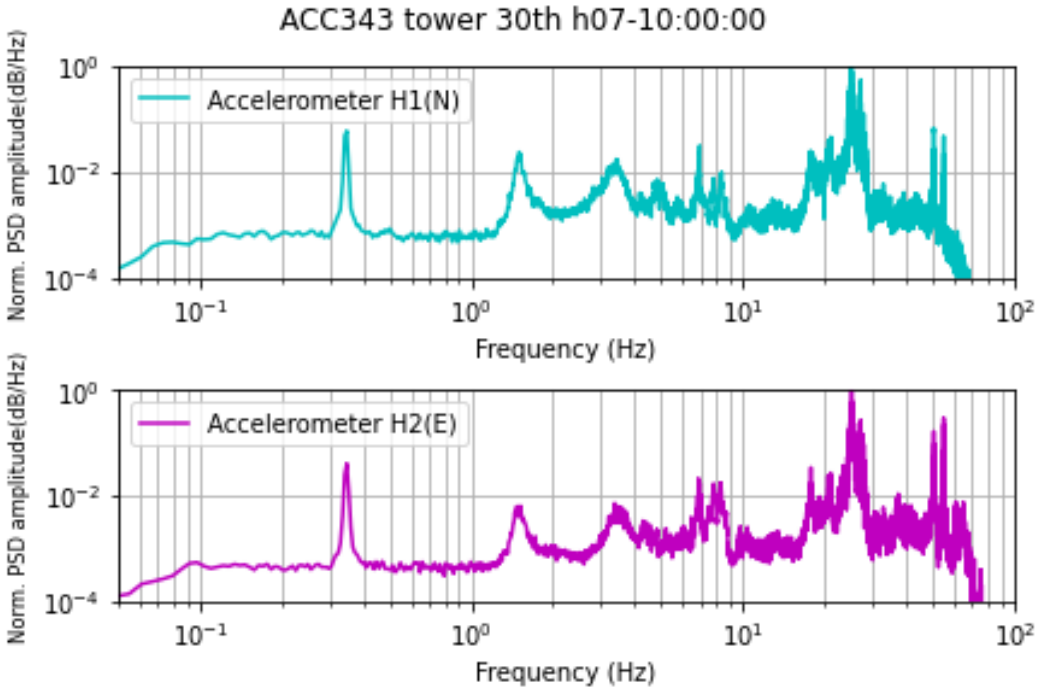

Figure 20: Normalized PSD for the accelerometer EB343 on the top of the tower calculated on the morning of January 30th.

As previously mentioned in section 2.2.4, the selection of the NFFT value, i.e., the length of the Fourier transform, involves a few considerations. This is particularly relevant in the case of the Porto Tolle chimney, where the peaks are situated at very low frequencies below 1Hz.

The value of NFFT reflects the length of each individual PSD analysis window. To analyze a peak around 0.3Hz, which is the peak value shown by the previous analysis, this window must contain at least one period of it, which corresponds to 3.3s -i.e. $1/0.3Hz$-. In 3.3s with a sampling rate equal to 200, 660 samples are analyzed. This is the minimum necessary value of NFFT. However, the use of NFFT values as a power of two is a common practice used to enhance the efficiency of computational process of the FFT algorithm. In this case then, the first power of two greater than 660 is 2^{10} i.e. an NFFT equal to 1024.

As evident from *Fig.21*, which depicts the PSDs calculated for the EB587 velocimeter with varying NFFTs, the peak between 0.3 Hz and 0.4 Hz emerges with an NFFT of 2048 – i.e. 2^{11}-. This demonstrates that the theoretically calculated value of 2^{10} is insufficient for discerning the peak and that, from a practical point of view, a larger value is needed.

As the spectral resolution increases, the peaks become more pronounced but the PSDs also becomes increasingly noisy. An intermediate value of NFFT, equal to 32768 -i.e. 2^{15}-, was selected for the PSD analysis presented in the previous and future PSD graphs.

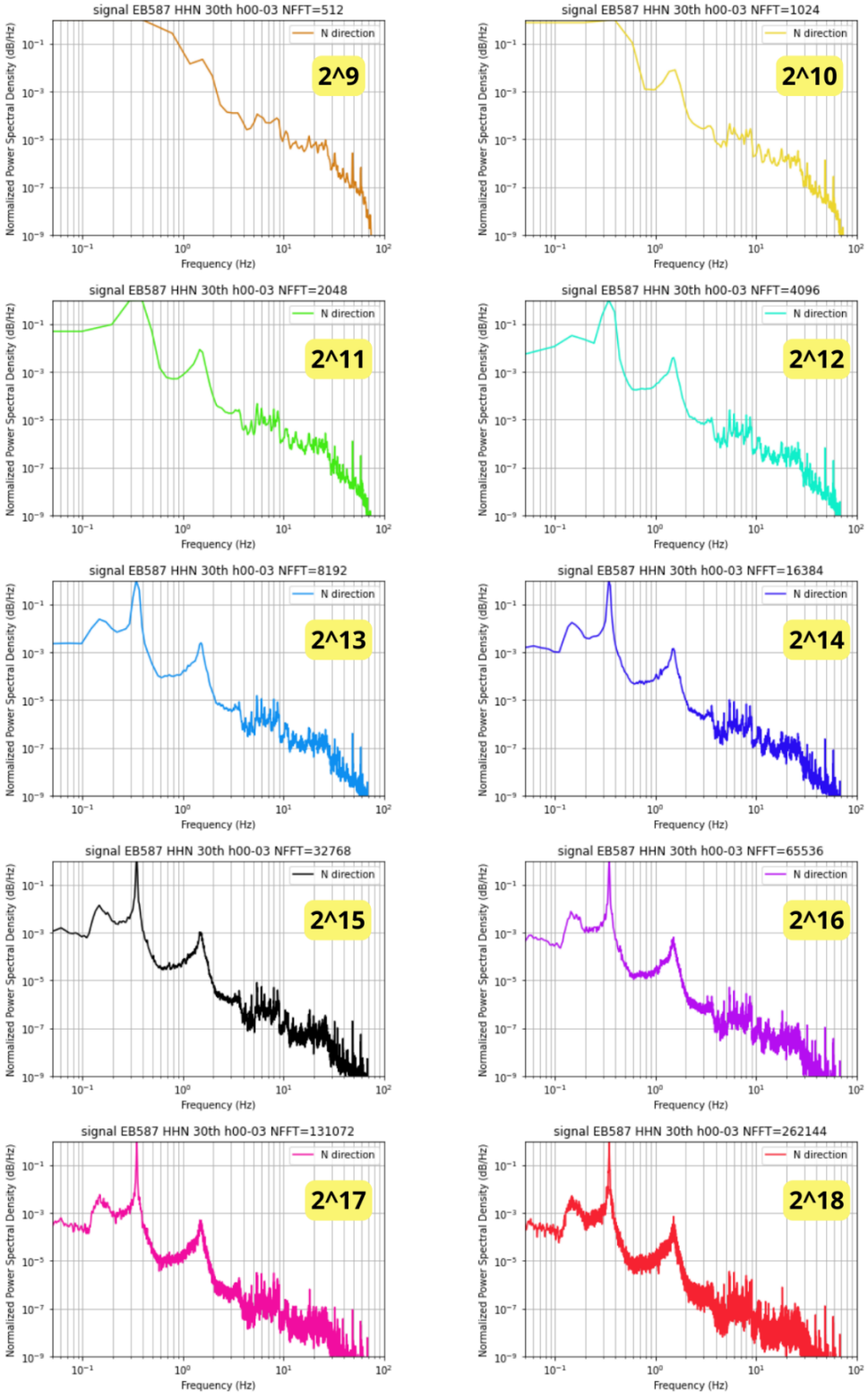

Figure 21: Normalized PSD calculated for the velocimeter on the top of the tower for just one horizontal direction with increasing values of NFFT.

The final analysis of the PSD presented is a comparison between the PSD obtained from the various velocimeters illustrated in *Fig. 22*. It is evident that the two distinct peaks observed at the top of the tower exhibit a gradual decline in amplitude from the sensor at its base, becoming undetectable as the distance from the tower increases. This phenomenon is analogous to the behavior observed in the HVSRs.

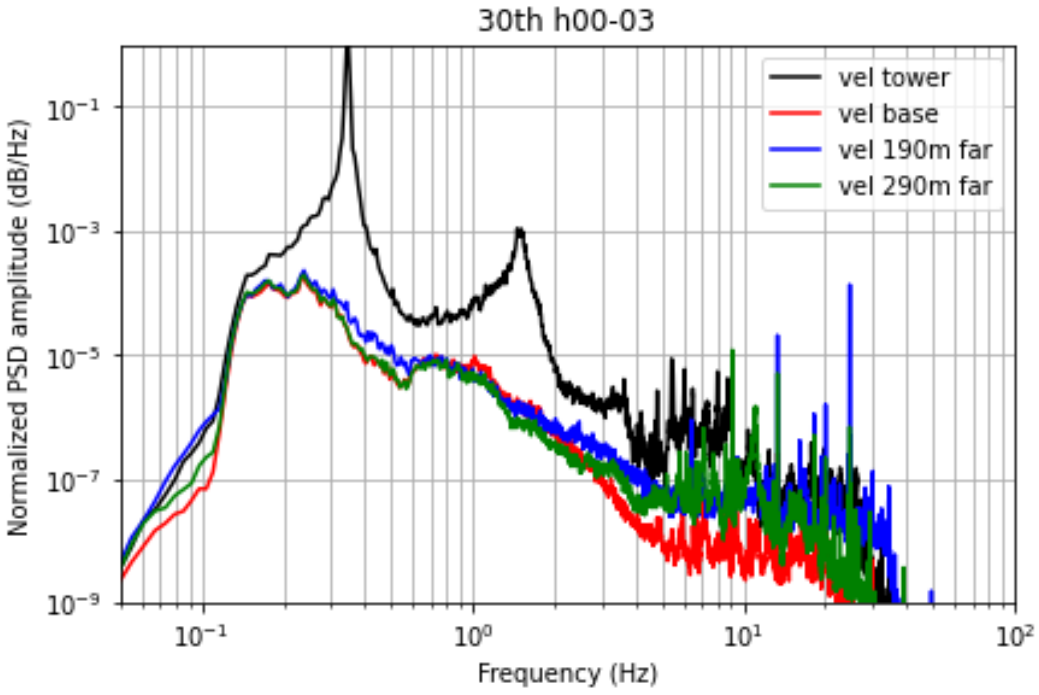

Figure 22: Comparison of the PSD for one horizontal direction from different velocimeters.

4.1.4 SPECTROGRAM

The spectrograms were calculated for all sensors, including the accelerometer, for almost the entirety of the recorded time and were calculated for all the directions registered by the sensors. However, as the results obtained from the two horizontal directions are similar and the results from the vertical direction have no apparent meaning, only the spectrograms obtained for the horizontal direction north-south are presented here (*Fig.23)*.

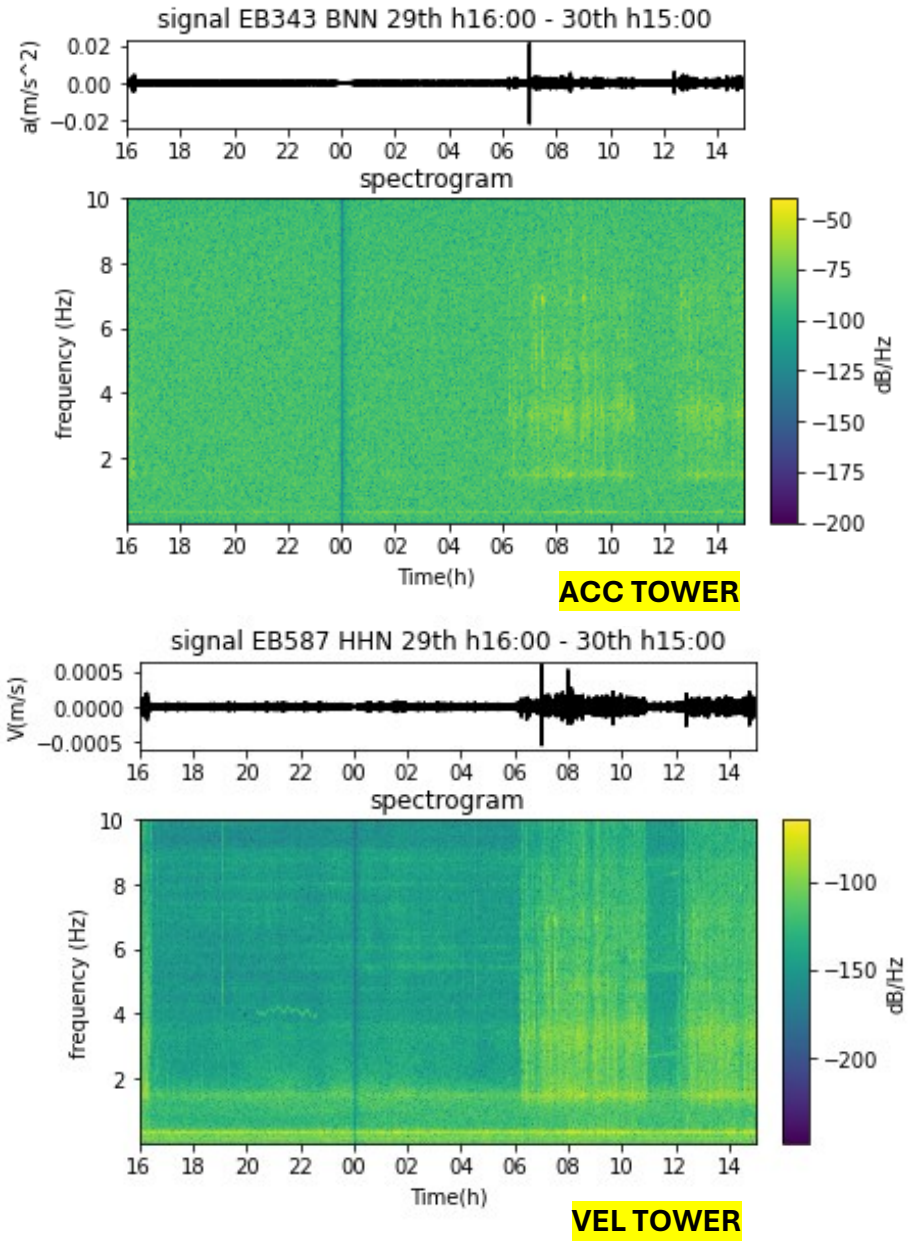

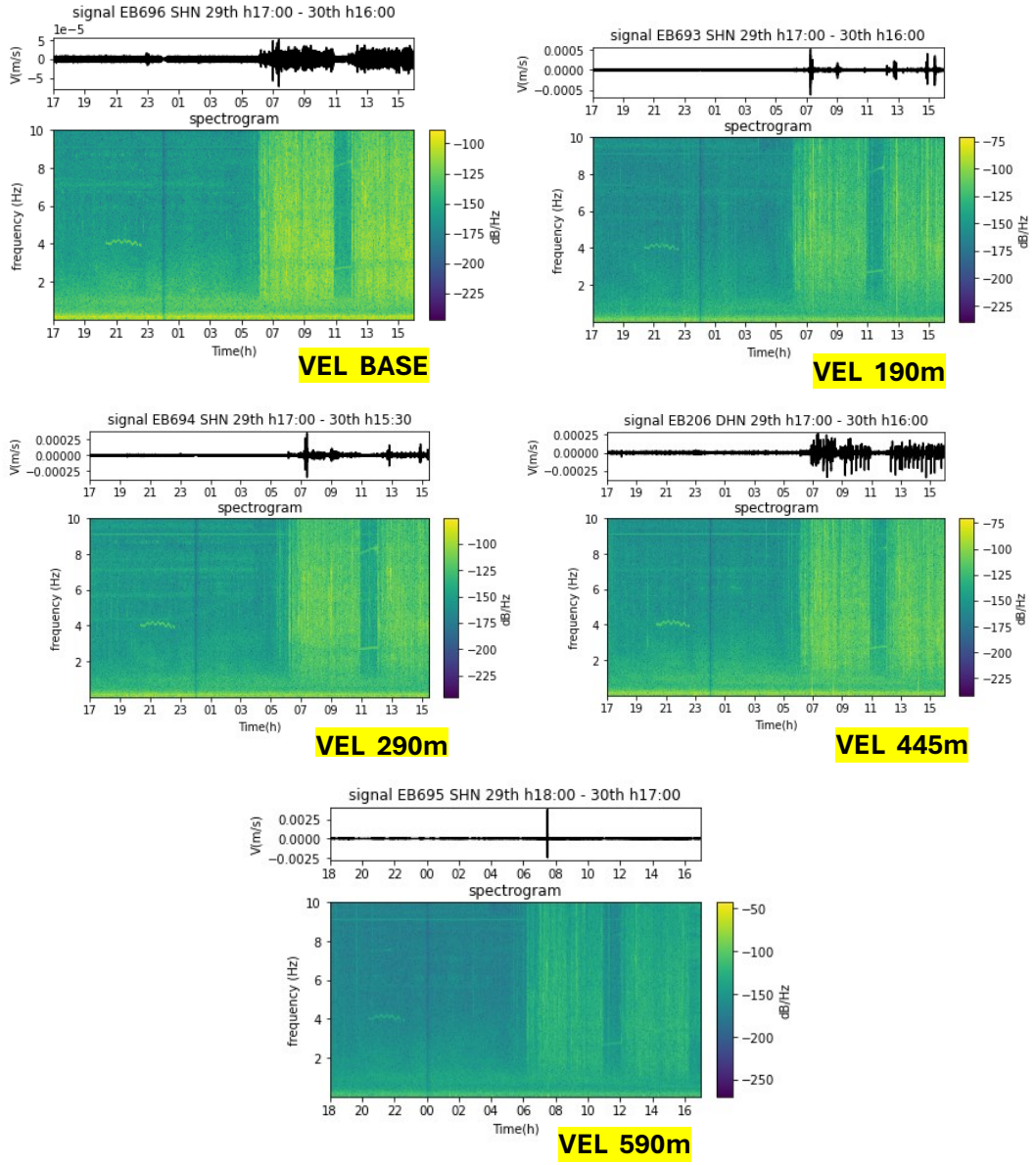

Figure 23: Spectrograms of just one horizontal direction for all the sensors. The graphs of the sensors positioned on the top of the tower are more enlarged.

The larger graphs, representing the sensors located on top of the tower, reveal the existence of two distinct frequency peaks below 2 Hz in the velocimeter, while only one such band is barely visible in the accelerometer. In contrast, for the other velocimeters, these peaks are not as readily discernible. At low frequencies, a lighter halo may be discernible, but it is not as prominent as the peaks for the velocimeter EB587.

On the other hand, what all sensors have in common is the low signal magnitude during the night and its increase from 6 a.m.UTC onwards with a broadband signal above 1 Hz containing a wide range of frequencies typical of white anthropic noise.

4.1.5 HODOGRAM

The hodograms were calculated for each velocimeter over the course of one minute. For the velocimeter EB587 located on the top of the tower, the hodograms were constructed for the first minute of each hour in the 23-hour recording period. In contrast, for the other sensors, due to the discrepancy in the start and end times of the recorded data, only the first minutes of the hours between midnight and 3 p.m. UTC were subjected to analysis.

Prior to calculating the hodograms, a bandpass filter was applied between 0.3 Hz and 0.45 Hz, which corresponds to the frequency range that includes the highest peak depicted by the previous analyses.

Fig. 24 illustrates the complete set of hodograms for all sensors, presented in both cartesian and polar coordinate formats.

Velocimeter EB587 top of the tower
29th January 2024 16:00 - 30th January 2024 15:01

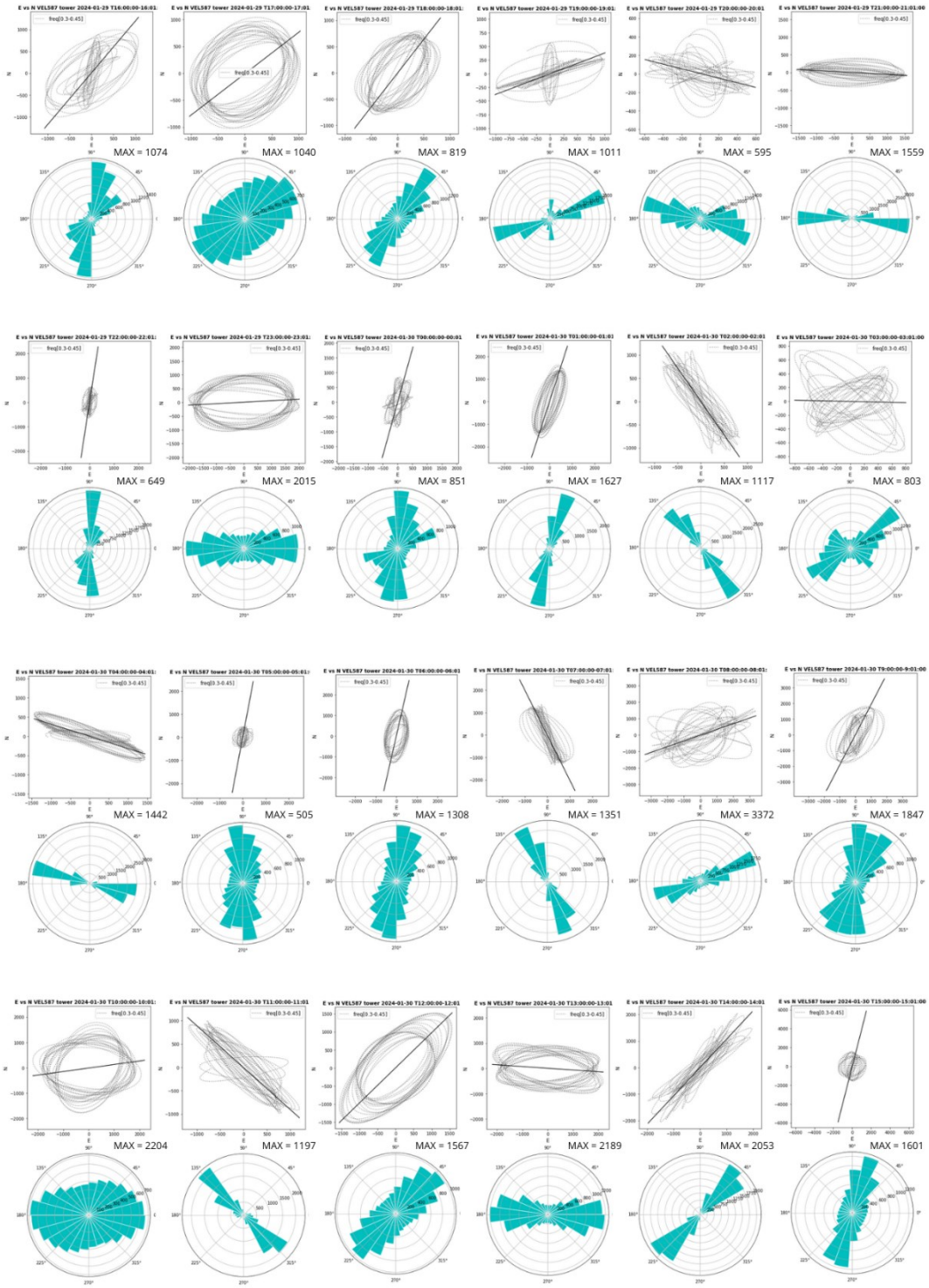

Velocimeter EB696 base
30th January 2024 00:00 - 15:01

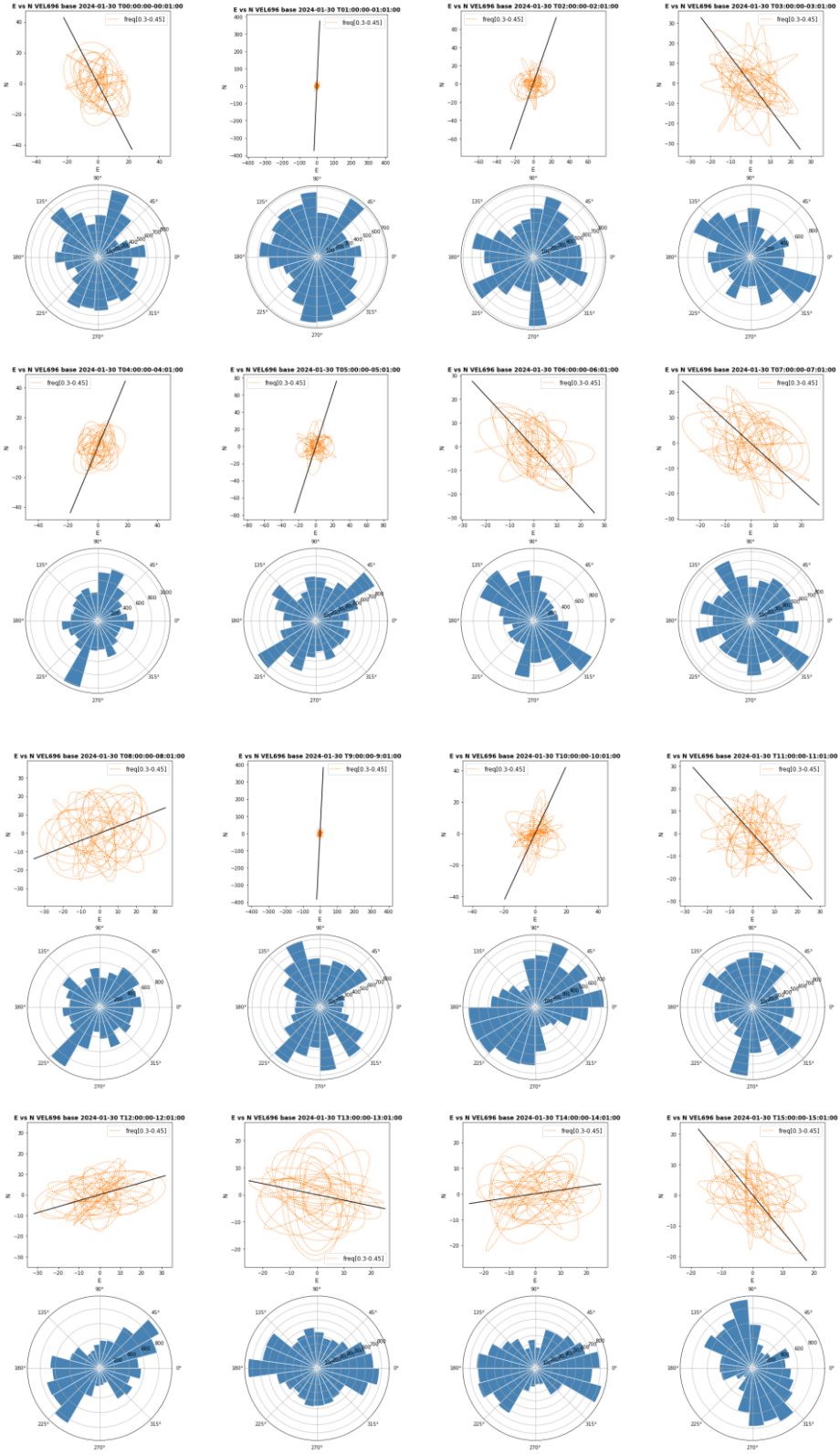

Velocimeter EB693 190m
30th January 2024 00:00 - 15:01

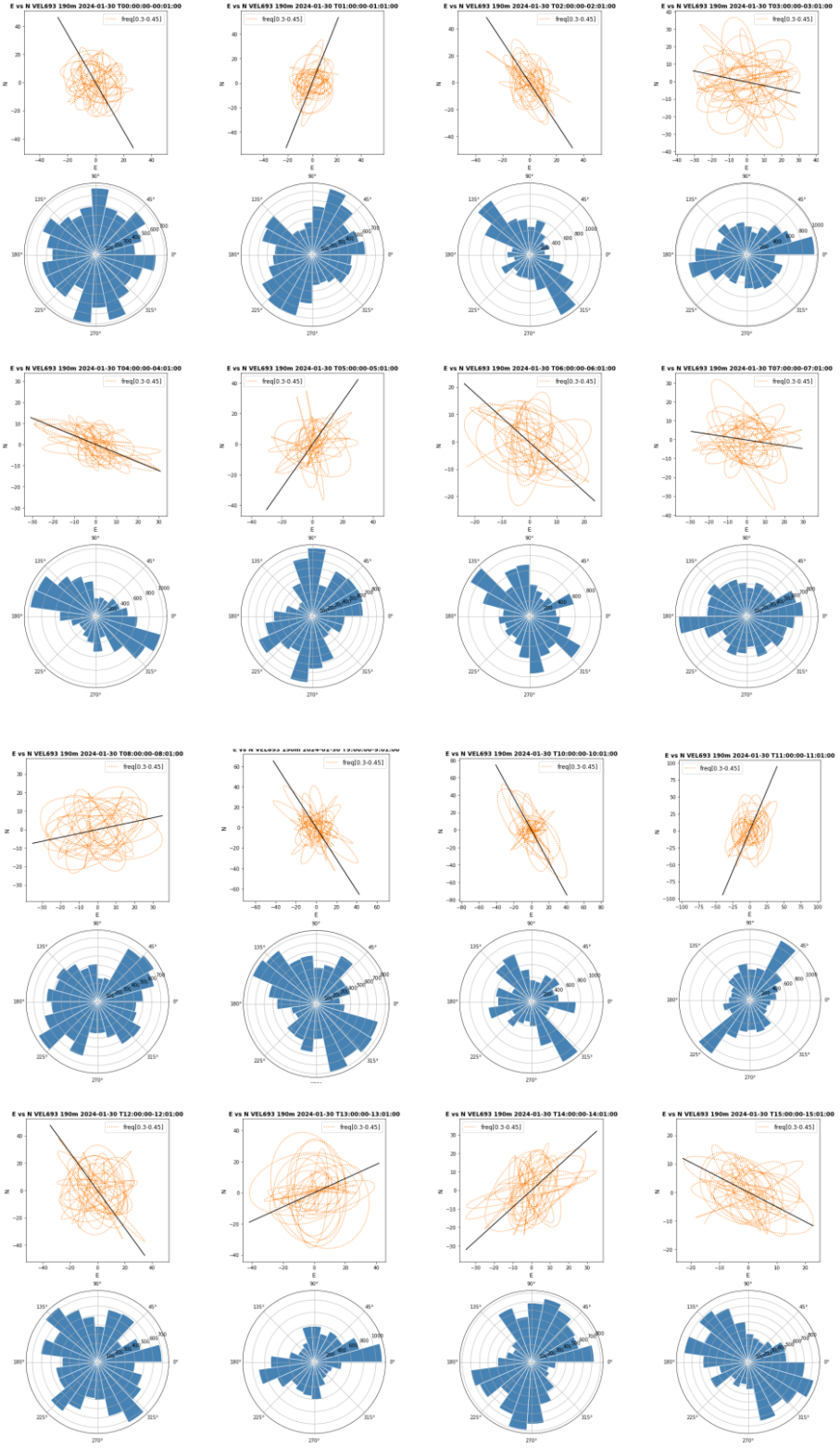

Velocimeter EB694 290m
30th January 2024 00:00 - 15:01

Velocimeter EB206 445m
30th January 2024 00:00 - 15:01

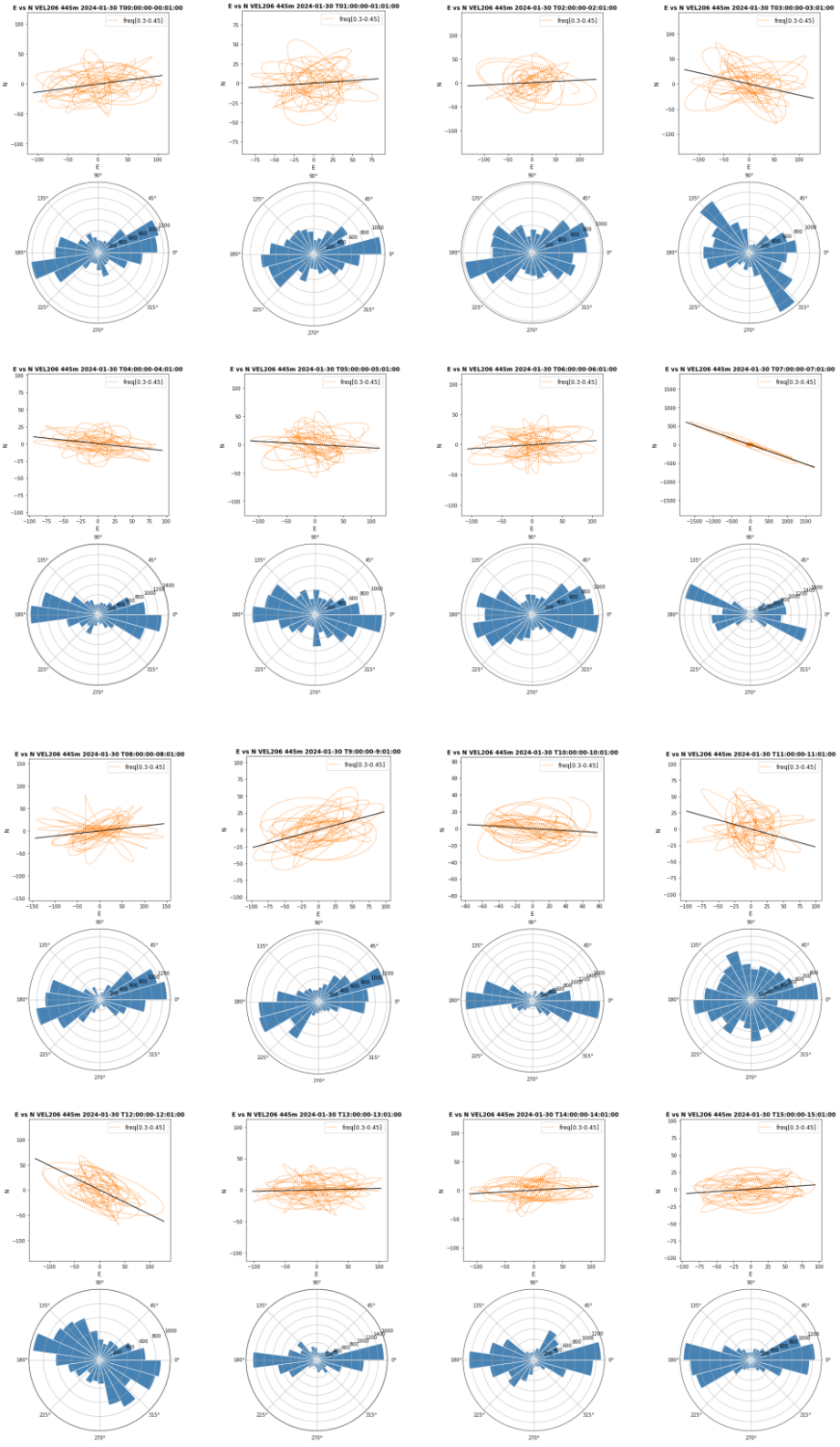

Velocimeter EB695 590m
30th January 2024 00:00 - 15:01

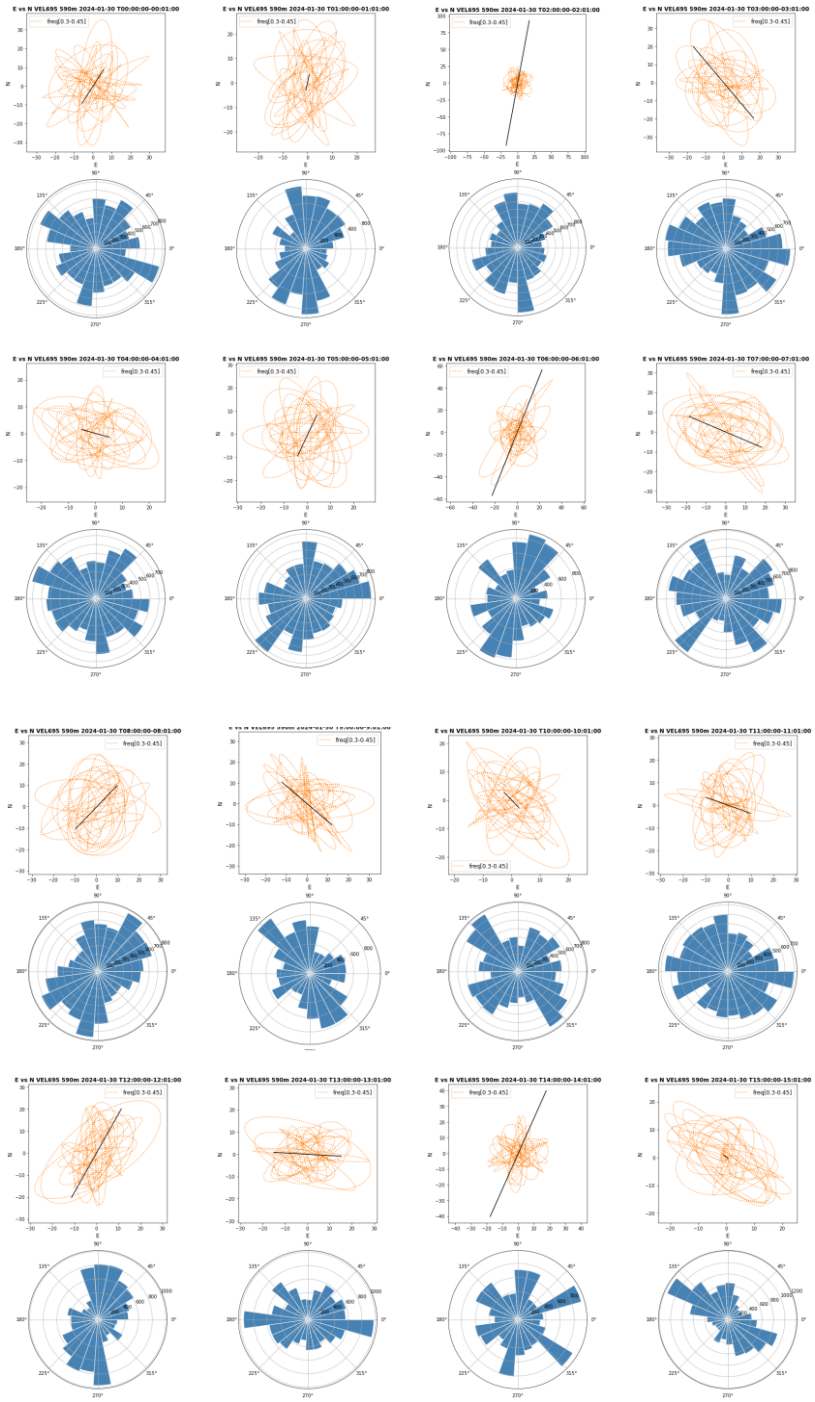

Figure 24: The set of all the hodograms, divided per sensor and calculated for the initial minute of every hour, presented in both Cartesian coordinates (above) and polar coordinate histogram (below). The velocimeter located at the top of the tower is depicted in a different color and the maximum relative displacement values are also shown.

The black line observed in the orange graphs and gray ones, for the velocimeter on the tower, represents the optimal linear fit of the hodograms between the two components. Nevertheless, this method of fitting is not always effective, which is why, in some cases, the hodograms appear to be smaller.

Looking at the polar coordinate histograms, it can be seen that the sensors that are located on the ground and not on the tower don't show prevailing directionality. The only exception is for the EB206 sensor located 445 m away from the tower, which instead shows a strong signal directionality along East-West direction. This sensor is located in the southern area of the Ex-Power Plant, in line with the EB695 sensor about 145m away. Altough they are in the same area, however, the EB695 sensor does not show the same strong directionality. Therefore, the strong directionality observed in the EB206 sensor may possibly be attributed to local ground conditions.

The velocimeter EB587 located on the top of the tower also shows a strong directionality but not in a constant direction during all the hours. The prevailing directions appear to be east-west and northeast-southwest, although there are also some hodograms indicating the presence of prevailing north-south and northwest-southeast directions.

In light of the elevated height of the chimney it may be also important to assess the influence of wind conditions and its potential impact on the directionality of the signal and its maximum value. *Fig. 25* illustrates the wind data recorded over the two-day period of seismic monitoring, obtained from a weather station situated across the channel on the neighbouring island to the south-west of the Porto Tolle chimney.

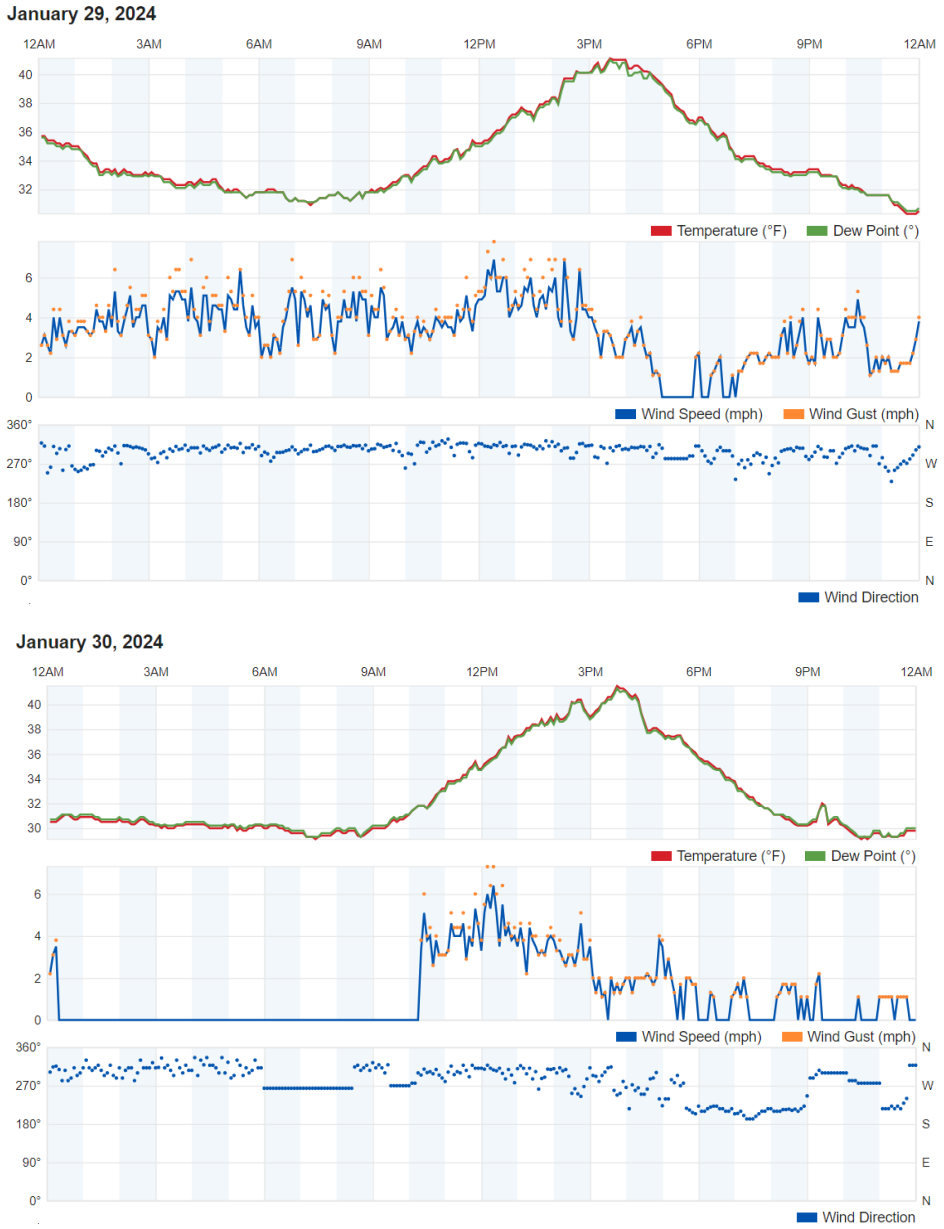

Figure 25: Wind data collected by a weather station in the vicinity of the chimney of Porto Tolle reported in local time (UTC+1).

The data on wind direction indicate that between the afternoon of the 29th of January and the afternoon of the 30th of January, the wind blew steadily in a north-westerly direction. This prevailing direction of movement is observable in some hodograms, like those at 8 p.m. of the 29th of January and 2 a.m., 4 a.m., 7 a.m. and 11 a.m. of the 30th of January UTC. Additionally, while it may

not be a predominant direction, in certain grey hodograms, the movement of particles in that direction can still be seen, such as in those at 3 a.m. and 1 p.m. UTC.

Hodograms are reported in UTC Time while wind data are displayed in CET. In order to compare them, it is necessary to transform UTC Time to CET by adding one hour. In any case, even when converted in local time -CET- , the occurrence of this directionality in some hodograms is not necessarily attributable to the wind, given that these hodograms have been calculated mostly in nocturnal hours, when wind speed is low or minimal according to the graph. An exception is the 11 a.m. UTC hodogram, which actually shows a northwest-southeast orientation when the wind speed is high. However, it is not clear from the graph whether the flat line during the night actually represents zero wind speed or whether it is lack of data.

An examination of the root-mean-square -RMS- values calculated for the displacement data recorded by the velocimeter at the top of the tower and reported in CET local time *(Fig.26)* reveals that the peaks in the RMS graph are not directly attributable to the maximum wind speed. Maximum wind speed values are recorded between 12 noon and 1 p.m. while RMS peaks calculated in both horizontal directions are highest between 9 a.m. and 11 a.m. CET and around 3 p.m. and 4 p.m. CET. The maximum values recorded and reported in the hodograms of the velocimeter EB587 at the top of the tower are also in agreement with a high value around 9 o'clock and 11 o’clock CET, while no significant increase is observed around 12 o'clock CET.

It should be noted that these maximum values are not the direct displacement values but they are the raw values recorded in digital counts. The relationship between digital counts and displacement is linear i.e., just a scaling factor so, in any case the maximum values reported in the hodograms are directly related to displacement.

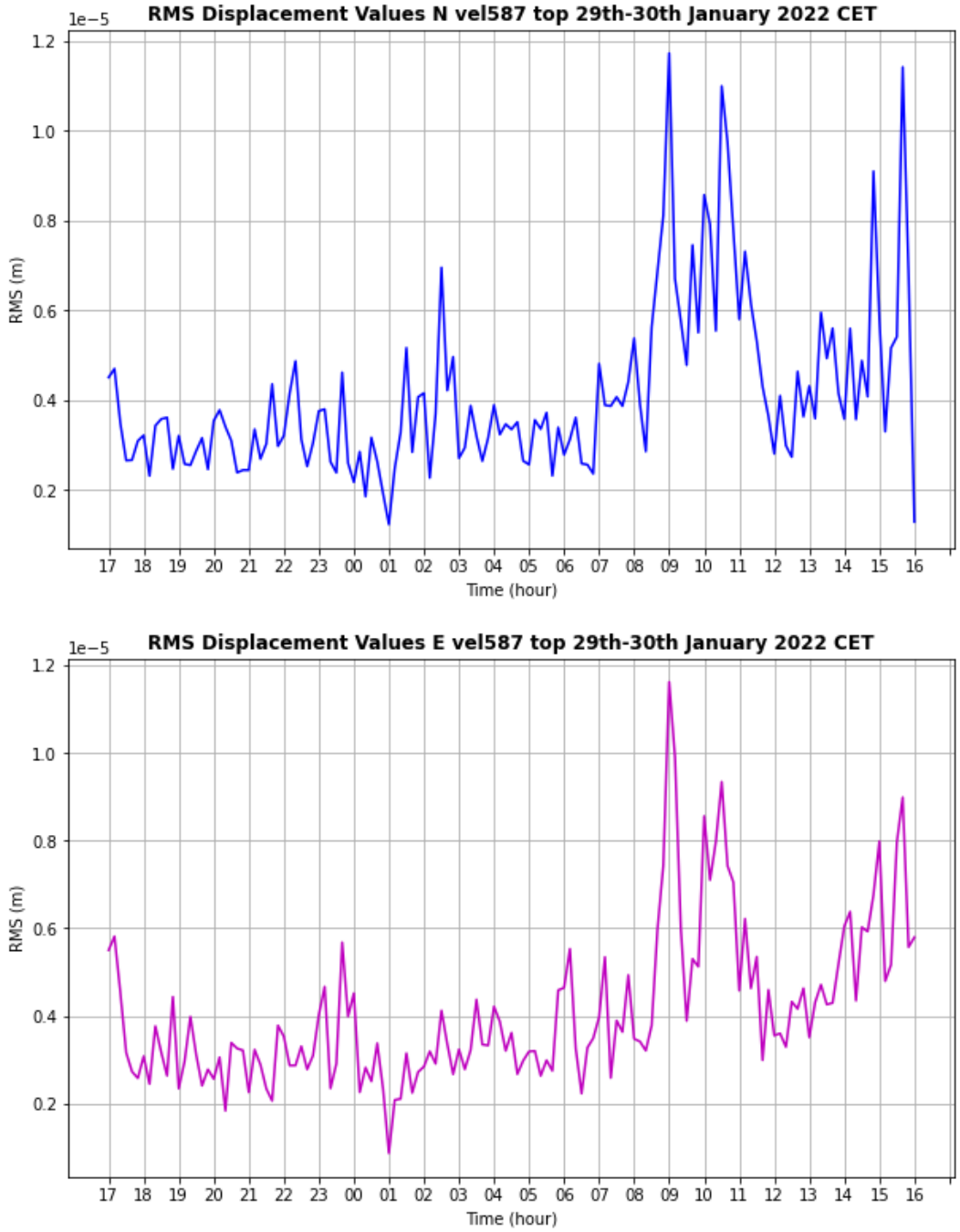

Figure 26: RMS values calculated for displacement for the two horizontal directions registered by the velocimeter on the top of the tower reported in CET local time.

4.1.6 MODAL ANALYSIS

To perform the modal analysis, only data collected by the accelerometer located at the top of the tower were utilized. Data from a single sensor located on a single floor enable the evaluation only of the first vibration mode of the structure. The first or fundamental mode represents the lowest natural frequency of the structure. In this mode, the structure tends to deform in a uniform manner, with maximum displacement occurring in a specific direction.

A simple model comprising a single vertical line and a node at the top, in which the sensor is positioned, was constructed in order to reconstruct the chimney.

A total of six 20-minute intervals were extracted from the 23 hours of recorded data. These intervals were subjected to a modal analysis and the corresponding frequencies were obtained from the SVD line and validated through the mode animation and MAC values. The frequencies were then tabulated and a mean value was calculated for all the frequencies identified. In *Fig. 27* are reported the SVD line, the MAC values and the modal shape of just one interval. As it is not possible to display the animations in a static image, the black arrows indicate the direction of the deformation of the tower observed from an aerial perspective.

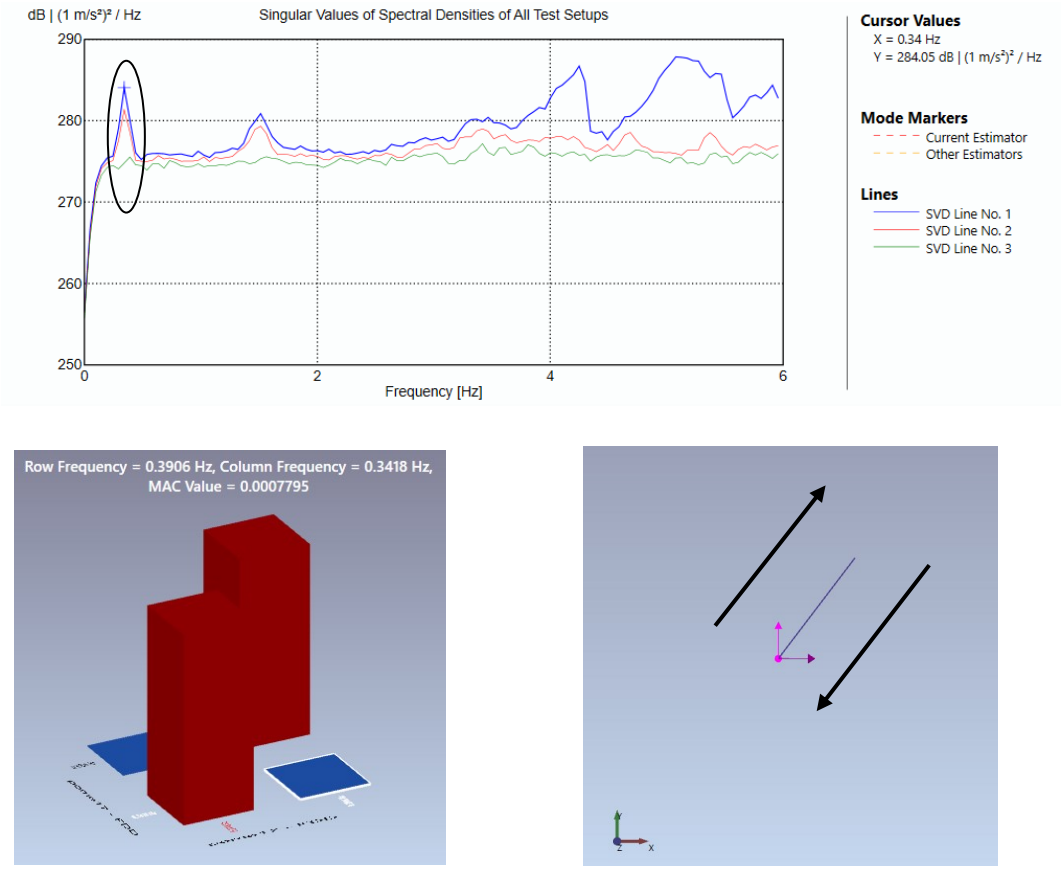

Figure 27: Graphical representation of the singular values in function of frequency -SVD lines- (top), MAC value of two selected frequency within the first peak (bottom left) and screenshot of the animation of the first modal form (bottom right). Results obtained from only one 20-minute interval.

The results obtained from all the intervals were highly consistent, with the SVD lines consistently depicting two prominent picks below 2 Hz. However, it was only possible to validate the first modal form, which corresponded to the first peak. The final mean value of the frequencies found with regard to the first mode is 0.37 Hz.

An examination of the MAC values reveals the presence of a very low MAC value between two frequencies very close to each other and that are both located within the same peak, specifically 0.39 Hz and 0.34 Hz. This is demonstrated by the nearly flat blue column in *Fig.27*, while the red ones in

the diagonal represent a comparison of the mode with itself and are always equal to one. An examination of the mode animation at the two frequencies reveals that both frequencies represent the first modal shape of vibration, but the deformation occurs in opposite directions, along the NE-SW direction as shown in *Fig.27* and in the perpendicular NW-SE direction.

When two distinct modes have the same or very close frequencies and vibrations in opposite or perpendicular directions, they are referred to as coupled modes. This interaction of modes can occur as a result of the geometry and distribution of masses, as observed in symmetrical structures.

In the modal analysis for the Porto Tolle chimney, the presence of coupled modes in the first modal form has been identified in several time intervals. In this case, the structure has two preferential directions of vibrations, along the two perpendicular axes, which can oscillate simultaneously but with different levels of amplitude or frequency and that can interact with each other.

The mean frequency value corresponding to the first modes is 0.37 Hz; however, the values of the decoupled modes are 0.35Hz in one direction and 0.38Hz along the perpendicular direction.

4.2 ANGERA BELL TOWER

Data collected for two and a half months from the sensors in the Angera bell tower are available for analysis. However, it is time consuming to carry out so many analyses on so many data. I have therefore chosen to focus the analyses mainly on just two days: July 27th and August 27th 2022. In the context of RMS and modal analysis, additional days were analysed.

4.2.1 RMS

Similarly to the RMS analysis conducted for Porto Tolle, an RMS analysis was carried out for the Angera site using a single sensor: the velocimeter located on the upper floor. A 10-minute time window was employed for both days, the 27th of July and the 27th of August 2022 *(Fig.28)*. In addition, an RMS analysis of a seven-day period from Monday the 25th of July to Sunday the 31st of July 2022 was performed *(Fig.29)*.

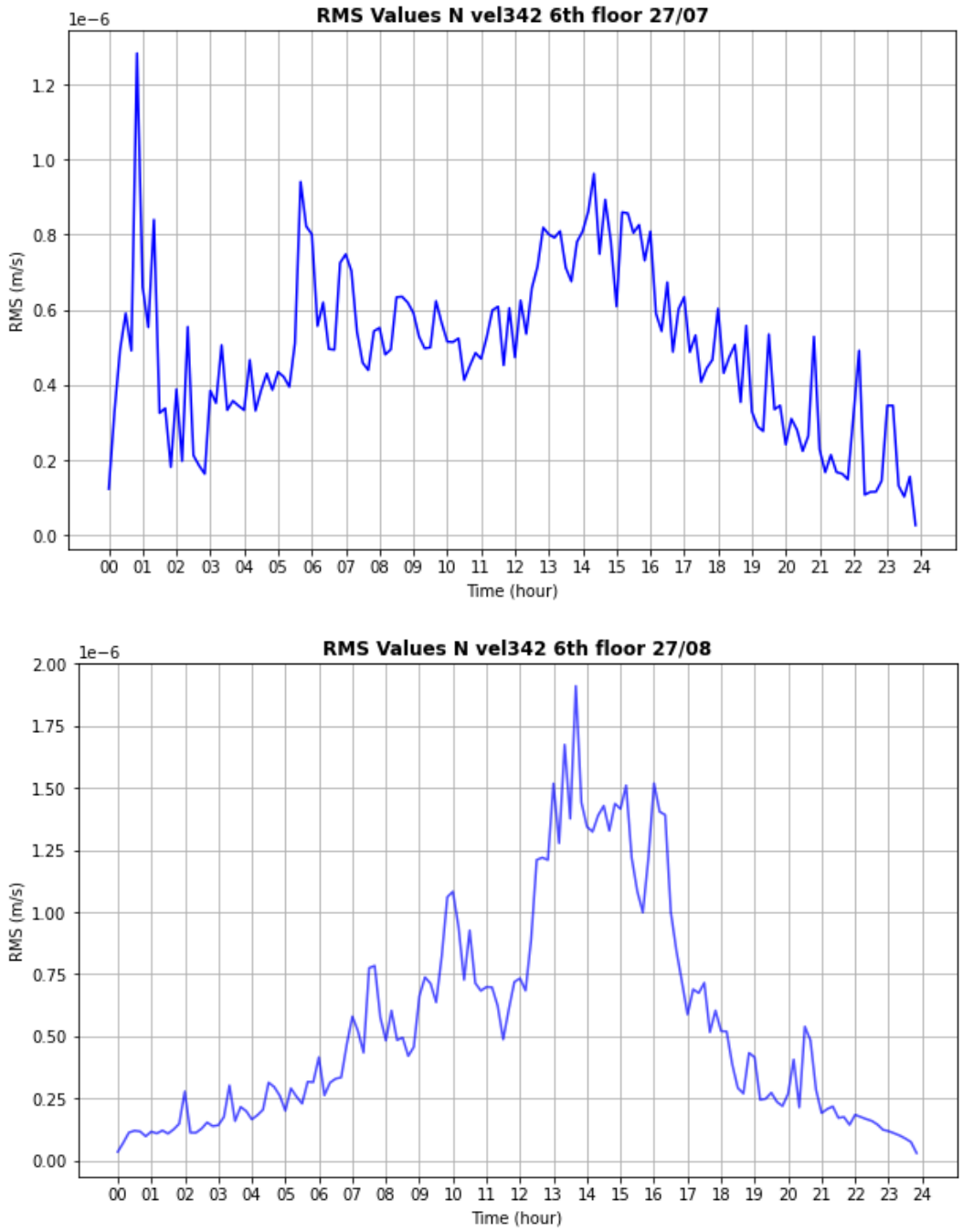

Figure 28: RMS values of the velocimeter on the 6th floor calculated over a time window of 10 minutes for the 27th July (above) and the 27th August (below) for one horizontal direction.

From *Fig. 28* the signal strength is distributed relatively uniformly throughout the day, with maximum RMS values occurring in the center and gradually decreasing during the night and evening. Beyond a peak between 1 a.m. and 2

a.m. UTC on the 27th of July and a through or drop around lunchtime local time -UTC+2- for August 27th, the two graphs exhibit a consistent trend. July 27th corresponds to a Wednesday while August 27th is a Saturday.

Regarding the analysis of the week between July 25th and 31st, as illustrated in *Fig. 29*, pronounced peaks are observed in the latter half of the day on Monday and Tuesday. Even between the night of Thursday and Friday the values remain elevated. While on Wednesday, Saturday and Sunday evenings high peaks are not visible. On the contrary to what might be expected in a tourist area during the summer, the signal over the weekend does not demonstrate higher values than on weekdays.

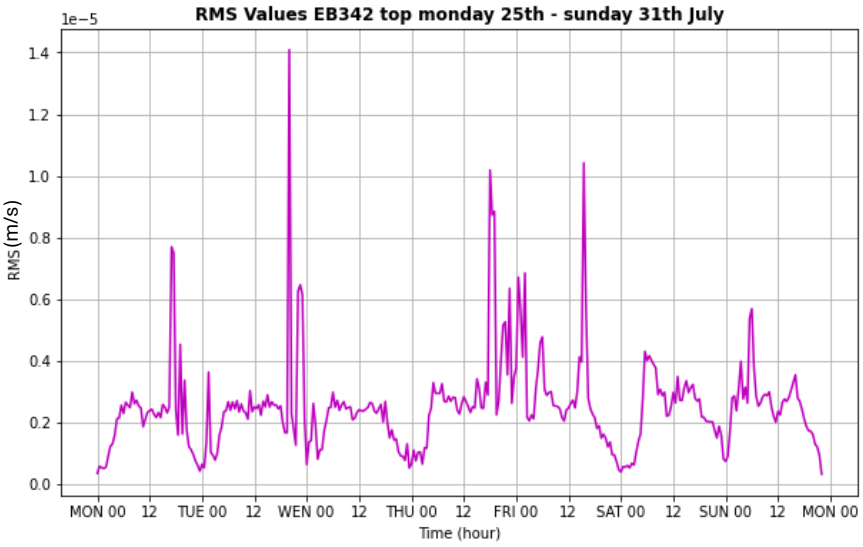

Figure 29: RMS values of the velocimeter on the 6th floor calculated over a time window of 10 minutes for a week from the 25th to the 31st of July 2022.

4.2.2 HVSR

The HVSR was calculated for all sensors, including the accelerometer, for both days. However, as explained in chapter 1.3.2, the velocimeter situated on the fourth floor at some point has been removed, and from the 8th August onwards, no data is available. Consequently, for all the following analysis regarding August 27th that sensor was not taken into account. The window length used is 240s. *Fig.30* and *Fig.31* show the HVSRs obtained for all sensors for July 27th and August 27th, respectively.

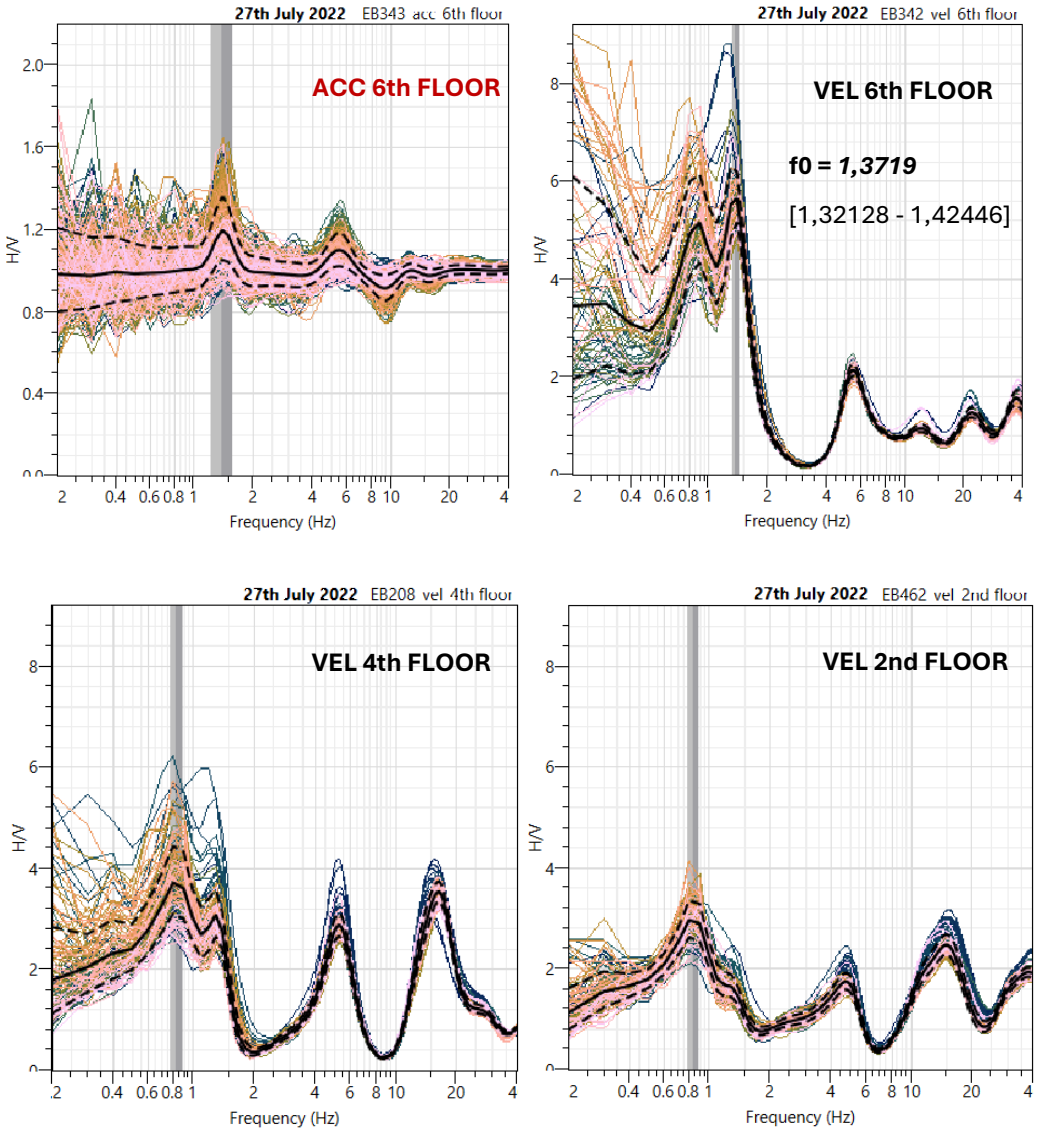

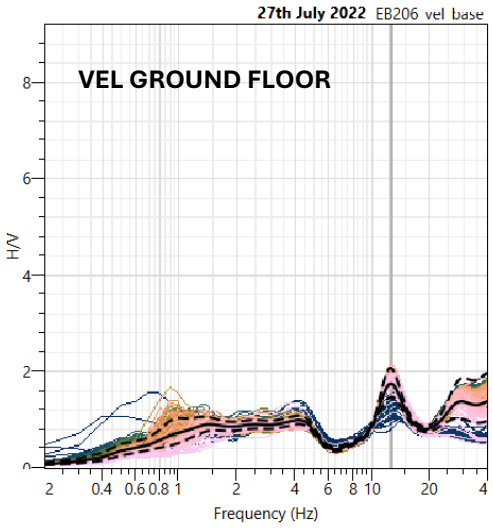

Figure 30: HVSR of all the sensors for July 27th from the highest to the lowest.In the velocimeter on the 6th floor is reported the identified value of the highets peak and its uncertainty frequency range.

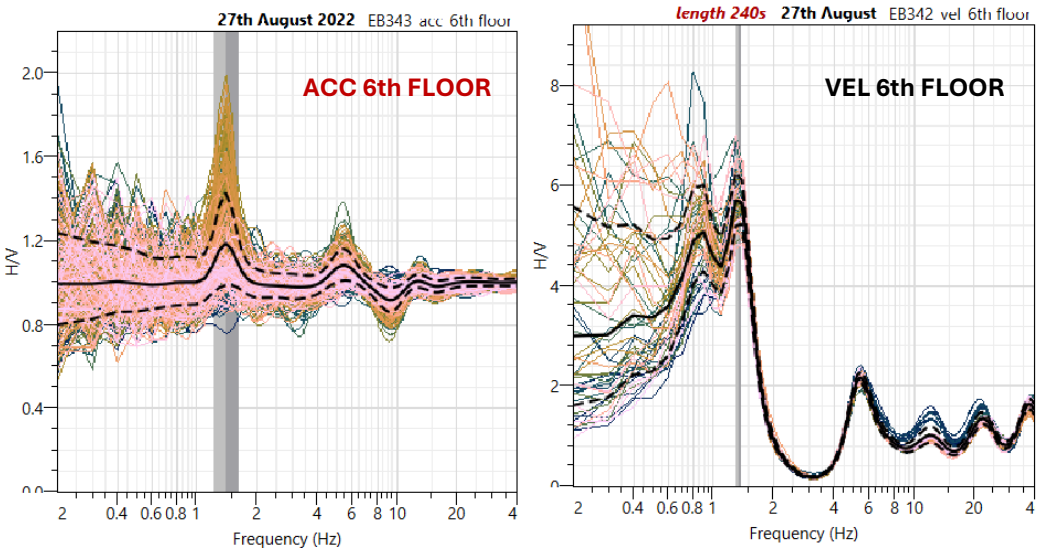

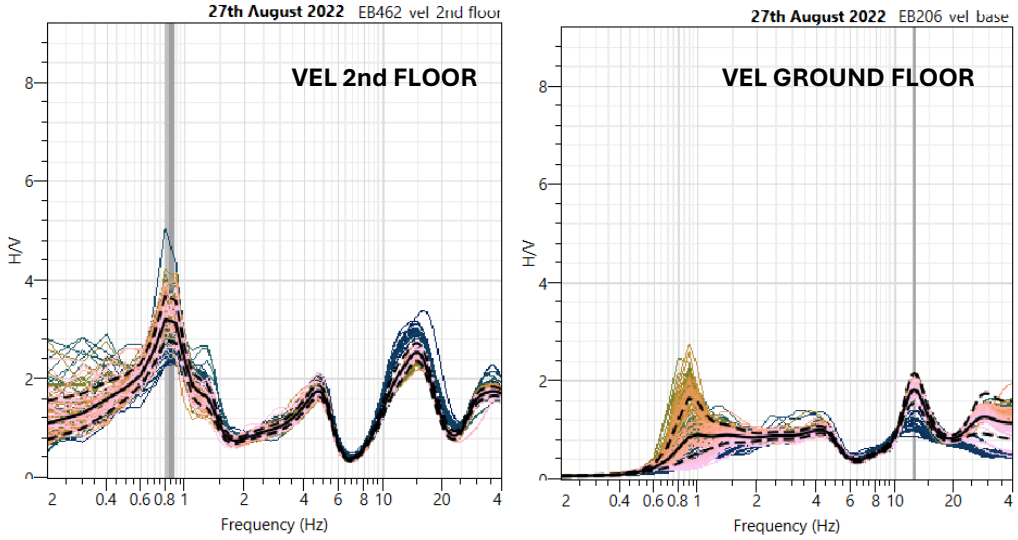

Figure 31: HVSR of all the sensors for August 27th from the highest to the lowest.

The data indicate that the results are consistent for both days.

The velocimeter on the highest level -6th floor- displays two distinct peaks below 2 Hz, the most prominent of which is situated between the values of 1.32 Hz and 1.42 Hz. Additionally, a series of less pronounced peaks can be observed from 4 Hz and above. The higher frequency peaks around 5 Hz and 15 Hz, are most prominent in the velocimeter on the fourth floor, visible only on July 27th, and remain visible in the one on the second floor as well. In contrast, the lower-frequency peaks flatten out as the height of the sensors decreases, until the velocimeter at the base, which shows an almost flat spectrum.

The peak between 1.32 Hz and 1.42 Hz appears to be more pronounced in the velocimeter on the sixth floor than the nearby peak around 0.8 Hz. However, in the other sensors, the situation is reversed, with the peak around 0.8 Hz being more prominent.

With regard to the accelerometer, the peak at approximately 1.37 Hz and the higher-frequency peak at around 5 Hz are also discernible in this case. In contrast, the lower frequency peak at 0.8 Hz is not visible at all.

Similar to Porto Tolle, if the HVSR is calculated for the accelerometer in a time interval when the recorded signal strength is low, for example during the night of August 27th, no frequency peaks are clearly discernible *(Fig.32)*.

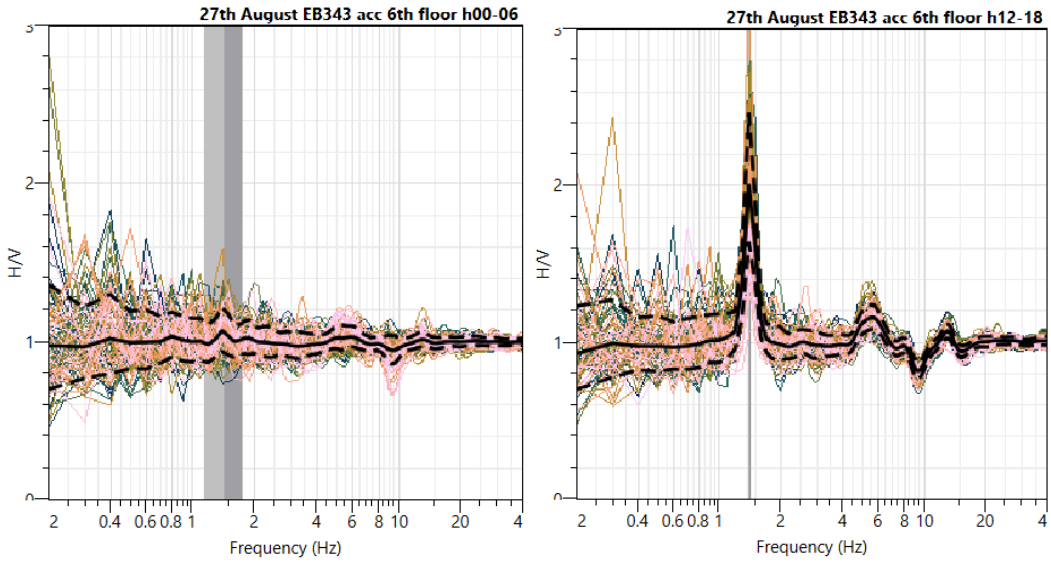

Figure 32: HVSR of the accelerometer on the 6th floor for August 27th, two different time intervals (night and day).

4.2.3 PSD

The PSDs were calculated for a 3-hour interval during the less noisy night hours for both days and for all sensors. The value of NFFT used is 2^15.

Fig.33 and Fig.34 shows the results obtained for only one horizontal direction compared for all velocimeter sensors for both days. The decision to report only one horizontal direction for the velocimeters is only to visually facilitate the comparison between PSDs for the different floors. In any case, the results for the two directions are almost identical, as can be seen from the results of the two horizontal directions for the accelerometer.

The most evident peak is that of the sensor on the sixth floor, occurring at approximately 1.5 Hz on both days. Also, the sensor on the second floor

detects a similar peak, although with a minor amplitude. In contrast, the peak observed in the sensor on the fourth floor, which is present only on the 27th of July, appears to be shifted towards lower frequencies and does not align with the peak frequency observed in the other sensors. Two additional peaks are observed in the sensor on the sixth floor, at approximately 5 and 10 Hz, which are not markedly distinct from one another. These peaks are more pronounced in the sensor on the second floor and still exhibit a shift to lower frequencies on the fourth floor. For the sensor on the ground floor, the peaks become less defined, flatten out and are barely discernible.

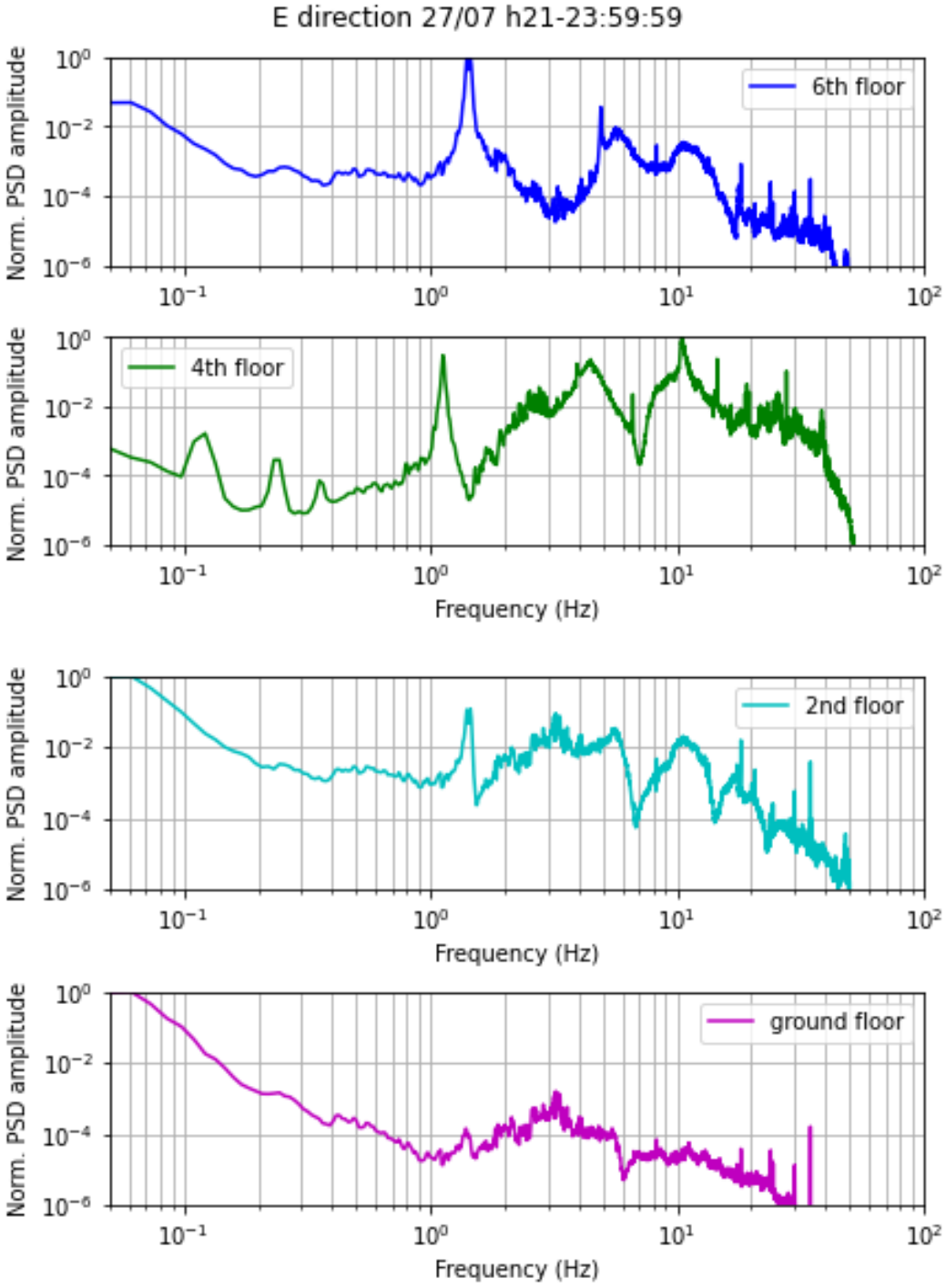

Figure 33: Normalized, to the maximum of the 6th floor, PSD comparison of only one horizontal direction for all the velocimeters for the 27th of July .

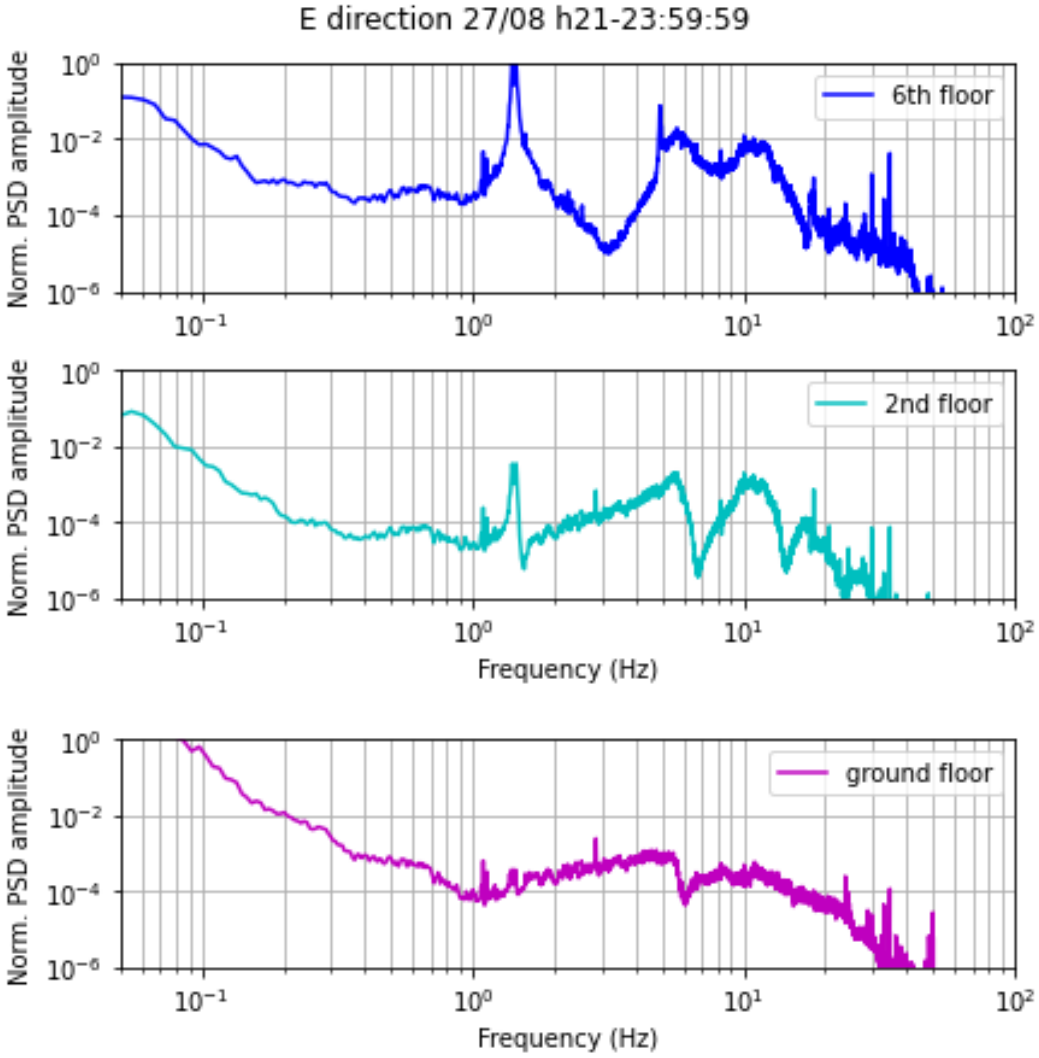

Figure 34: Normalized, to the maximum of the 6th floor, PSD comparison of only one horizontal direction for all the velocimeters for the 27th of August.

Fig.35 illustrates the results obtained for the accelerometer in the two horizontal directions over the same time interval, for both days. The peak at 1.5 Hz is evident in both directions and on both days, while no other peaks at higher frequencies are discernible. The visible peak has low amplitude values compared to the velocimeter. Analyzing the PSD obtained for a time range where the signal strength is higher according to the RMS between 1 p.m. and 5 p.m. UTC *(Fig.36),* the peak shows higher amplitude and some broader peaks at higher frequencies also appear.

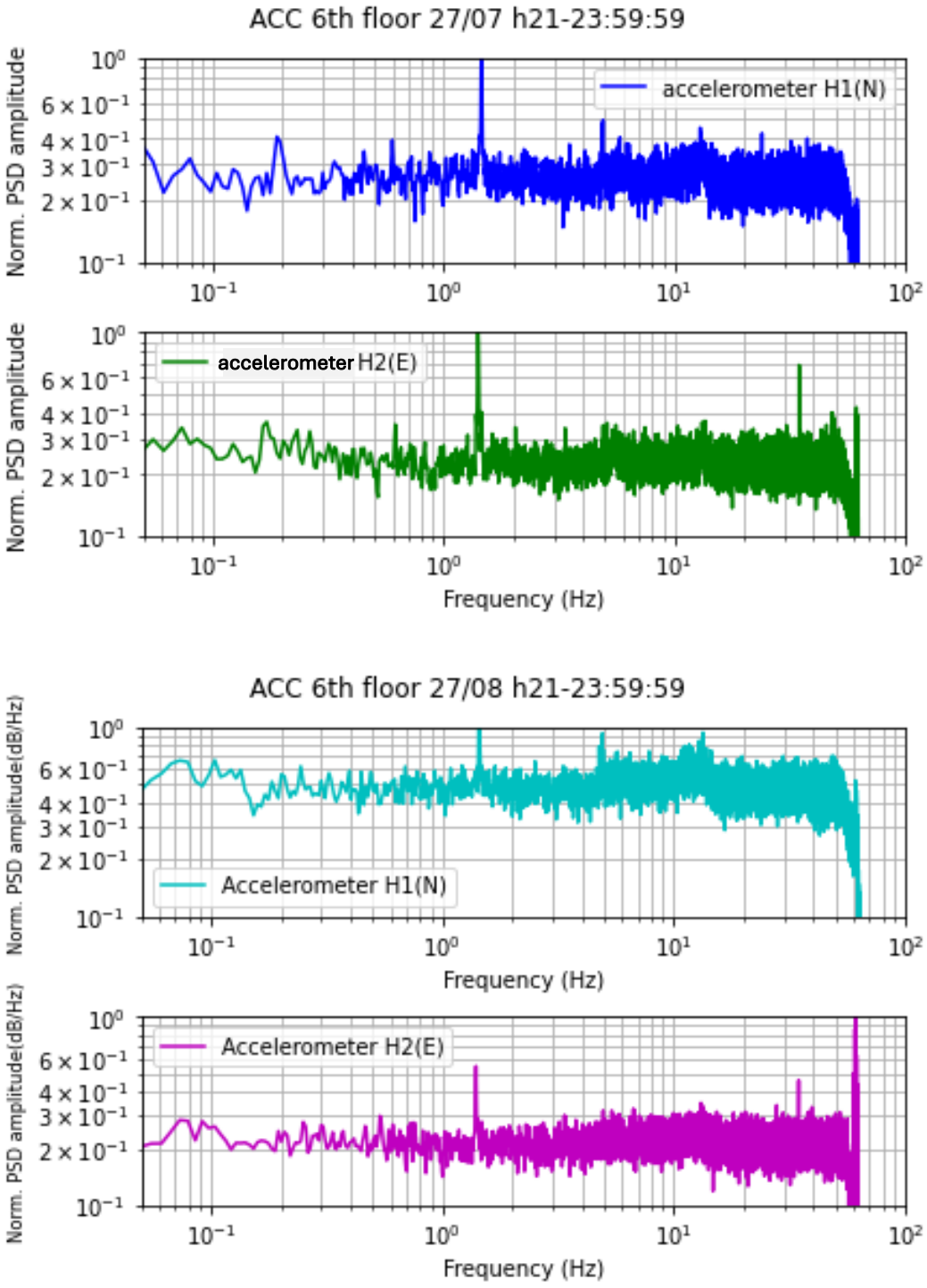

Figure 35: Normalized PSD comparison of the horizontal directions for the accelerometer on the 6th floor for the 27th of July (above) and for the 27th of August (below).

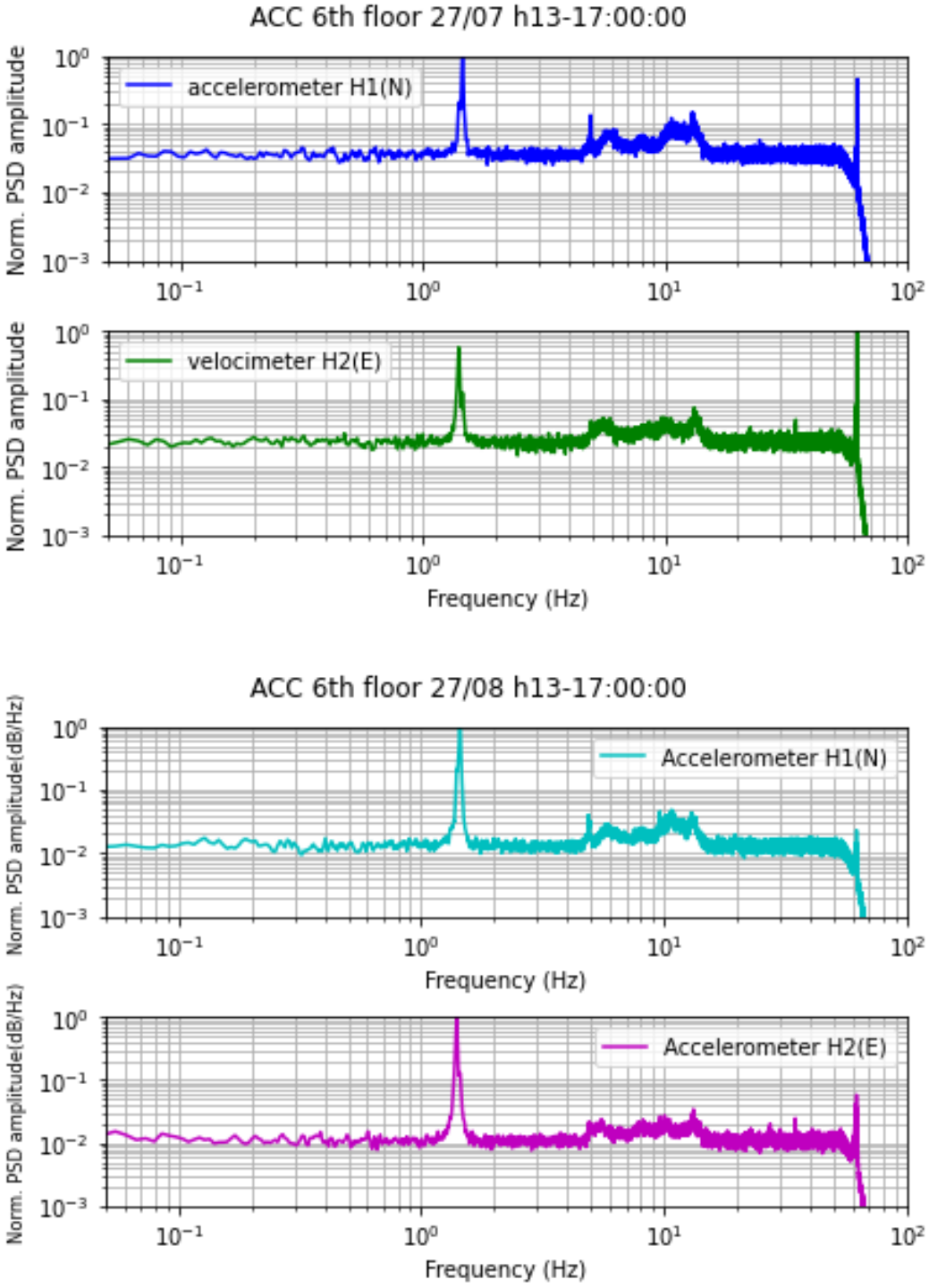

Figure 36: Normalized PSD comparison of the horizontal directions for the accelerometer on the 6th floor for the 27th of July (above) and for the 27th of August (below) for a different time interval between 1 p.m. and 5 p.m. UTC.

4.2.4 SPECTROGRAM

As for Porto Tolle, spectrograms were produced for the full 24-hour periods of July 27th and August 27th for all sensors, and are displayed for just one horizontal component in *Fig.37* and *Fig.38*, respectively.

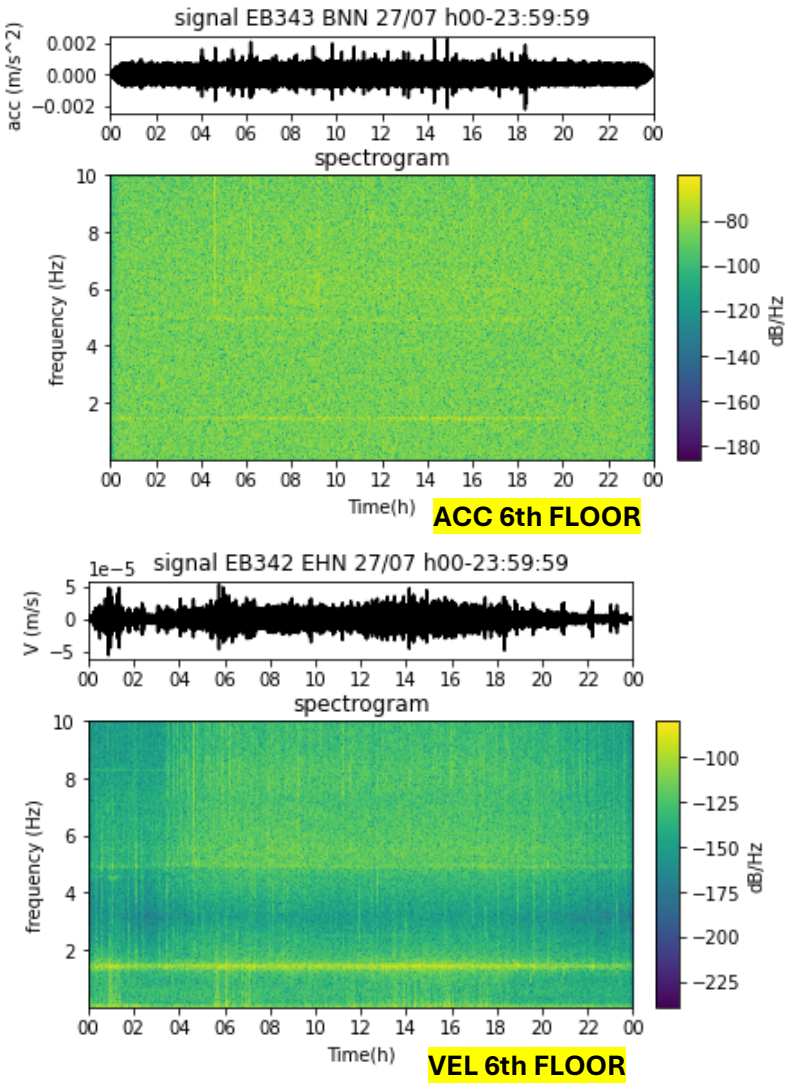

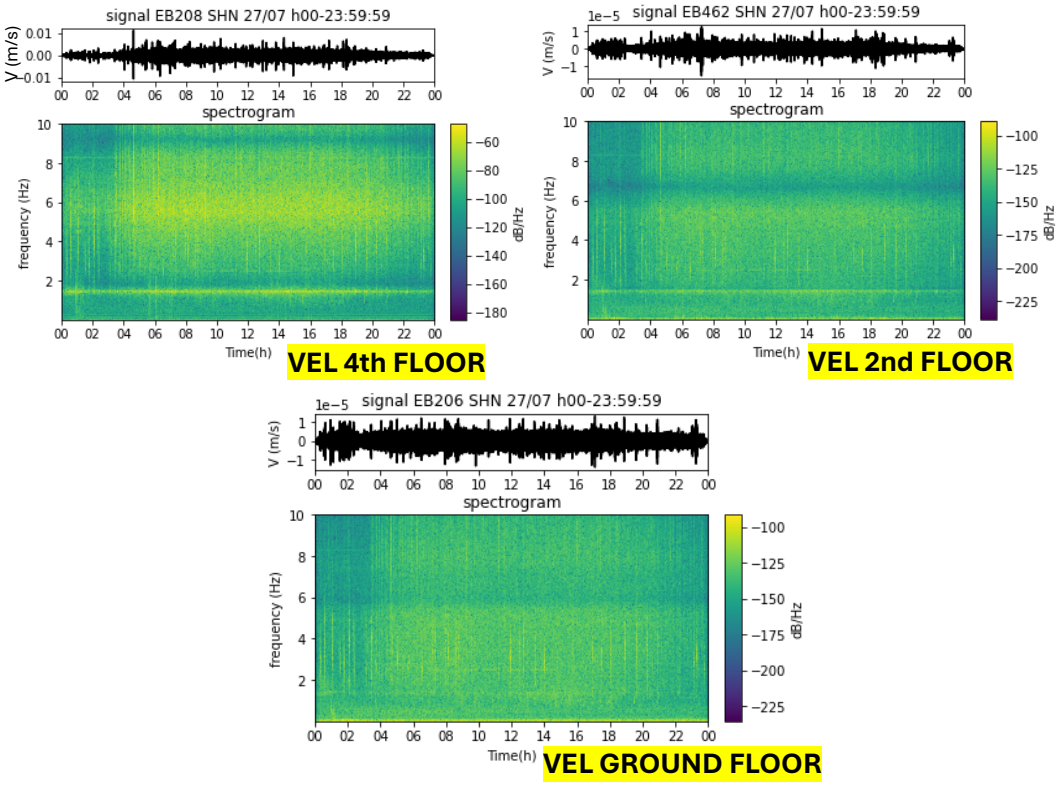

Figure 37: Spectrogram of all the sensors for just one horizontal direction for the 27th of July.

The spectrograms show comparable results for both days. Two distinct frequency peaks are clearly discernible in the velocimeter situated on the upper floor. The first band is visible just below 2 Hz and the second around 5 Hz. The lower frequency peak is also discernible in the sensors on the fourth and second floors, while the peak around 5 Hz is no longer visible. In the velocimeter on the ground floor, both peaks are no longer discernible.

In the accelerometer on the sixth floor the two frequency peaks are visible although much less pronounced than in the velocimeter. In addition, especially on the day of August 27th, the peaks are more highlighted during the central hours of the day.

In comparison to the Porto Tolle spectrograms, these appear to be considerably more disturbed, with vertical lines of high intensity present throughout the day.

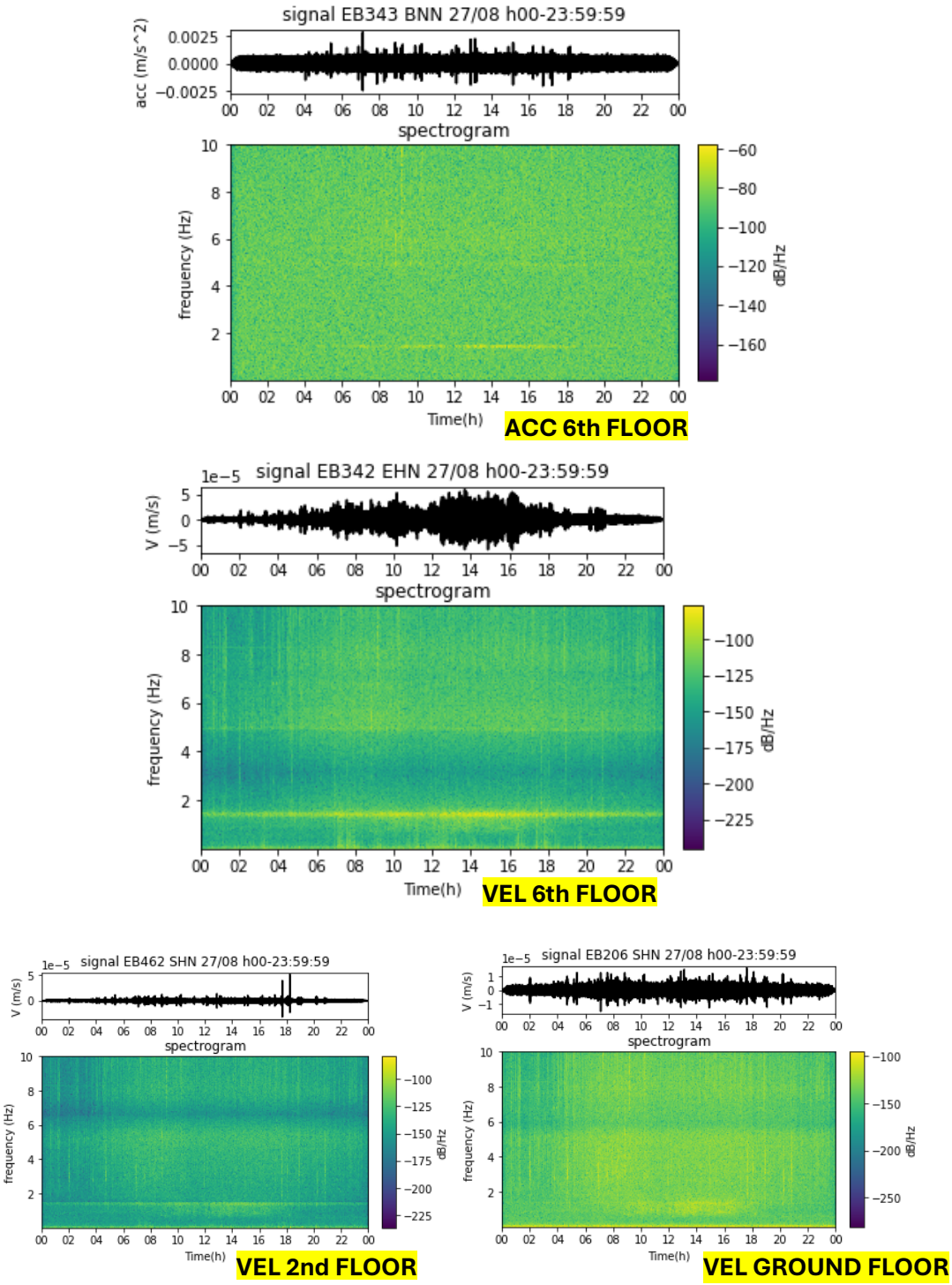

Figure 38: Spectrogram of all the sensors for just one horizontal direction for the 27th of August

Additionally, it is possible to discern the presence of a periodic signal, which is present in all sensors and observed on both days. It appears as vertical halos in the range from 2 Hz to 6 Hz in the spectrograms and is more visible during the night of July 27th *(Fig.39)*. It is a fairly regular and intermittent source of noise, which when activated lasts several tens of seconds and can be attributed to a cooling or ventilation system.

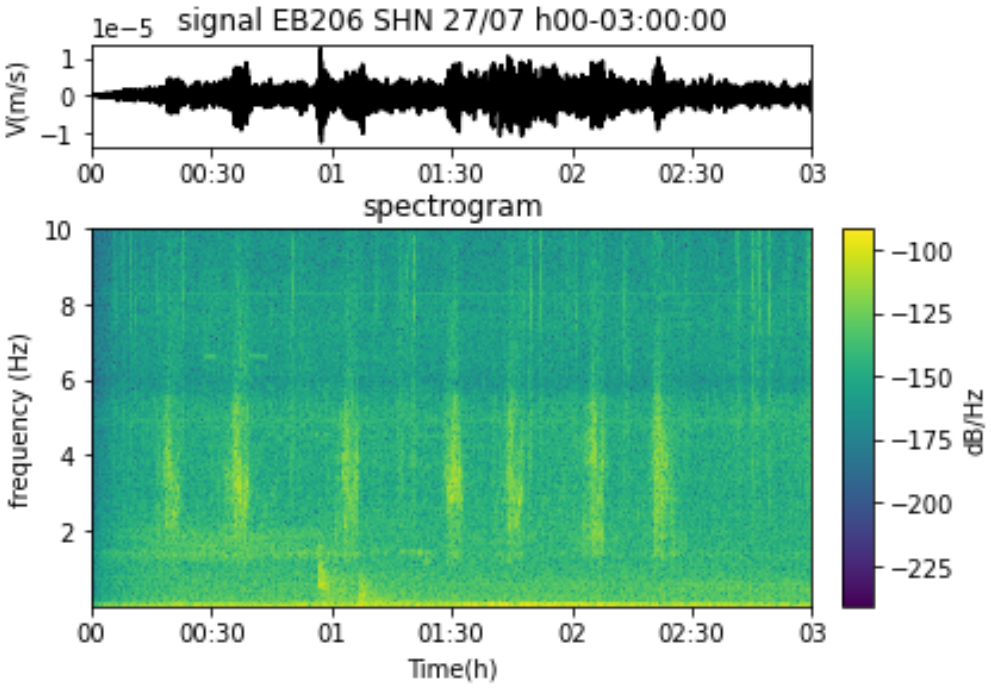

Figure 39: Periodic noise present in spectrograms highlighted for July 27th during night time hours.

4.2.5 HODOGRAMS

The hodograms were calculated for the initial minute of each hour for each sensor, for both July 27th and August 27th. In this instance, a bandpass filter between 1.32 Hz and 1.42 Hz was applied prior to conducting the analyses.

The hodograms are shown in *Fig.40* for July 27th and *Fig.41* for August 27th.

Velocimeter E vs N VEL342 6th floor
27th July 2022 00:00 - 23:01

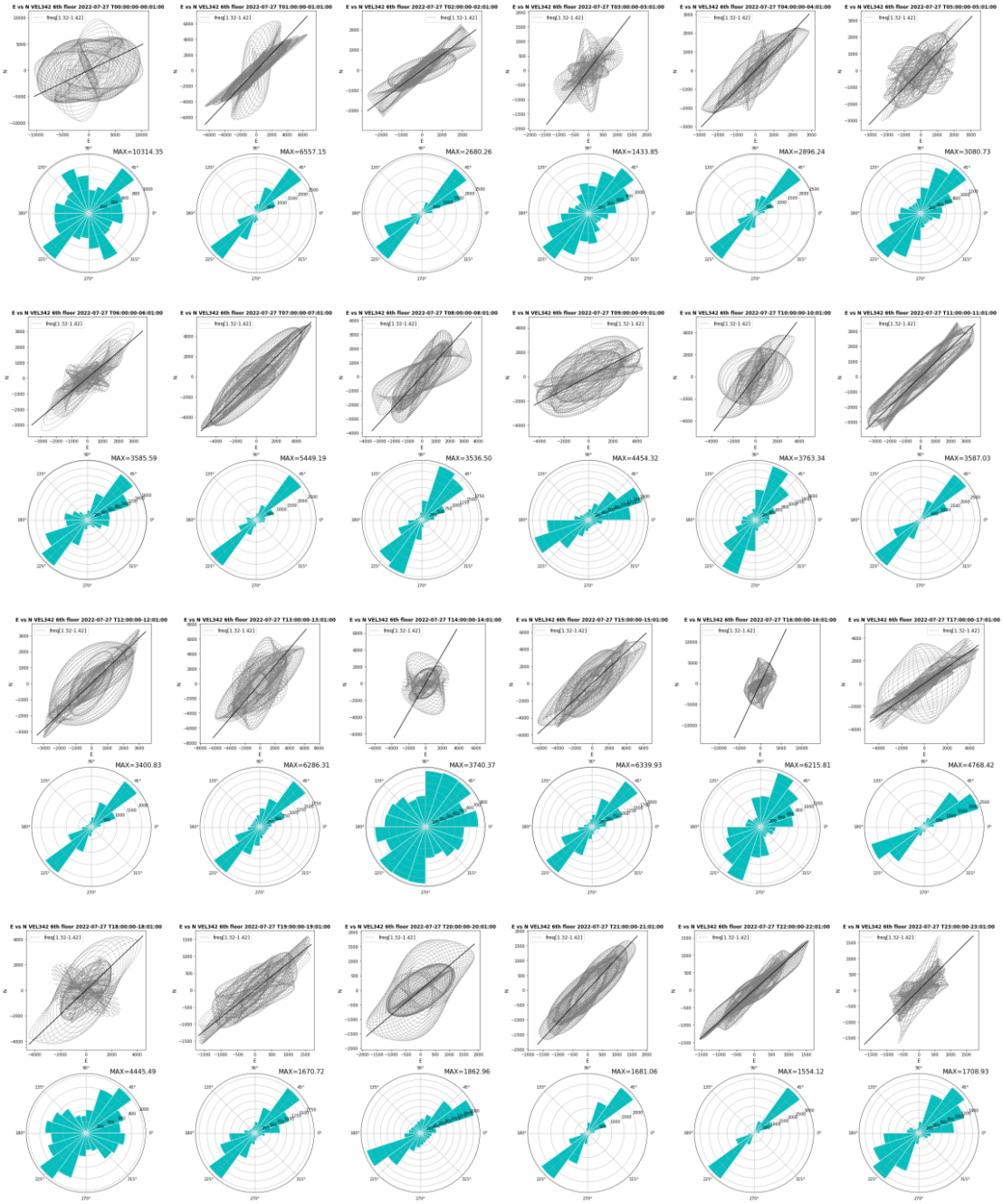

Velocimeter E vs N VEL208 4th floor
27th July 2022 00:00 - 23:01

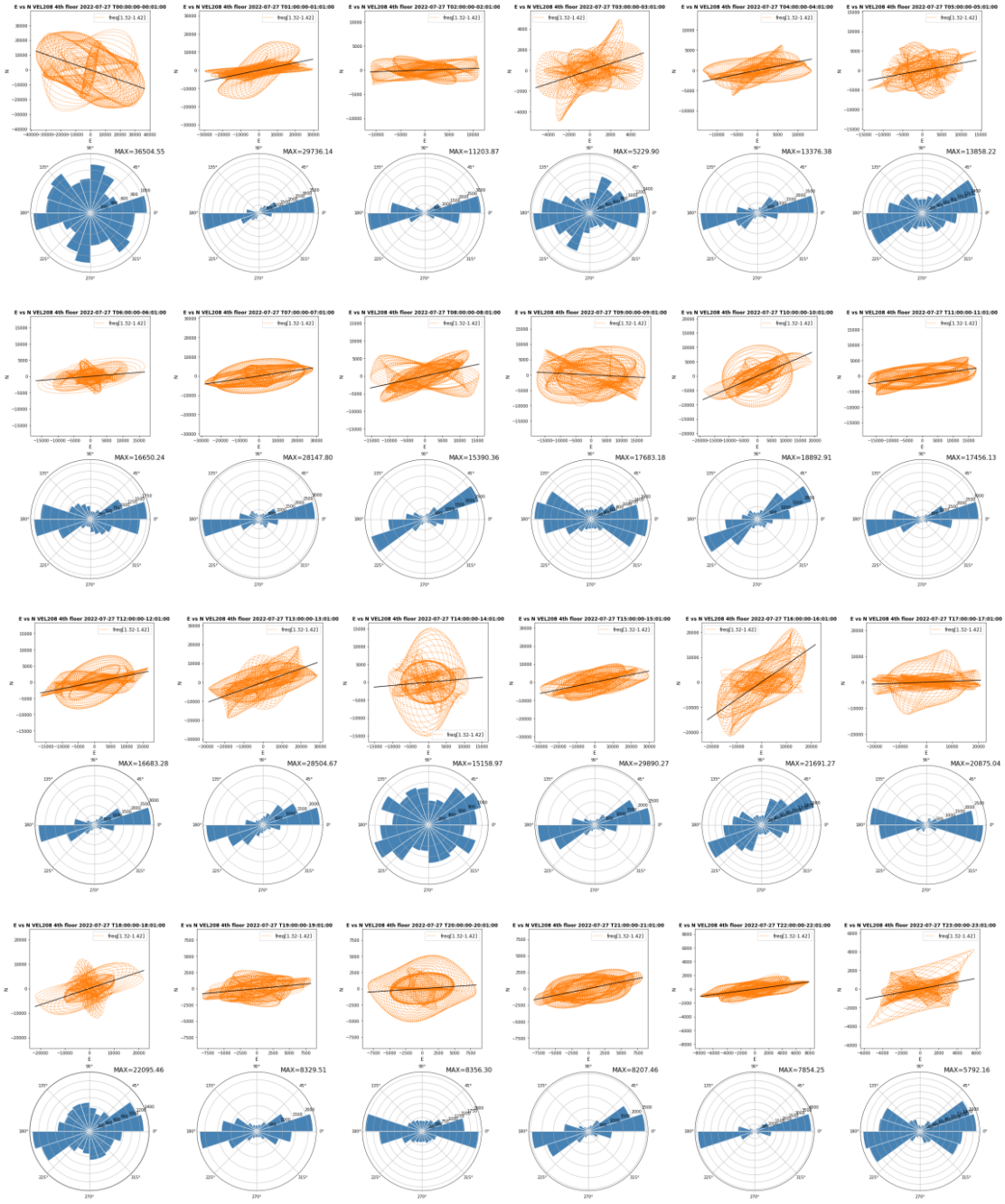

Velocimeter E vs N VEL462 2nd floor
27th July 2022 00:00 - 23:01

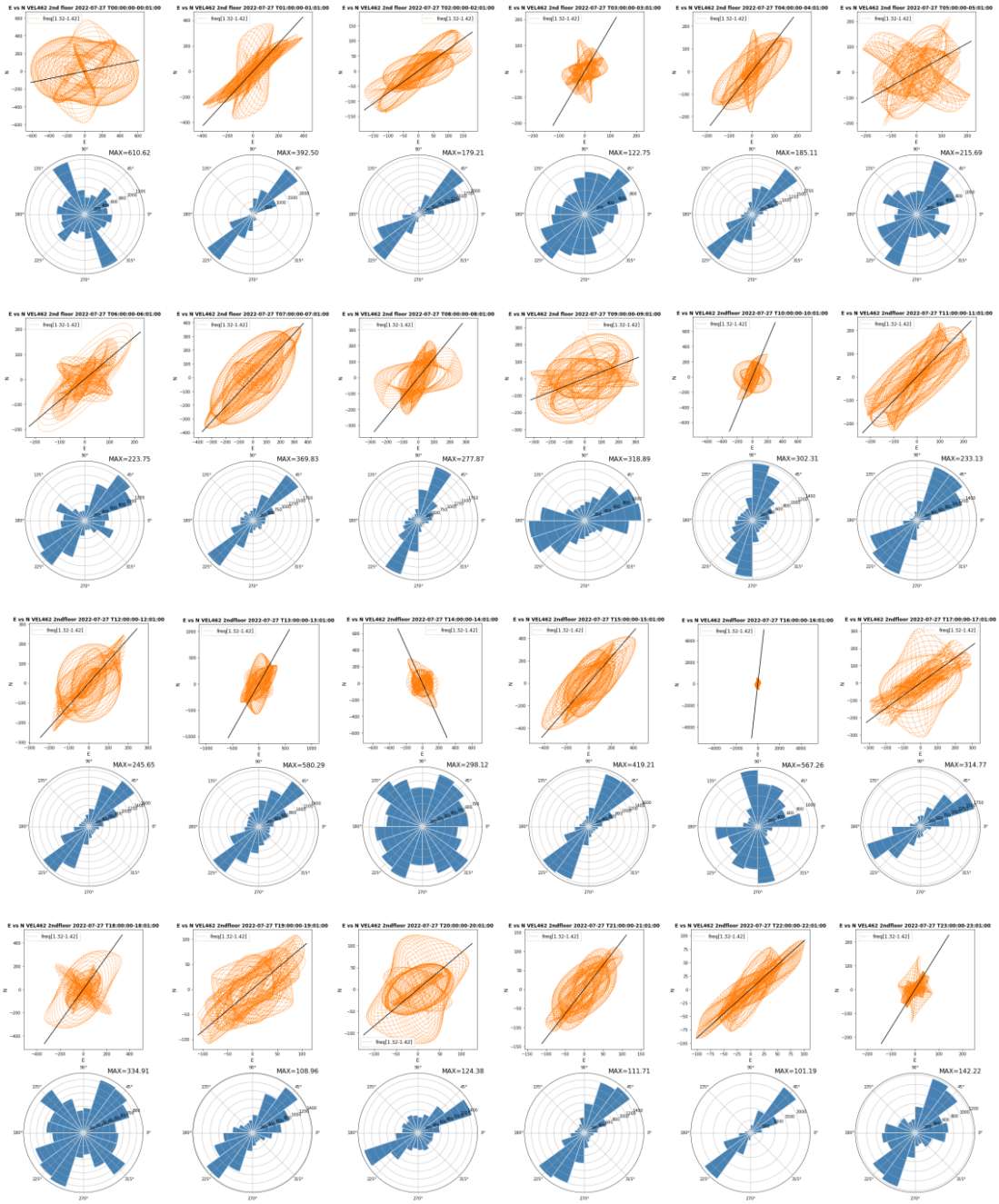

Velocimeter E vs N VEL206 ground floor
27th July 2022 00:00 - 23:01

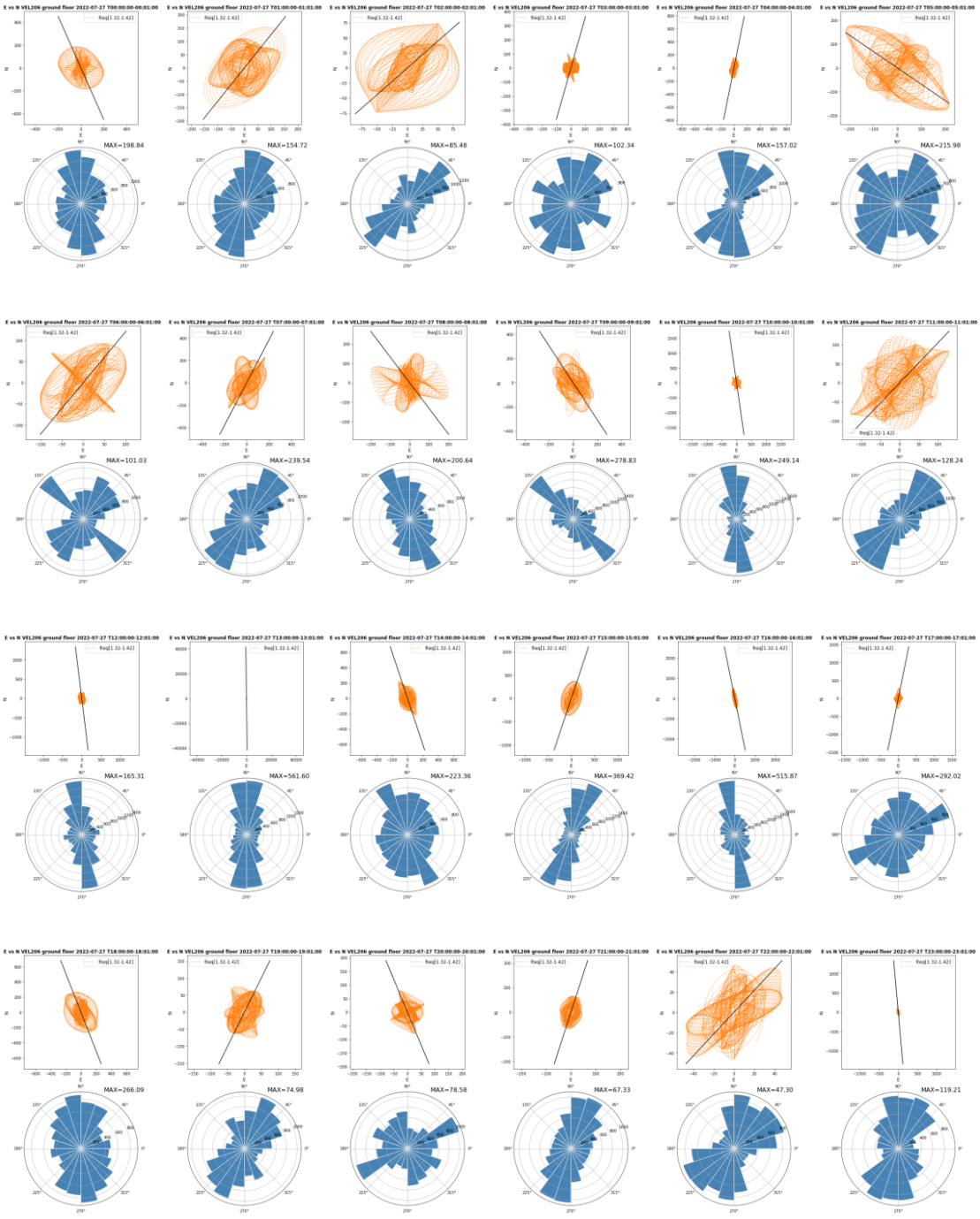

Figure 40: The set of all the hodograms, divided per sensor and calculated for the initial minute of every hour, presented in both Cartesian coordinates (above) and polar coordinate histogram (below) for the 27th of July.

Velocimeter E vs N VEL342 6th floor
27th August 2022 00:00 - 23:01

Velocimeter E vs N VEL462 2nd floor
27th August 2022 00:00 - 23:01

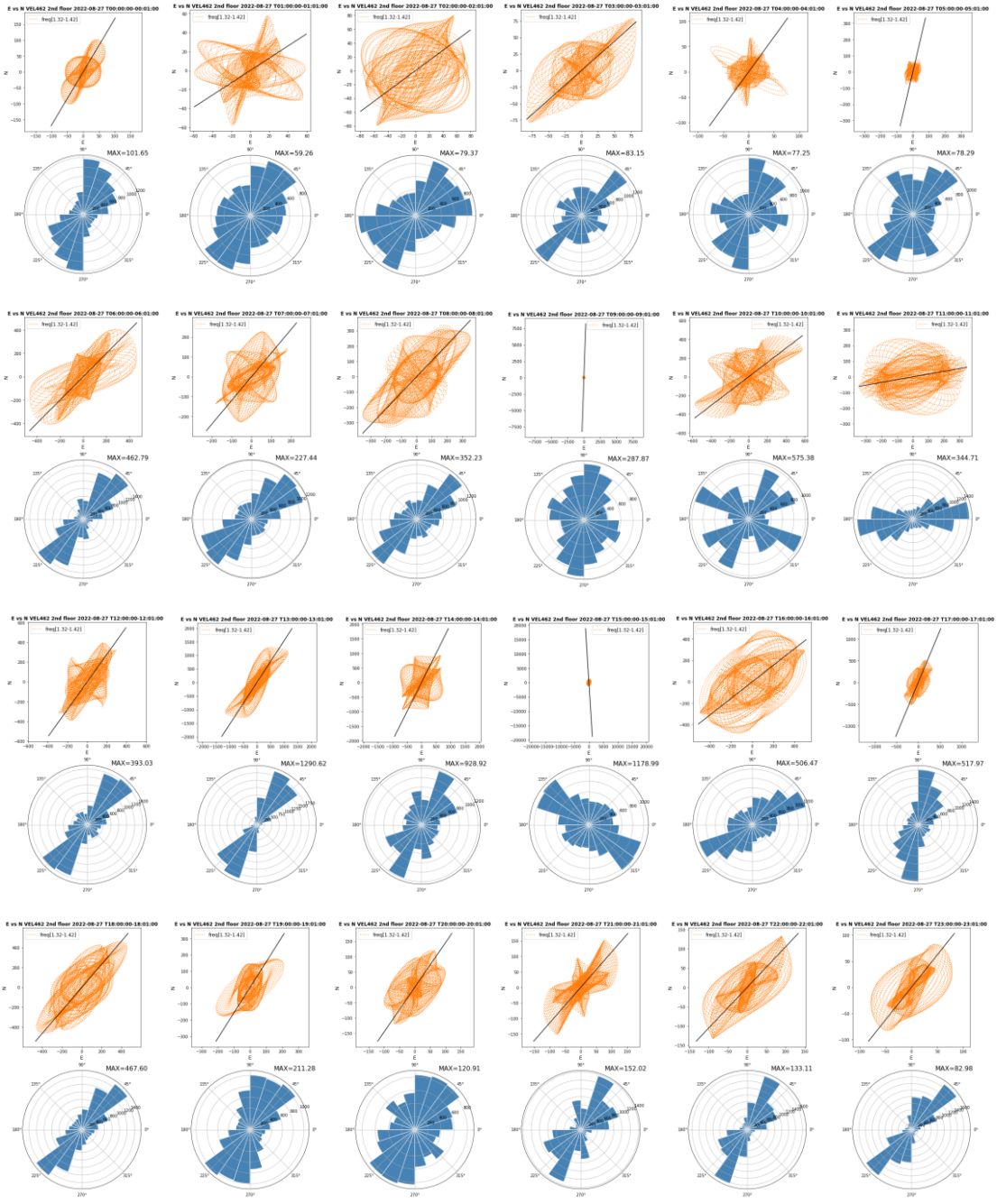

Velocimeter E vs N VEL206 ground floor
27th August 2022 00:00 - 23:01

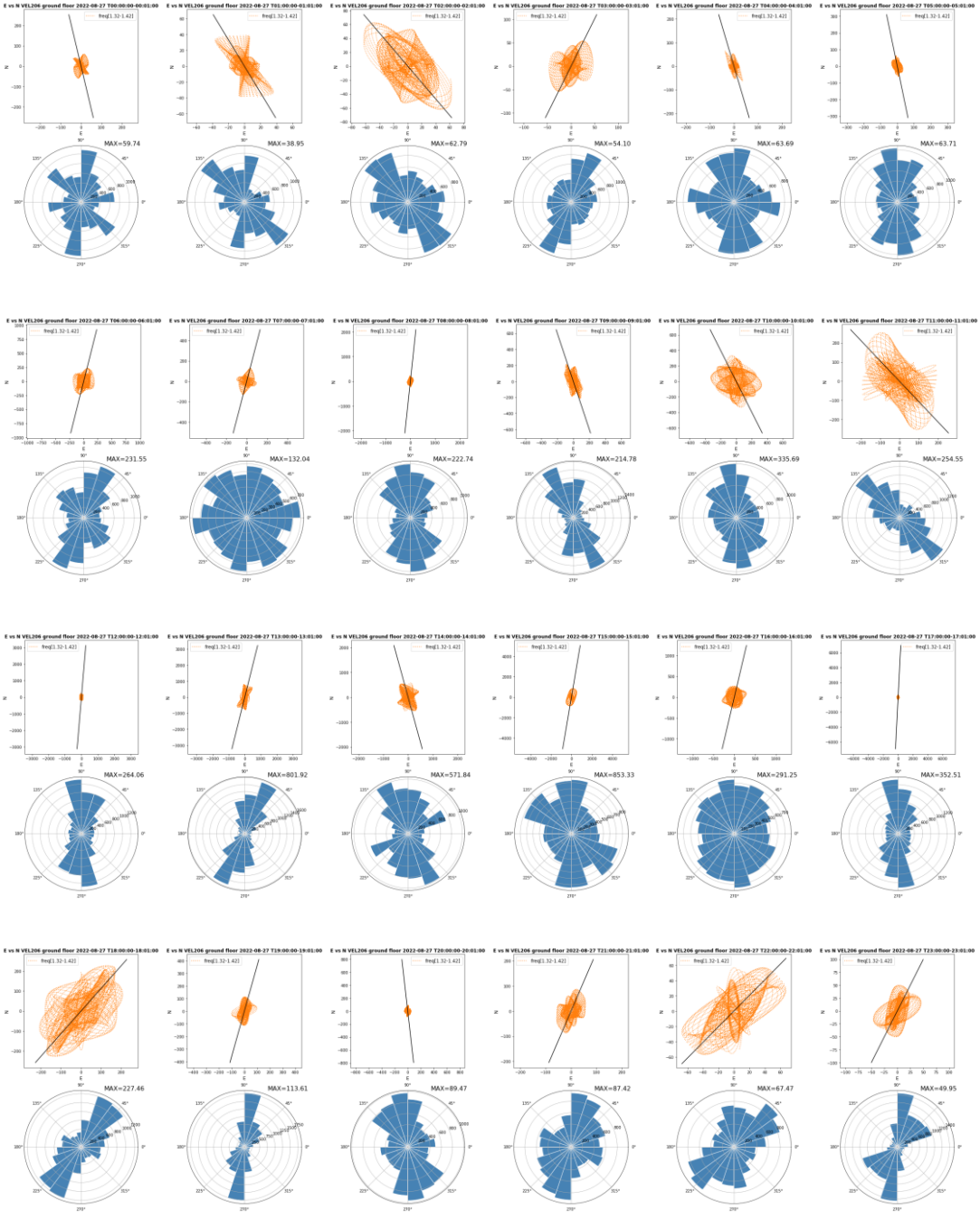

Figure 41: The set of all the hodograms, divided per sensor and calculated for the initial minute of every hour, presented in both Cartesian coordinates (above) and polar coordinate histogram (below) for the 27th of August.

A preliminary comparison between the Cartesian hodograms of the top of the chimney in Porto Tolle and Angera reveals that the motion of particles in the same amount of time appears to form more detailed and irregular shapes in the latter, in contrast to the former where many hodograms exhibit a tendency to form more or less elongated ellipses that intersect with one another. In all the time intervals of the hodograms of all sensors, the maximum values recorded in digital counts are displayed, which are directly related to the maximum displacement.

An examination of the direction of the vibrations reveals a discernible north-east axis of propagation, as indicated by the velocimeter on the upper floor. This strong directionality is also evident in the velocimeter on the 4th floor, although with a slight inclination along the east-west axis. A prevailing northeast directionality is also observed in the velocimeter on the 2nd floor, although with a greater number of hodograms indicating evenly distributed vibrations. In contrast, the directionality of vibrations is no longer evident in the velocimeter on the ground floor, as it should normally be.

Regarding the maximum vibration amplitude values shown in the hodograms, the values for the 4th floor, on average, are approximately one order of magnitude greater than the amplitudes of the other floors. On July 27th, the maximum value observed on the top floor was approximately 10000 digital counts, while the maximum amplitude recorded on the fourth floor was 36000 digital counts.

However, looking at the maximum values of all the sensors, with the exception of the fourth floor, the values, although not constant within the day, exhibit a downward trend as one proceeds from the 6th floor of the bell tower towards the ground floor where the values are in the tens and hundreds digital counts. The hodograms were calculated for the frequency range shown by the peaks in the previous analyses corresponding to the fundamental mode of vibration of the tower. The first or fundamental mode corresponds to a traslation in

which the entire structure oscillates like a pendulum with maximum displacements at the top of the tower and minimums at the base. This is in accordance with the trend of decreasing maximum values with height shown in the hodograms.

Note also how for all sensors and for both days the smaller amplitudes occur towards the end of the day concordant with the lower signal strength shown in the RMS.

Although the bell tower is not as high as the Porto Tolle chimney, it is still interesting to test a possible correlation between vibration direction and weather conditions. *Fig.42* shows weather data recorded from a weather station located in a neighboring town south of the city of Angera.

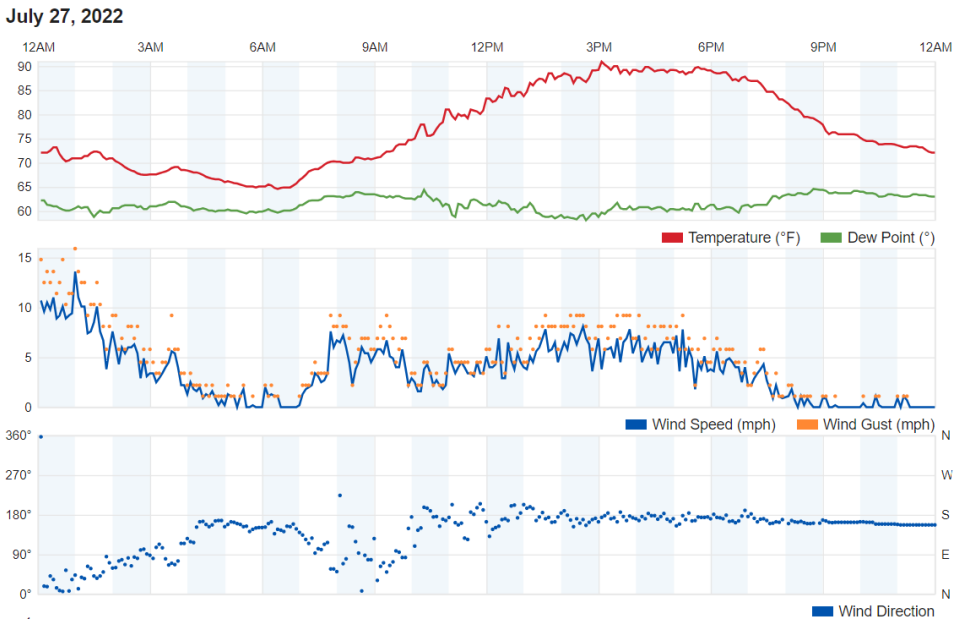

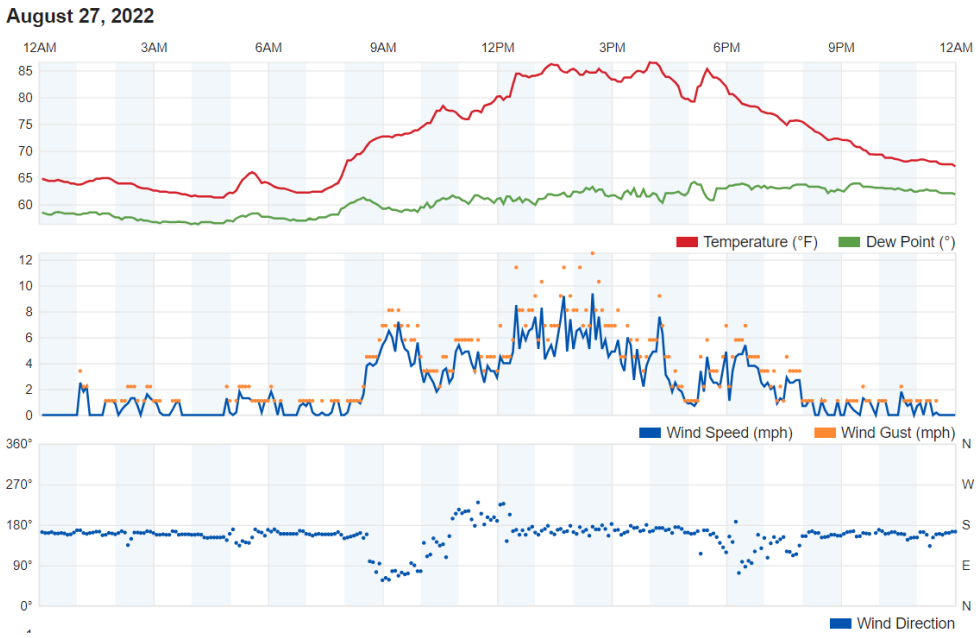

Figure 42: Wind data from a weather station located south to the city of Angera for the 27th of July (above) and the 27th of August (below).

From the wind direction data, it can be seen that for both days the wind blew predominantly southward with variations in direction toward the east and north.

Looking mainly at the velocimeter at the highest plane, there is no hodogram showing a prevailing directionality of vibration in that direction. In any case, an examination of the Cartesian hodograms reveals the existence of a north-south component in some time windows, manifested as a distinctive shape in the particle motion along that direction. Such a phenomenon is observable in the hodograms of July 27th at midnight and 1 a.m. UTC, as well as in those of August 27th from 6 p.m. until 11 p.m UTC.

Fig. 43 and Fig. 44 illustrates the calculated RMS values for displacement in a single horizontal direction for the velocimeter on the 6th floor for both days, with a comparison to the wind data collected on the same day. Both graphs are shown in the same time zone i.e. CEST and are therefore directly comparable.

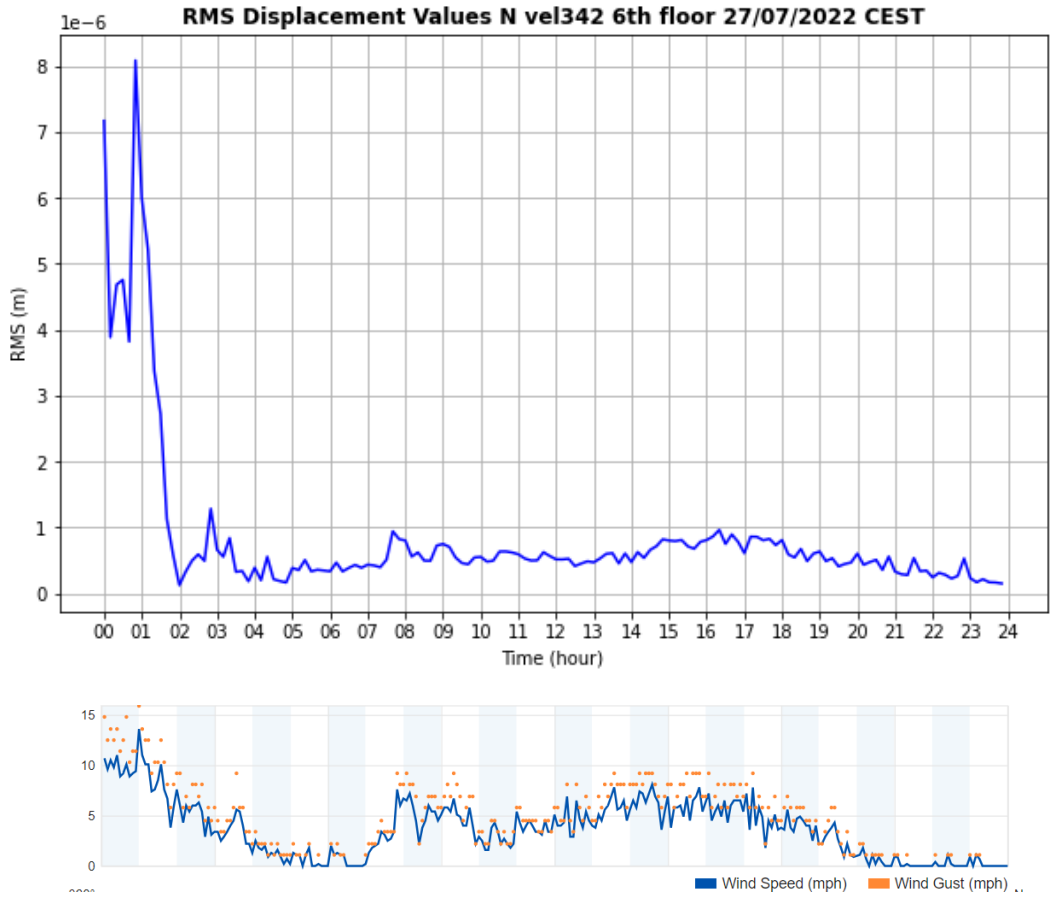

Figure 43: Comparison between the RMS displacement values of the velocimeter on the 6th floor calculated for one horizontal directions for the 27th July and wind speed data collected during the same day. The two are both in CEST time zone.

An examination of the data for July 27th in the RMS reveals elevated values between midnight and 2 a.m., which also correspond to the stronger wind gusts of the day. Additionally, the two hillocks between 7:30 a.m. and 9:30 a.m. appear to align with the data in both graphs. In any case, the sharp decline from the maximum at 1 p.m. in the RMS, is more gradual in the wind speed graph. Furthermore, the disparity between tha maximum and minimum values observed within the day is significantly greater for the RMS of displacement than for the wind speed data. During the rest of the day, wind

speeds and gust are slightly lower than those recorded at 1 a.m. -a 5mph difference corresponds to a difference of approximately 8 km/h-, yet the resulting RMS values did not exhibit comparable increases.

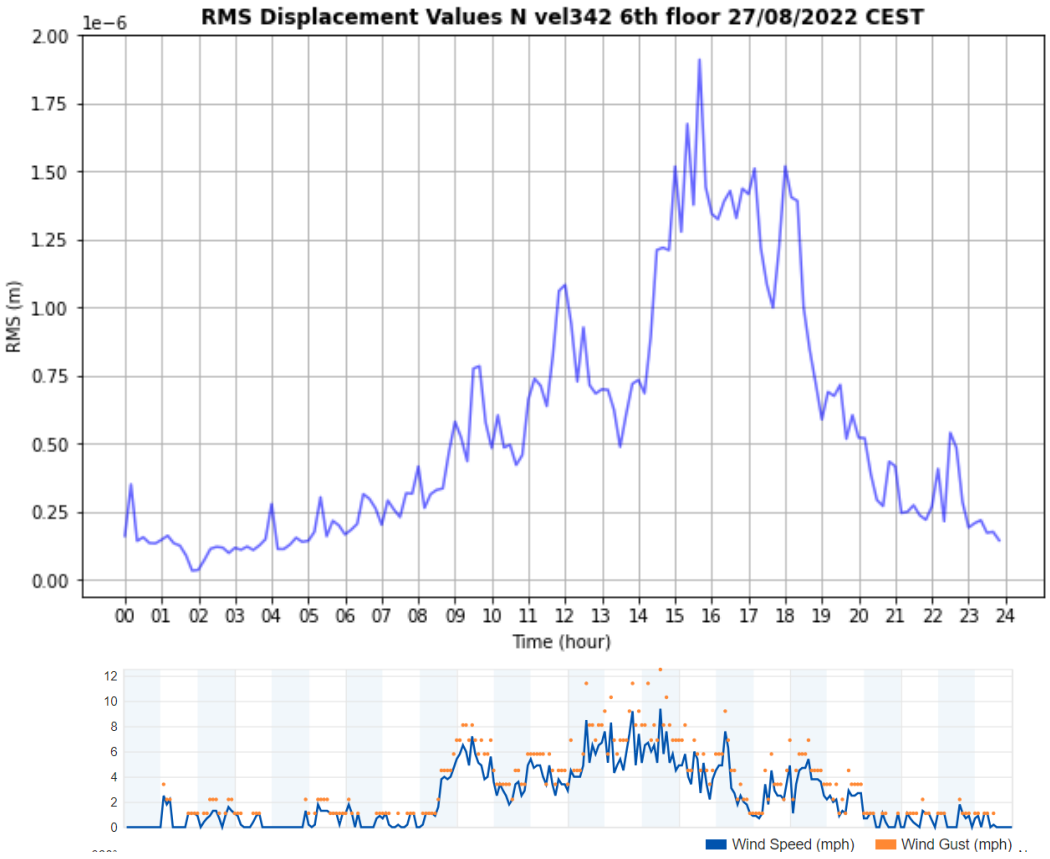

Figure 44: Comparison between the RMS displacement values of the velocimeter on the 6th floor calculated for one horizontal directions for the 27th August and wind speed data collected during the same day. The two are both in CEST time zone.

The wind speed trend on the 27th of August exhibits a comparable pattern to that of RMS; however, the two graphs are out of phase, and the times of maximum displacement do not fully align with the times of maximum wind. The maximum wind speed values are observed between 12 noon and 5 p.m.,

while the maximum values for the RMS of displacement are observed between 2 p.m. and 7 p.m..

In any case, the prevalence of the bell tower's oscillatory motion along a northeast-southwest trajectory may be attributed to the geometric and structural characteristics of the tower itself. As illustrate in *Fig.45*, which was adapted from *Fig.13*, it can be observed that the direction of vibration occurs along the shorter side of the building, which generally exhibits lower structural stiffness compared to the longer side.

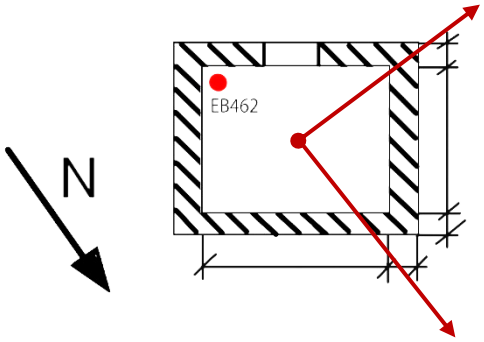

Figure 45: Orientation of one floor of the bell tower from Fig.13.

4.1.6 MODAL ANALYSIS

As for the sensor configuration in Porto Tolle, acceleration data are available for Angera only from the accelerometer on the sixth floor. From these data, six 20-minute intervals were collected at different times for six different days. Modal analysis was then performed on each interval, and the average frequency was calculated.

Fig. 46 illustrates the results obtained for a single time interval. The peak reported by the SVD lines, corresponding to the fundamental mode of vibration of the bell tower, is equivalent to an average value of 1,44 Hz, calculated for all intervals. Similarly, coupled modes were identified in this case, as for the chimney at Porto Tolle. This was confirmed by the MAC value

and vibration animation. The coupled mode shows a similar frequency of 1,42 Hz along one direction and 1.45 Hz along the perpendicular one.

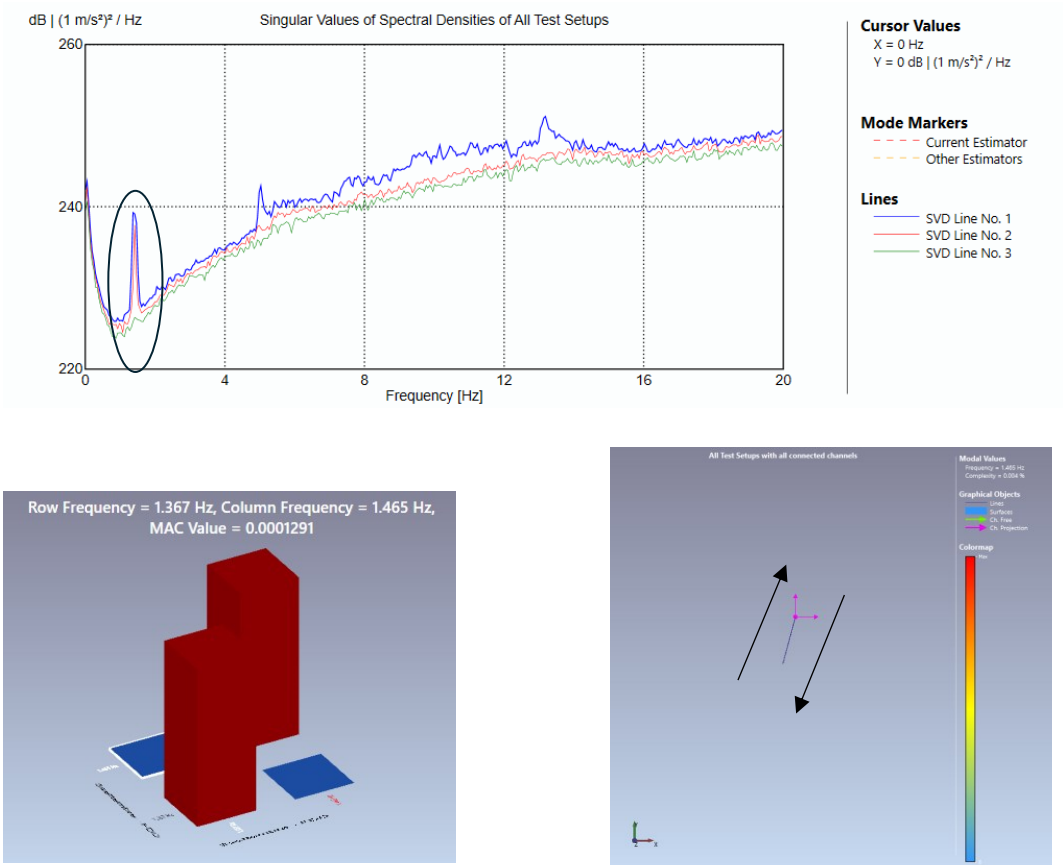

Figure 46: Graphical representation of the singular values in function of frequency -SVD lines- (top), MAC value of two selected frequencies within the first peak (bottom left) and screenshot of the animation of the first modal form (bottom left) of only one 20-minute interval for just the accelerometer on the 6th floor.

In contrast to Porto Tolle, velocimeters placed in the other floors are also available for the modal analysis of the Angera bell tower. The sensor velocity data at the fourth and second floors were then converted to accelerations and used for modal analysis to identify the higher modes of the structure.

A simple lumped-mass model of the bell tower was then constructed with a line and three nodes placed at the heights of the various floors where the

sensors were placed. As for the identification of the initial mode, identical intervals were employed, but prior to August 8th, so that the data from the sensor on the fourth floor could also be accessible.

The results for one interval are illustrated in *Fig.47*.

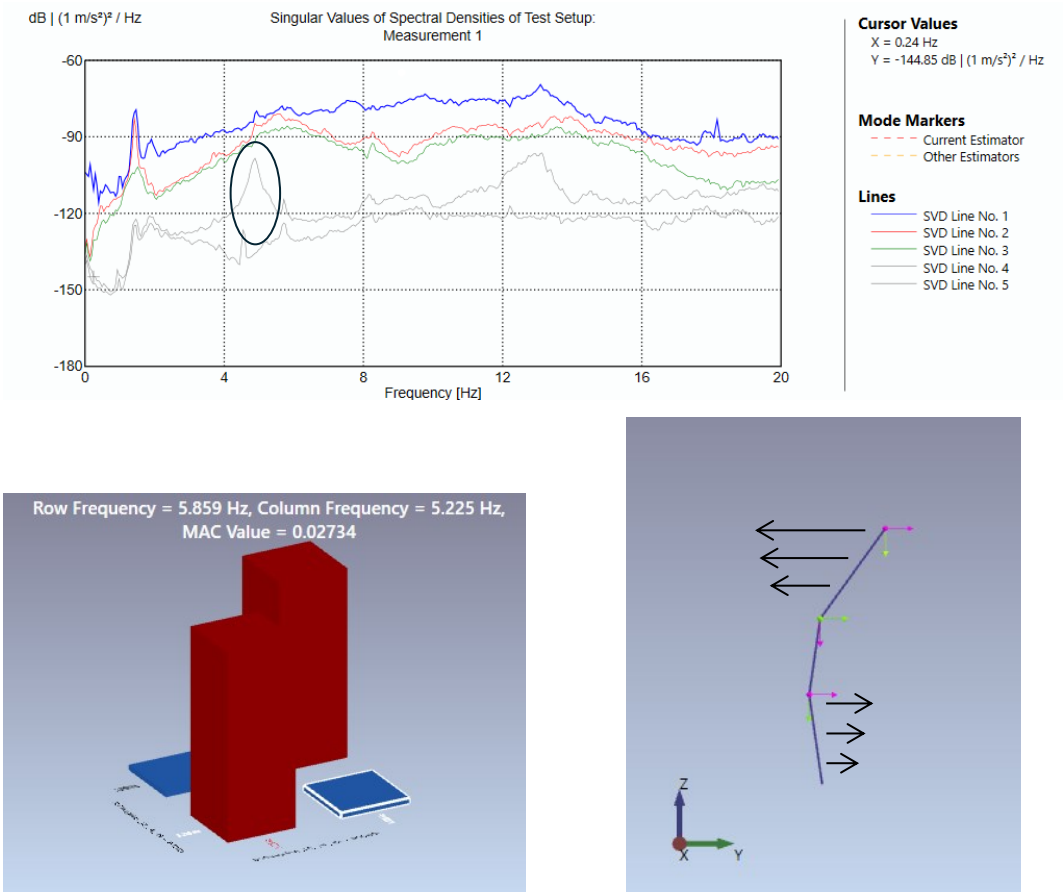

Figure 47: Graphical representation of the singular values in function of frequency -SVD lines- (top), MAC value of two selected frequencies within the circled peak (bottom left) and screenshot of the animation of the second modal form found for one of the selected frequencies (bottom right) of only one 20-minute interval for the accelerometer on the 6th floor and the velocimeter converted.

Looking at the obtained SVD lines, a peak corresponding to the fundamental frequency of vibration clearly appears while no second peak is so evident equally for all SVD lines. Typically the first SVD line, the blue line, represents

the strongest modal contribution, which is usually associated with the main mode of the structure. However, no other significant peaks are visible in the blue SVD line. Additionally, a further issue arises when a frequency in the blue SVD line is selected for the vibration animation. In this animation, the middle node corresponding to the sensor on the fourth floor exhibits a significantly greater degree of movement than the other sensors, which instead appear to move only minimally. In fact, the maximum value of acceleration registered by the sensor in the 4th floor is markedly elevated relative to the average values recorded by the other sensors.

The SVD algorithm decomposes the signal recorded by the sensors into the main modal components. If one sensor, in this case the central one, records significantly higher values than the other two sensors, it may dominate the decomposition. However, each SVD line captures different modal components, and the second mode of vibration may be predominant in another line. In this case, the second mode around 5 Hz is predominant in the SVD line No.4, visible by a peak and confirmed by the animation reported in *Fig.47*.

Analysing all the intervals, which all present this same problem, the second vibration mode of the structure was identified at a frequency of 5.09Hz.

The modal analysis of just one single interval revealed the presence of coupled modes in the second vibration mode identified at 5.22 Hz and 5.86 Hz. (MAC value in *Fig.47*).

5. DISCUSSION

5.1 CORRELATION WITH WIND

Flexible and tall structures are sensitive to dynamic wind loads. For typical tall buildings, oscillations have been observed not just in the alongwind direction but also in the crosswind directions, as well as in the torsional mode *(Lin et al.,2005)*.

The methodologies used to study the wind-induced vibration of tall buildings can be classified into three categories: wind tunnel test, numerical simulation, and field measurement. Field measurement, usually involves the measurement of wind speed and acceleration. In some cases, the displacement, pressure, and strain are also measured. The dynamic response of tall buildings is mainly measured under typhoon or strong wind owing to their ability to trigger large-amplitude vibrations *(Hou et al., 2020)*.

In consideration of the data recorded by the weather stations situated in the proximity of the chimney and bell tower, the maximum wind gusts are observed to reach approximately 12-13 miles per hour in Angera and 7 miles per hour in Porto Tolle. Conversion to kilometers per hour yields a wind speed of 24 km/h and 11 km/h, respectively. According to the Beaufort scale, a wind is considered strong wind from 50-61 km/h.

In this study, correlation with wind data was based on the analysis of directionality and maximum values shown by relative displacement in hodograms and RMS. Directionality in any case cannot be directly attributed to wind. Wind can lead to oscillation of buildings along the direction of flow as well as perpendicularly and rotationally. These different oscillations are present in all hodograms in smaller or larger amounts. Therefore, it is not possible to discern whether these movements are due to wind, other noise elements, or the natural oscillation of the towers. In any case, this interpretation is based on only one minute of analysis per hour, which is not

enough to fully represent the changes in wind direction. The maximum values of RMS are also not directly related to the wind since they do not correspond to the maximums of the wind speed or gust. The only comparison that yields concordant results is between the RMS analysis and wind speed for Angera on July 27th. However, as the trend appears similar, the difference in values are not and it's not possible to directly attribute the results to wind. Also, during this wind gust no significant change in direction was observed.

However, for the Porto Tolle chimney, due to its high height, the wind speed and direction values at the top may vary from those recorded by the meteorological station. In fact, in the RMS of displacement a high peak is recorded around 9 a.m. CET that does not correspond to the wind gusts recorded by the station and there may also be the possibility that the wind speed data are missing and not null and therefore those spikes actually correspond to unrecorded wind gusts. Also, in the hodograms at the top of the chimney, the direction of the axis of motion varies more within the day than for Angera.

In sum, the use of these analyses doesn't provide definitive evidence of a correlation with wind data. In both cases studies, the wind is relatively weak and thus may play a subordinate role compared to the influence of anthropogenic activities. The installation of an anemometer and a GPS device to detect absolute displacement on the chimney during stronger wind events, in conjunction with wind tunnel tests or numerical simulations, may facilitate the generation of more specific results for future analysis.

5.2 THE VELOCIMETER AT THE 4TH FLOOR IN THE BELL TOWER

The velocimeter on the 4th floor of the Angera bell tower shows discordant results with the other sensors for three out of five analyses.

In the PSD analysis, the frequency peaks are shifted to lower values compared to the other velocimeters. The maximum values reported by the hodograms are visibly higher compared to the values on the upper and lower floors and consequently the modal analysis is affected, showing inconsistent SVD lines.

In contrast, the results obtained from the HVSR and spectrograms are consistent with those of the other sensors: peaks at higher frequencies, corresponding to higher vibrational modes, are more highlighted in this floor.

The sensor was removed on the 8th of August after presenting some problems. The inconsistent results obtained for some analyses could be due to problems with the calibration and the state of health of the sensor. Or rather the results are actually related to the lower stiffness of the fourth floor, which seems to be under greater stress due to the higher values recorded. To confirm the reasons for these discrepancies, the fourth floor should be subjected to a continuous SHM with several sensors. This could also be the subject of a future analysis.

5.3 CONSISTENCY OF RESULTS

5.3.1 PORTO TOLLE CHIMNEY

Regarding the velocimeter above the tower, the peak values identified in the HVSR, PSD and the frequency peaks observed in the spectrogram coincide. The identified values range from 0.3 Hz to 0.4 Hz for the first peak and approximately 1.5 Hz for the second peak. In addition, the peaks are discernible and persistent throughout the entirety of the recording period.

The peak values obtained for the accelerometer are consistent with those obtained for the PSD, spectrogram and SVD lines obtained from the modal analysis and coincide with those of the velocimeter. In the HVSR results, on the other hand, the peak below 1 Hz is not identifiable. This discrepancy may

be attributed to the potential influence of the vertical component in the spectral ratio calculation, which was not considered in the other analyses. It is possible that below 1 Hz, there is an intrinsic or an external noise along the vertical axis that maintains a low value for the H/V ratio.

Additionally, the accelerometer data suggest a notable dependence of the results on the signal strength reported in the RMS. For both the HVSR, the PSD and spectrogram, the results obtained for an interval where the signal is stronger exhibit more pronounced peaks and highlight those at higher frequencies.

For the other velocimeters installed on the ground, the peaks in frequency for both the HVSR and the PSD are still discernible at the base of the tower but gradually diminish with distance. This phenomenon is also evident in the frequency bands visible in the spectrograms. Additionally, the sensor at the base of the tower demonstrates a similar dependency to that observed in the accelerometers, with a more visible 1.5 Hz peak emerging in the HVSR during a time interval of increased signal.

5.3.2 ANGERA BELL TOWER

For the results on the Angera bell tower, the observations are similar to those for the Porto Tolle chimney. With the exception of the sensor on the fourth floor, which was discussed in the previous chapter, the frequency peaks obtained from the PSDs and spectrograms are consistent with one another for the velocimeters. They reveal the presence of two peaks below 10 Hz, around 1.4 Hz and 5 Hz, as well as one above, which is visible mainly in the sensors located below the sixth floor.

The peaks of the PSD, HVSR and spectrogram bands for the accelerometer are also consistent, and the results obtained for different time intervals again demonstrate the greater dependence of the accelerometer results to signal

strength. This shows how the accelerometer proves to be less sensitive to low intensity signals.

In contrast, the HVSR results for the velocimeter exhibit slight discordance, with the 1.5 Hz peak appearing to be doubled and a second peak at 0.8 Hz becoming more prominent in all sensors on floors below the sixth. In any case, this peak at 0.8 Hz is present only in the HVSRs and is not confirmed by the other analyses. Therefore, as for Porto Tolle, it is possible that the vertical component may had an influence on the calculation of the spectral ratio and on the results obtained from this analysis.

The peak obtained from the SVD lines for the accelerometer is also consistent. Instead, the peak of the SVD lines calculated with the addition of the converted velocimeters although not consistent for all SVD lines is in line with the values found from the other analyses.

5.4 CHIMNEY Vs BELL TOWER

The two analyzed structures differ in several elements, as summarised in *Tab.5*.

Table 5: Table of major differences between the two buildings.

	Approx. h.	Materials	Shape	Period	Environ.	Type	Monitor. Design
PORTO TOLLE CHIMNEY	250m	reinforced concrete	round	1980-1984	isolated lagoon	industrial	Increasing distance
ANGERA BELL TOWER	30m	masonry	rectangular	medieval	urban	hystorical	Increasing height

Certainly, the large difference in height is one of the major factors that seems to influence the different dynamic behaviour of the structures, especially the

oscillation eigen frequency. In fact, the fundamental frequency of oscillation observed for the Porto Tolle chimney is approximately 0.4 Hz, which corresponds to an oscillation period of 2.5 seconds. In contrast, the fundamental frequency observed for the less elevated Angera bell tower is approximately 1.4 Hz, which corresponds to an oscillation period of 0.7 seconds.

However, additional structural elements, including materials of construction, shape and period of construction, must be considered when comparing the two structures. The data obtained from the Angera bell tower indicate that the structure exhibits a more complex dynamic response. The frequency peaks of higher modes are also discernible and the hodograms display more articulated motion shapes.

For both structures, the data indicate a correlation between the recorded signal strength and the peak intensities, particularly for the accelerometer results.

The recorded signal is a function of the different environmental contexts in which the two structures are situated, which in turn model the characteristics of environmental noise. From the RMS and spectrograms, it is evident that the recorded signal intensity is irregular, and more distributed for the bell tower, which is located in an urban context and in an area frequented by tourists during the summer months. Conversely, the industrial chimney, situated in an isolated lagoon area, is surrounded by a rural landscape of countryside and canals, which results in a less disturbed recorded signal reflecting the times when the reclamation work associated with the former power plant is underway.

6. CONCLUSIONS

In conclusion, the multidisciplinary analysis conducted on both structures highlighted the importance of using various techniques to fully characterize the dynamic responses of tall buildings. The Operational Modal Analysis -OMA-, combined with passive seismic monitoring, proved particularly effective in identifying the oscillation frequencies and vibration modes of the structures under ambient noise conditions. The integration with Power Spectral Density -PSD- analysis allowed for a clear representation of the frequency peaks associated with the different oscillation modes, while modal analysis provided a decomposition of vibrations into well-defined modal shapes.

Furthermore, the use of the H/V spectral ratio -HVSR- and hodogram analysis, which provide information on signal directionality and particle motion, made the analysis more robust and complete, enabling verification of the consistency of the results. This methodological combination, performed over different time intervals and varying environmental conditions, further increased the reliability of the results.

One of the most interesting aspects emerging from the analyses is the importance of the surrounding environment and external conditions, such as wind, human and environmental activites that may play a significant role in exciting taller structures and whose study is enabled by RMS and spectrogram analysis.

The enhancement of the network of sensors and the addition of specific monitoring tools, such as anemometers, would allow for continuous structural health monitoring and offer a deeper understanding of dynamic behavior under both normal and extraordinary conditions, such as seismic events or extreme weather conditions.

In summary, the multidisciplinary approach, combining OMA, PSD, HVSR, and hodogram analysis, represents the most comprehensive and reliable methodology for obtaining an integrated view of the dynamic responses of structures. While RMS and spectrograms allow for a greater knowledge and insight into the environmental context in which the structures are located, thereby enabling the quantification of the impact of the input signal's pattern, intensity and frequency content on the structure's dynamic response.

BIBLIOGRAPHY

- *Andò, B., Baglio, S., & Pistorio, A. (2018). A low cost multi-sensor system for investigating the structural response of buildings. *Annals of Geophysics, 61*(2), SE217-SE217.*
- *Baker, K. (2005). *Singular value decomposition tutorial*. The Ohio State University, 24, 22.*
- *Boaga, J., Casarin, F., De Marchi, G., Valluzzi, M. R., & Cassiani, G. (2019). 2016 central Italy earthquakes recorded by low-cost MEMS-distributed arrays. *Seismological Research Letters, 90*(2A), 672-682.*
- *Bonnefoy-Claudet, S., Cotton, F., & Bard, P. Y. (2006). The nature of noise wavefield and its applications for site effects studies: A literature review. *Earth-Science Reviews, 79*(3-4), 205-227.*
- *Cascone, V., Boaga, J., & Cassiani, G. (2021). Small local earthquake detection using low-cost MEMS accelerometers: Examples in northern and central Italy. *The Seismic Record, 1*(1), 20–26. https://doi.org/10.1785/0320210007*
- *Cochard, A., Igel, H., Schuberth, B., Suryanto, W., Velikoseltsev, A., Schreiber, U., Wassermann, J., Scherbaum, F., & Vollmer, D. (2006). Rotational motions in seismology: Theory, observation, simulation. In *Earthquake Source Asymmetry, Structural Media and Rotation Effects* (pp. 391–411). Springer: Berlin/Heidelberg, Germany.*
- *Crognale, M., Rinaldi, C., Potenza, F., Gattulli, V., Colarieti, A., & Franchi, F. (2024). Developing and testing high-performance SHM sensors mounting low-noise MEMS accelerometers. *Sensors, 24*(8), 2435. https://doi.org/10.3390/s24082435*
- *Enel,1976, picture from Achivio Centr. Termoel. P. Tolle*
- *Enel,2016, https://www.enel.com/company/stories/articles/2016/08/from-old-power-station-to-new-community-space*

- *Georicerche Srl. (2024). Technical report 'Report della campagna di indagini geognostiche eseguita presso l'ex centrale termoelettrica Enel S.p.A. in comune di Porto Tolle (RO)'.*
- *Hou, F., & Jafari, M. (2020). Investigation approaches to quantify wind-induced load and response of tall buildings: A review. Sustainable Cities and Society, 62, 102376.* https://doi.org/10.1016/j.scs.2020.102376
- *Isamgeo Italia Srl. (2024) Technical report 'Ciminiera dell'ex-centrale ENEL di Polesine Camerini sita nel comune di Porto Tolle (RO). Caratterizzazione geofisica dei terreni di fondazione'.*
- *Jwo, D.-J., Chang, W.-Y., & Wu, I.-H. (2021). Windowing techniques, the welch method for improvement of power spectrum estimation. *Comput. Mater. Contin, 67*(3), 3983-4003.*
- *Landès, M., Hubans, F., Shapiro, N. M., Paul, A., & Campillo, M. (2010). Origin of deep ocean microseisms by using teleseismic body waves. *Journal of Geophysical Research: Solid Earth, 115*(B5).*
- *Lin, N., Letchford, C., Tamura, Y., Liang, B., & Nakamura, O. (2005). Characteristics of wind forces acting on tall buildings. *Journal of Wind Engineering and Industrial Aerodynamics, 93*(3), 217-242.*
- *Mariotti, V., & Simonotti, F. (2001-2002). Angera (VA). Oratorio di S. Filippo Neri. Rilievo di strutture murarie in alzato. *Notiziario della Soprintendenza Archeologica della Lombardia*, pp. 201-202.*
- *Molnar, S., Sirohey, A., Assaf, J., et al. (2022). A review of the microtremor horizontal-to-vertical spectral ratio (MHVSR) method. *Journal of Seismology, 26*, 653–685.* https://doi.org/10.1007/s10950-021-10062-9
- *Nakamura, Y. (1989). A method for dynamic characteristics estimation of subsurface using microtremor on the ground surface. *Q.R. of RTRI*.*
- *Novotny, O. (1999). *Seismic surface waves*. Bahia, Salvador: Instituto de Geociencias.*

- *Okada, H., & Suto, K. (2003). *The microtremor survey method*. Society of Exploration Geophysicists.*
- *Pham, N. D. (2009). *Rotational Motions in Seismology: Theory, Observation, Modeling* (Ph.D. Thesis, Ludwig-Maximilians-Universität München, München, Germany).*
- *Rayleigh, L. (1892). XVI. On the instability of a cylinder of viscous liquid under capillary force. *The London, Edinburgh, and Dublin Philosophical Magazine and Journal of Science, 34*(207), 145-154.*
- *The University of Waikato, 2007, www.sciencelearn.org.nz*
- *Xu, R., & Wang, L. (2021). The horizontal-to-vertical spectral ratio and its applications. *Eurasip Journal on Advances in Signal Processing, 2021*(1). https://doi.org/10.1186/s13634-021-00765-z*